

AD-A258 975



1

AFIT/GAE/EN 172D-08

DTIC  
ELECTE  
JAN 6 1993  
S c D

STRATEGIES FOR OPTIMAL CONTROL  
DESIGN OF NORMAL ACCELERATION  
COMMAND FOLLOWING ON THE F-16

THESIS

James C. Baird, Captain, USAF

AFIT/GAE/ENY/92D-08

012225



93-00169

1991

Approved for public release; distribution unlimited

93 1 04 020

STRATEGIES FOR OPTIMAL CONTROL DESIGN OF NORMAL  
ACCELERATION COMMAND FOLLOWING ON THE F-16

THESIS

Presented to the Faculty of the School of Engineering  
of the Air Force Institute of Technology  
Air University  
In Partial Fulfillment of the  
Requirements for the Degree of  
Master of Science in Aeronautical Engineering

James C. Baird, B.S.

DTIC QUALITY INSPECTED 5

Captain, USAF

December 1992

Approved for public release; distribution unlimited

Accession For	
NTIS GRA&I	<input checked="checked" type="checkbox"/>
DTIC TAB	<input type="checkbox"/>
Unannounced	<input type="checkbox"/>
Justification	
By	
Distribution/	
Availability Codes	
Dist	Avail and/or Special
A-1	

## **Preface**

This application oriented thesis has taken many long nights and hundreds of designs to piece together, but I believe that each minute was well worth it and enjoyed. Hopefully this effort will be useful to designers seeking to develop optimal controllers, and if this work brings the eventual use of one of these optimal methods on an actual aircraft one step closer to reality, I will know that my goal has been accomplished. My honest belief is that general mixed  $H_2/H_\infty$  optimization is the methodology of the near future, and I have confidence that the reader will agree.

Now I wish to thank the many people that have helped me on this thesis, and at AFIT in general. I begin by thanking the most important friends that I see everyday, this special recognition goes to my AFIT classmates of GAE-92D. The support I have received from Craig, Mike, Joe, Dempsey, and Dan has been incredible. Naturally the staff at AFIT has made a tremendous impression on me, and I trust that many more Air Force officers will realize the quality of education here and enroll at AFIT. Most importantly, the faculty members that I wish to thank are my thesis committee, consisting of Dr Liebst and Capt Walker, and my advisor, Dr Ridgely. Dr Ridgely has given much needed guidance over my stay at AFIT, not only on my thesis, but on other technical subjects and on personal issues. I owe him the most of anyone for opening my eyes to the incredible

world of modern flight control design. Also, the timely support of Maj Mracek will be well remembered. Not to forget the closeness to the Control Analysis Group of the Flight Dynamics Laboratory, I acknowledge the efforts and kindness of Mr Bowlus and Dr Banda. For technical support on writing this thesis, Capt Wells has aided me with graphical integration and word processing problems, not to mention having such a fine thesis to use as a guide. I also thank God for giving me this opportunity, and for blessing me with good health.

Lastly, and most importantly, I want to thank the one that has made AFIT and my life so enjoyable, and the one I love with all my heart, Jennifer Hill. I do not believe there is another woman that could have endured the strain on a relationship such as she has.

Dedicated to my fiancée, Jennifer Hill. Thanks for everything!

James C. Baird

# Table of Contents

	Page
Preface . . . . .	ii
List of Figures . . . . .	vi
List of Tables . . . . .	x
Notation . . . . .	xi
Abstract . . . . .	xiii
 I. Introduction . . . . .	 1-1
1.1 Background . . . . .	1-1
1.2 Research Objectives . . . . .	1-5
1.3 Scope . . . . .	1-6
1.4 Thesis Outline . . . . .	1-6
 II. Methodology Overview and Related Work . . . . .	 2-1
2.1 General Discussion . . . . .	2-1
2.2 H <sub>2</sub> Optimization . . . . .	2-1
2.3 H <sub>∞</sub> Optimization . . . . .	2-6
2.4 Mixed H <sub>2</sub> /H <sub>∞</sub> Optimization . . . . .	2-12
2.5 Review of Related Work . . . . .	2-19
 III. Pre-Design Process . . . . .	 3-1
3.1 F-16 Model Development . . . . .	3-1
3.2 Closed-Loop Evaluation Models . . . . .	3-8
3.3 Design Limitations . . . . .	3-14

IV. $H_2$ Designs . . . . .	4-1
4.1 $H_2$ /LQG Regulator . . . . .	4-1
4.1.1 $H_2$ /LQG Weight Selection . . . . .	4-5
4.1.2 $H_2$ /LQG Results . . . . .	4-6
4.2 $H_2$ /LQG Sensitivity . . . . .	4-19
4.2.1 $H_2$ /LQG Sensitivity Weight Selection . . . . .	4-22
4.2.2 $H_2$ /LQG Sensitivity Results . . . . .	4-24
4.3 $H_2$ /LQG Tracking . . . . .	4-36
4.3.1 $H_2$ /LQG Tracking Weight Selection . . . . .	4-39
4.3.2 $H_2$ /LQG Tracking Results. . . . .	4-41
 V. $H_\infty$ Design . . . . .	 5-1
5.1 $H_\infty$ /Robust Tracker . . . . .	5-1
5.1.1 $H_\infty$ /Robust Tracking Weight Selection . . . . .	5-6
5.1.2 $H_\infty$ /Robust Tracking Results . . . . .	5-8
5.2 $H_\infty$ Sub-Optimal Examination (Central) . . . . .	5-24
 VI. Mixed $H_2$ / $H_\infty$ Design . . . . .	 6-1
6.1 $H_\infty$ Sensitivity and $H_2$ Tracker . . . . .	6-1
6.2 $H_2$ / $H_\infty$ Weight Selection . . . . .	6-4
6.3 Mixed $H_2$ / $H_\infty$ Solution . . . . .	6-6
6.4 DFP Start Compensator . . . . .	6-11
6.5 Mixed $H_2$ / $H_\infty$ Results . . . . .	6-14
 VII. Conclusions and Recommendations . . . . .	 7-1
7.1 Summary and Conclusions . . . . .	7-1
7.2 Recommendations for Future Work . . . . .	7-5
 Appendix A: F-16 Model Data . . . . .	 A-1
 Bibliography . . . . .	 BIB-1
 Vita	

## List of Figures

Figure	Page
2-1. $H_2$ Design Diagram . . . . .	2-2
2-2. (J,Q)-Parameterization . . . . .	2-5
2-3. $H_\infty$ Design Diagram . . . . .	2-7
2-4. Mixed $H_2/H_\infty$ Design Diagram . . . . .	2-13
3-1. Lower Order Plant Magnitude Vs Higher Order . . . . .	3-6
3-2. Multiplicative Uncertainty . . . . .	3-7
3-3. Plant Additive Uncertainty . . . . .	3-8
3-4. Transfer Function/Lower Order Simulation Model . . . . .	3-9
3-5. Magnitude of $G_{rd}(s)$ . . . . .	3-10
4-1. $H_2$ /LQG Regulator Diagram . . . . .	4-2
4-2. Compensator Magnitude . . . . .	4-10
4-3. Magnitude of $G(s)K_b(s)$ , LO . . . . .	4-10
4-4. Sensitivity Magnitude, LO . . . . .	4-12
4-5. Magnitude of $K_b(s)S(s)$ , LO . . . . .	4-12
4-6. Complimentary Sensitivity Magnitude, LO . . . . .	4-13
4-7. $\alpha$ from $\alpha(0) = 5$ deg, LO . . . . .	4-14
4-8. Control Usage (u) from $\alpha(0) = 5$ deg, LO . . . . .	4-15

4-9.	$N_z$ from $N_z$ Command Step, LO . . . . .	4-16
4-10.	$N_z$ from $N_z$ Command Step, HI . . . . .	4-17
4-11.	$H_2/LQG$ Sensitivity Diagram . . . . .	4-20
4-12.	Compensator Magnitude . . . . .	4-27
4-13.	Magnitude of $G(s)K_b(s)$ , LO . . . . .	4-28
4-14.	Sensitivity Magnitude, LO . . . . .	4-29
4-15.	Complimentary Sensitivity Magnitude, LO . . . . .	4-30
4-16.	Magnitude of $K_b(s)S(s)$ , LO . . . . .	4-31
4-17.	$\alpha$ from $\alpha(0) = 5$ deg, LO . . . . .	4-32
4-18.	Control Usage ( $u$ ) from $\alpha(0) = 5$ deg, LO . . . . .	4-33
4-19.	$N_z$ from $N_z$ Command Step, LO . . . . .	4-34
4-20.	$H_2/LQG$ Tracking Diagram . . . . .	4-37
4-21.	Feedforward Compensator Magnitude . . . . .	4-43
4-22.	Feedback Compensator Magnitude . . . . .	4-44
4-23.	Magnitude of $G(s)K_b(s)$ , LO . . . . .	4-45
4-24.	Sensitivity Magnitude, LO . . . . .	4-46
4-25.	Complimentary Sensitivity Magnitude, LO . . . . .	4-47
4-26.	Closed-Loop Transfer Function Magnitude, LO . . . . .	4-48
4-27.	Magnitude of $K_b(s)S(s)$ , LO . . . . .	4-49
4-28.	$\alpha$ from $\alpha(0) = 5$ deg, LO . . . . .	4-50
4-29.	Control Usage ( $u$ ) from $\alpha(0) = 5$ deg, LO . . . . .	4-51
4-30.	$N_z$ from $N_z$ Command Step, LO . . . . .	4-52



5-1.	$H_{\infty}$ Robust Tracker Design Diagram . . . . .	5-4
5-2.	Singular Values of $T_{cd}$ , LO . . . . .	5-11
5-3.	Feedforward Compensator Magnitude . . . . .	5-12
5-4.	Feedback Compensator Magnitude . . . . .	5-12
5-5.	Magnitude of $G(s)K_b(s)$ , LO . . . . .	5-13
5-6.	Sensitivity Magnitude, LO . . . . .	5-14
5-7.	Complimentary Sensitivity Magnitude, LO . . . . .	5-15
5-8.	Closed-Loop Transfer Function Magnitude, LO . . . . .	5-16
5-9.	Magnitude of $K_b(s)S(s)$ , LO . . . . .	5-17
5-10.	$N_z$ from $N_z$ Command Step, LO . . . . .	5-19
5-11.	$\alpha$ from $\alpha(0) = 5$ deg, LO . . . . .	5-20
5-12.	Elevator Deflection from $\alpha(0) = 5$ deg, LO . . . . .	5-21
5-13.	Singular Values of $T_{cd}$ , LO . . . . .	5-28
5-14.	Feedback Compensator Magnitude . . . . .	5-29
5-15.	Magnitude of $G(s)K_b(s)$ , LO . . . . .	5-30
5-16.	Sensitivity Magnitude, LO . . . . .	5-31
5-17.	Complimentary Sensitivity Magnitude, LO . . . . .	5-32
5-18.	Closed-Loop Transfer Function Magnitude, LO . . . . .	5-32
5-19.	Magnitude of $K_b(s)S(s)$ , LO . . . . .	5-33
5-20.	$N_z$ from $N_z$ Command Step, LO, Optimal . . . . .	5-34
5-21.	$N_z$ from $N_z$ Command Step, LO, 10% Suboptimal . . . . .	5-35

5-22.	Control Usage (u) from $N_z$ Command Step, LO, Optimal . . . . .	5-36
5-23.	Control Usage (u) from $N_z$ Command Step, LO, 10% Suboptimal . . . . .	5-36
6-1.	Mixed $H_2/H_\infty$ Design Diagram . . . . .	6-2
6-2.	Flow Chart for DFP . . . . .	6-8
6-3.	(J,Q)-Parameterization . . . . .	6-12
6-4.	$\ T_{zw}\ _2$ Versus $\ T_{ed}\ _\infty$ for Mixed Case . . . . .	6-16
6-5.	Maximum Singular Values of $T_{ed}$ , LO . . . . .	6-17
6-6.	Maximum Singular Values of $T_{zw}$ , LO . . . . .	6-18
6-7.	Feedforward Compensator Magnitude . . . . .	6-19
6-8.	Feedback Compensator Magnitude . . . . .	6-20
6-9.	Magnitude of $G(s)K_b(s)$ , LO . . . . .	6-21
6-10.	Sensitivity Magnitude, LO . . . . .	6-22
6-11.	Complimentary Sensitivity Magnitude, LO . . . . .	6-23
6-12.	Closed-Loop Transfer Function Magnitude, LO . . . . .	6-24
6-13.	Magnitude of $K_b(s)S(s)$ , LO . . . . .	6-25
6-14.	$N_z$ from $N_z$ Command Step, LO . . . . .	6-26
6-15.	$\alpha$ from $\alpha(0) = 5$ deg, LO . . . . .	6-27
6-16.	Elevator Deflection from $\alpha(0) = 5$ deg, LO . . . . .	6-27

## List of Tables

Table	Page
4-1. $H_2$ /LQG Results ( $W_z = 1$ ), LO . . . . .	4-7
4-2. $H_2$ /LQG Sensitivity Results ( $W_z = 1$ ), LO . . . . .	4-25
4-3. $H_2$ /LQG Tracking Results ( $W_z = 1$ , $W_e = 20$ ), LO . . . . .	4-42
5-1. $H_\infty$ /Robust Tracking Results, LO . . . . .	5-9
5-2. $H_\infty$ Suboptimal Examination Results, LO . . . . .	5-27
6-1. Mixed $H_2/H_\infty$ Results, LO . . . . .	6-14

## Notation

$\mathbf{R}$	field of real numbers
$\mathbf{x}^T, \mathbf{A}^T$	vector/matrix transpose
$\mathbf{A} > 0$ ( $< 0$ )	$\mathbf{A}$ is positive (negative) definite
$\mathbf{A} \geq 0$ ( $\leq 0$ )	$\mathbf{A}$ is positive (negative) semidefinite
$\bar{\sigma}(\mathbf{A})$	maximum singular value of $\mathbf{A}$
$\text{tr}(\mathbf{A})$	trace of $\mathbf{A} = \sum_{i=1}^n a_{ii}$
$\text{RH}_2$	space of all real-rational, strictly proper, stable transfer matrices
$\text{RH}_\infty$	space of all real-rational, proper, stable transfer matrices
$\ \cdot\ _2$	matrix norm on $L_2$
$\ \cdot\ _\infty$	matrix norm on $L_\infty$
$\left[ \begin{array}{c c} \mathbf{A} & \mathbf{B} \\ \hline \mathbf{C} & \mathbf{D} \end{array} \right]$	transfer function notation $\equiv \mathbf{C}(s\mathbf{I}-\mathbf{A})^{-1}\mathbf{B}+\mathbf{D}$
$\mathbf{G}^*(s)$	complex conjugate transpose of $\mathbf{G}(s) \equiv \mathbf{G}^T(-s)$
$\text{Ric}(\mathbf{M})$	Riccati operator on Hamiltonian matrix $\mathbf{M}$
$\inf$	infimum
$\sup$	supremum
$a \equiv b$	$a$ identically equal to $b$ , $a$ defined as $b$
ARE	Algebraic Riccati Equation

DFP	Davidon-Fletcher-Powell
LFT	Linear Fractional Transformation
LQG	Linear Quadratic Gaussian
LQG/LTR	Linear Quadratic Gaussian with Loop Transfer Recovery
SISO	Single-Input, Single-Output
MIMO	Multiple-Input, Multiple-Output
$\in$	element of
$s$	Laplace variable ( $s = j\omega$ )
$\omega$	frequency variable
$\gamma$	value of the infinity norm
$\gamma_o$	$\inf_{K \text{ adm}} \ T_{ed}\ _{\infty}$
$\gamma_2$	$\ T_{ed}\ _{\infty}$ when $K(s) = K_{2opt}$
$\alpha$	value of the two-norm
$\alpha_o$	$\inf_{K \text{ adm}} \ T_{zw}\ _2$
$\mu$	real number $\in [0,1]$
$\mathcal{L}$	Lagrangian
$K_{2opt}$	the unique $K(s)$ that yields $\ T_{zw}\ _2 = \alpha_o$

## **Abstract**

Weight shapes and locations are investigated for  $H_2$ ,  $H_\infty$ , and the general mixed  $H_2/H_\infty$  optimization methodologies. The design model is normal acceleration command following for the F-16 (SISO) at Mach 0.6 and Sea Level, which yields a nonminimum phase and unstable plant.  $H_2$  design types include LQG, LQG/Sensitivity, and LQG/Tracking. Robustness and tracking are the objectives of the central  $H_\infty$  process. Both  $H_\infty$  optimal and suboptimal controllers are examined, with the suboptimal controller shown as the practical choice for this plant. The mixed  $H_2/H_\infty$  setup allows the tradeoff between  $H_2$  tracking and noise rejection, and  $H_\infty$  robustness. Results of weight choices on all designs are discussed, with the mixed  $H_2/H_\infty$  design being favored.

# **STRATEGIES FOR OPTIMAL CONTROL DESIGN OF NORMAL ACCELERATION COMMAND FOLLOWING ON THE F-16**

## **I. Introduction**

### **1.1 Background**

Frequency weighted optimal control methods have experienced significant advancements over the last decade, but this progress has centered mainly on theoretical aspects. While many optimal design solutions have been simplified, and new ones discovered, the application of optimal compensator designs has lagged far behind the theoretical developments. Furthermore, a large number of applications are either unrealistic, not related to air vehicles, or the basis for selecting the design weights is not included. However, control systems are used in almost every machine in existence, even though all of these are not optimal designs. A performance index is the reason that a design can be considered optimal, with minimization of this measure typically being the task. Three optimal design methodologies examined in this work are the  $H_2$ ,  $H_\infty$ , and general mixed  $H_2/H_\infty$  techniques. Whereas the  $H_2$  and  $H_\infty$  developments are fairly mature, Ridgely's general mixed  $H_2/H_\infty$  method is not

as refined, especially the solution process [Rid91]. This mixed design methodology, that competes  $H_2$  and  $H_\infty$  objectives, also has a limited application history because of its recent development. With a shortage of applications that include background on weight selection (other than the popular mixed-sensitivity case), a need for thorough design formulations is evident.

A compensator is designed with the goal of keeping certain parameters within predetermined levels. Hence, an effective design depends largely on the knowledge of system requirements, and the design parameters that can be manipulated to give these. Typically the linear time-invariant plant, that may include weights, imposes restrictions on the closed-loop system that must be "traded off" by the designer. A simple example would be with the feedback loop itself. While there are obvious advantages that pertain to managing disturbances and small modelling errors, problems can develop in a feedback system due to noise corruption of the feedback signal, or when a disturbance is actually amplified by using the feedback loop. Therefore, a feedback loop can constrain attainable closed-loop properties of the system. Hence, the designer manipulates optimal design parameters, like the quadratic weighting matrices in LQG, to produce a satisfactory compensator. To manipulate this optimal process, the designer must understand the methodology being used so that an appropriate technique can be selected and properly applied to the design plant [FrL88].



Consider the case where the designer needs minimal energy passage to a system output from a white noise input. This is represented by the transfer function (matrix) 2-norm when the input is a zero-mean unit intensity white noise with a Gaussian distribution. The 2-norm calculation represents an integral over the linear frequency range as in

$$\|G(j\omega)\|_2 \equiv \left[ \frac{1}{2\pi} \int_{-\infty}^{+\infty} \text{tr} [G^*(j\omega) G(j\omega)] d\omega \right]^{1/2} \quad (1.1)$$

Even though performance aspects of the optimal  $H_2$  methodology can be significant, as in LQG, the benefits are often overshadowed by the drawback of stability margins that are not guaranteed.

Now consider the case where a bounded, but unknown, input signal needs to be minimized by the control design. This yields the popular  $H_\infty$  methodology, which can be combined with the  $\infty$ -norm's submultiplicative property and the Small Gain Theorem [Zam66] to give a guaranteed robustness level. One motivation for using a robustness tool comes from the model development of the system. Since many approximations and linearizations are required, and some system dynamics are typically ignored, a technique that employs good robustness features is often needed. Unlike the  $H_2$  method, the optimal  $H_\infty$  process can eliminate peaks in a transfer function (matrix) by constraining the maximum singular value over all frequency. This is demonstrated in the  $\infty$ -norm formula, Equation (1.2).

$$\|G(j\omega)\|_{\infty} \equiv \sup_{\omega} \bar{\sigma}[G(j\omega)] \quad (1.2)$$

This constraint imposed by the  $\infty$ -norm calculation gives an "all-pass" feature to the design. The problem with the  $H_{\infty}$  technique is that the noise issue is generally ignored, and turns out to be a serious drawback in optimal  $H_{\infty}$  designs because the compensator does not roll off, like the  $H_2$  compensator does. Furthermore, the optimal  $H_{\infty}$  design possesses an iterative solution technique.

It is clear that each of these optimal design methods has significant benefits that a designer wants, but the drawbacks can be equally important. Hence, the designer needs a process by which the beneficial performance of the  $H_2$  compensator can be visibly traded with the guaranteed robustness of the  $H_{\infty}$  design. It is realistic that one has to be given up to gain more of the other, either robustness or performance, since the two are competing objectives. Ridgely's general mixed  $H_2/H_{\infty}$  methodology accomplishes this by maximizing  $H_2$  performance while holding  $H_{\infty}$  robustness at a predetermined level. Although the mixing of  $H_2$  and  $H_{\infty}$  methodologies is not new, the general mixed technique developed by Ridgely is the first "nonconservative" solution (and is the one employed in this work). With an overview of these three optimal design techniques given, now consider applications of these methods.

The plant used in the design process is generally not the same as the basic model plant. The linear time-invariant design plant, denoted as  $P$ , contains the weights that have been added by the designer. The original plant is only a small part of this design plant; therefore, the compensator that is returned by the optimization procedure is optimized for this design plant. Added weights can be transfer functions that manipulate less important frequency requirements of a design to give better results in more important frequency ranges. However, there are constraints imposed on this tradeoff by the design plant. An example of this would be shaping the sensitivity transfer function for good complex margins, while knowing the sensitivity transfer function must obey an integral constraint.

In summary, this history presents a need for realistic applications of optimal design methods. Three optimal design techniques are introduced, and the design plant is shown to be the key to applying these procedures. Most importantly, the weights included in the design plant are the factors that determine the success of the resulting controller design, and these shapes and locations can be defined once selection of the optimal design method is made.

## **1.2 Research Objectives**

The main objective of this thesis is the investigation of weight locations and shapes for optimal control design techniques. Secondary objectives include examining two degree-of-freedom (2 DOF) controllers for aircraft

applications, justifying the use of an  $H_\infty$  suboptimal compensator over an optimal one, and showing the first realistic application of Ridgely's general mixed  $H_2/H_\infty$  technique.

### **1.3 Scope**

Due to the number of designs shown in this work, each is not examined in full detail. The three design methodologies utilized in this work are the  $H_2$ ,  $H_\infty$ , and general mixed  $H_2/H_\infty$  types. Also, the 2 DOF controller used in many designs has common poles for the feedforward and feedback compensators, unlike some applications where the compensators are independent designs. Although the feedforward compensator can be altered after the design, perhaps to correct a nonzero steady state error from a step input, this is not done here. The basis for choosing weights and analyzing results is to show general trends. In analyzing compensators for time responses, only step commands and initial angle-of-attack ( $\alpha$ ) perturbations will be examined. The short period approximation of the F-16 normal acceleration command following at Sea Level and Mach 0.6 is the aircraft model. Furthermore, result comparisons to other techniques, such as LQG/LTR, is not the intent of this work.

### **1.4 Thesis Outline**

This thesis consists of seven chapters. Chapter I gives overall background

and motivation for investigating weight functions in three optimal designs. These three methods are introduced, and the design plant shown to be the focus of this work.

Chapter II provides the necessary understanding of the optimal design methods. Also included is a brief review of publications that center on the mixed-sensitivity problem, one example of a 2 DOF design, and a summary of possible constraints for an unstable nonminimum phase design plant.

Chapter III develops the longitudinal normal acceleration command following model used for this F-16 example. In addition, the various methods of analyzing a compensator design are presented. These consist of examining transfer functions such as sensitivity, and time responses (i.e. for a step input).

The first design studies are the  $H_2$  ones of Chapter IV. A basic LQG-type performance index is initially examined, followed by an LQG/Sensitivity and an LQG/Tracking scheme. The purpose of the LQG design is for regulation, whereas the two designs that follow attempt to improve on performance and robustness.

Chapter V begins with an optimal  $H_\infty$  tracking design that includes weights to help system robustness. Since problems with noise attenuation will be significant because of the optimal  $H_\infty$  compensator's "D" term, a section on suboptimal  $H_\infty$  controllers is included. Hence, explanations on optimal versus suboptimal tradeoffs are also provided.

The design method used in Chapter VI is Ridgely's general mixed  $H_2/H_\infty$  optimization. A visible tradeoff in  $H_2$  and  $H_\infty$  objectives is a key to this methodology. The mixed solution algorithm is also examined, and plots of two mixed cases are compared to the separate optimal  $H_2$  and  $H_\infty$  designs. Furthermore, comments on creating a start guess for the mixed algorithm are given.

The final chapter, Chapter VII, gives the overall conclusions for this design weight study. Also included are recommendations for further work, and an overview of this thesis.

## **II. Methodology Overview and Related Work**

### **2.1 General Discussion**

This chapter is intended to lay the foundation for the specific compensator designs that will follow. First the  $H_2$ ,  $H_\infty$ , and general mixed  $H_2/H_\infty$  design procedures are explained. An understanding of these design tools is necessary before examining applications. Since complete theoretical backgrounds are not given, the reader may wish to review the references that accompany the procedure outlines. Following this methodology overview is a summary of contributions related to design weight choices applicable to aircraft. Although there are numerous examples of missile and space systems in print, only select aircraft designs are investigated due to brevity. A look at a 2 DOF example is also included since most designs will be of this type. The combination of the methodology background and example summary will aid the designer in properly applying these techniques. Only insight into weight locations and shapes is the remaining factor for a successful design application.

### **2.2 $H_2$ Optimization**

$H_2$  optimization, which parallels the popular LQG problem in the optimal output feedback case, is based on minimizing the 2-norm of a transfer function

matrix from white noise inputs to controlled outputs ( $T_{zw}$ ). Specifically, the white noise input is assumed to be zero-mean, unit intensity, and possess a Gaussian distribution. Figure 2-1 shows the basic  $H_2$  design diagram with the controlled output as  $z$ , and the white noise input as  $w$ . The remaining vectors are the controlled input to the plant  $u$ , and the measured plant output  $y$ .

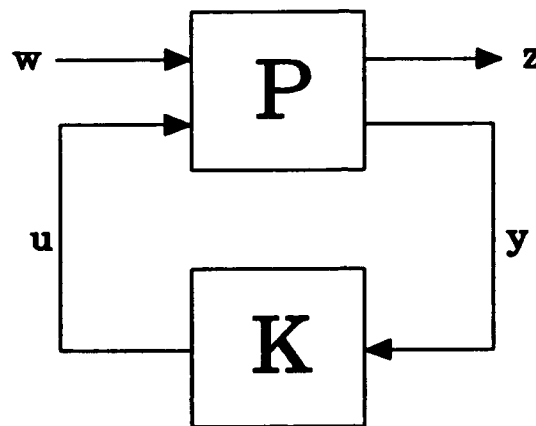


Figure 2-1.  $H_2$  Design Diagram

Again,  $P$  includes design weights. The procedure is to find the admissible  $K(s)$  that minimizes  $\|T_{zw}\|_2$ , which is equivalent to finding the admissible  $K(s)$  that minimizes the energy of  $z$  due to  $w$  (by Parseval's Theorem).  $T_{zw}$  is the closed-loop transfer function from  $w$  to  $z$ , which can be written as a linear fractional transformation (LFT) of  $P$  and  $K$  from Figure 2-1 as

$$z = [T_{zw}] w = [P_{zw} + P_{zu}K(I - P_{yu}K)^{-1}P_{yw}] w$$



The smallest possible 2-norm value of  $T_{zw}$  will be represented by  $\alpha_o$ , as in

$$\inf_{K \text{ adm}} \|z\|_2 = \inf_{K \text{ adm}} \|T_{zw}\|_2 \equiv \alpha_o$$

where

$$\|T_{zw}\|_2 = \left[ \frac{1}{2\pi} \int_{-\infty}^{+\infty} \text{tr}[T_{zw}^*(j\omega) T_{zw}(j\omega)] d\omega \right]^{1/2}$$

Before the  $H_2$  compensator can be found, the design plant  $P$  (in Figure 2-1) must be represented in state space form. The resulting nine matrices that make up  $P$  are

$$\dot{x} = Ax + B_w w + B_u u \quad (2.1a)$$

$$z = C_z x + D_{zw} w + D_{zu} u \quad (2.1b)$$

$$y = C_y x + D_{yw} w + D_{yu} u \quad (2.1c)$$

Important assumptions on these matrices consist of:

- (i)  $D_{zw} = 0$
- (ii)  $D_{yu} = 0$
- (iii)  $(A, B_u)$  stabilizable &  $(C_y, A)$  detectable
- (iv)  $D_{zu}^T D_{zu}$  full rank ;  $D_{yw} D_{yw}^T$  full rank
- (v)  $\begin{bmatrix} A - j\omega I & B_u \\ C_z & D_{zu} \end{bmatrix}$  has full column rank for all  $\omega$

$$(vi) \quad \begin{bmatrix} A - j\omega I & B_w \\ C_y & D_{yw} \end{bmatrix} \quad \text{has full row rank for all } \omega$$

All six of these conditions must be known to the designer for use in problem setup. The assumption (i) is actually a requirement for the 2-norm of the closed-loop transfer function to be finite, since noise  $w$  has infinite energy. The next condition, on  $D_{yu}$ , is not necessary but is made to simplify the problem. For stabilizing compensators to exist, (iii) must be satisfied. Both conditions in (iv) are needed to avoid singular control problems. Constraints (v) and (vi) are required for existence of stabilizing solutions to the algebraic Riccati equations (AREs) that appear in the problem solution.

A method of scaling  $u$  and  $y$ , which is internal to the solution algorithm, can be used to strengthen (iv) to  $D_{zu}^T D_{zu} = I$  and  $D_{yw} D_{yw}^T = I$ . An explanation of this scaling process, along with accompanying figures, is in [Rid91]. The revised condition will always be satisfied when the original (iv) is met, since a nonzero scaling will not alter the rank structure. Scalings on  $u$  and  $y$  are not shown in the following  $H_2$  optimization solution, i.e. they are assumed to be identity.

The  $H_2$  output feedback solution follows from [DGKF89], where the family of all admissible compensators that satisfies  $\|T_{zw}\|_2 \leq \alpha$  (with  $\alpha \geq \alpha_0$ ) is given by the LFT of  $J(s)$  and the freedom parameter  $Q(s)$ , as in Figure 2-2. For  $Q(s)$  equal to zero, the  $J_w(s)$  transfer function is equal to

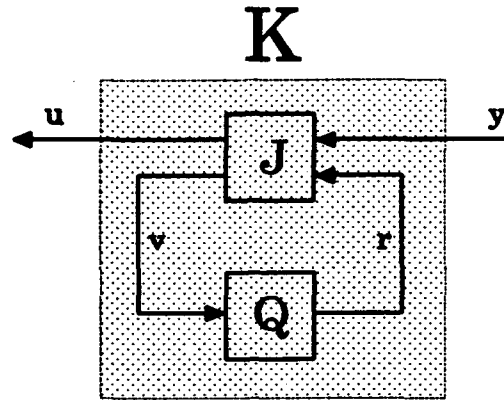


Figure 2-2. (J,Q)-Parameterization

$K(s)$  and is the unique optimal  $H_2$  compensator called  $K_{2opt}$ . With a nonzero  $Q(s)$ , suboptimal compensators can be formulated. Constraints on  $Q(s)$  in the suboptimal case are  $Q \in RH_2$ , and  $\|Q\|_2^2 \leq \alpha^2 - \alpha_o^2$ . The  $H_2$  transfer function  $J(s)$  is given by Equation (2.2), with the individual  $A_j$ ,  $B_j$ , and  $C_j$  matrices defined below it by  $A_j$ ,  $[K_f \ K_{f1}]$ , and  $[-K_c \ K_{c1}]^T$ , respectively.

$$J(s) = \left[ \begin{array}{c|cc} A_J & K_f & K_{f1} \\ \hline -K_c & 0 & I \\ K_{c1} & I & 0 \end{array} \right] \quad (2.2)$$

$$A_j = A - K_f C_y - B_u K_c$$

$$K_f = Y_2 C_y^T + B_w D_{yw}^T \quad K_{f1} = B_u$$

$$K_c = B_u^T X_2 + D_{zw}^T C_z \quad K_{c1} = -C_y$$

The  $X_2$  and  $Y_2$  matrices that appear in the components of  $J(s)$  are the

symmetric, positive semidefinite solutions to the AREs below.  $X_2$  and  $Y_2$  will be real and unique.

$$(A-B_u D_{zu}^T C_z)^T X_2 + X_2 (A-B_u D_{zu}^T C_z) - X_2 B_u B_u^T X_2 + [(I-D_{zu} D_{zu}^T) C_z]^T [(I-D_{zu} D_{zu}^T) C_z] = 0$$

$$(A-B_w D_{yw}^T C_y) Y_2 + Y_2 (A-B_w D_{yw}^T C_y)^T - Y_2 C_y^T C_y Y_2 + [B_w (I-D_{yw}^T D_{yw})][B_w (I-D_{yw}^T D_{yw})]^T = 0$$

$H_2$  designs investigated in this work are all optimal output feedback compensators, with  $\alpha = \alpha_0$  and  $Q(s) = 0$ ; therefore,  $K(s) = K_{2opt}$ . This compensator is unique, full order, and exhibits the separation structure like LQG compensators. Also notice that the optimal compensator below is strictly proper and not dependent on  $K_{c1}$  or  $K_n$ .

$$K_{2opt} = \left[ \begin{array}{c|c} A_J & K_f \\ \hline -K_c & 0 \end{array} \right]$$

### **2.3 $H_\infty$ Optimization**

The  $H_\infty$  optimization methodology, used mainly for robust control design, is based on minimizing the energy of a controlled output to a deterministic input signal that has bounded, but unknown, energy. With the input  $d$

normalized such that  $\|d\|_2 \leq 1$ , the objective is

$$\inf_{K \text{ adm}} \sup_{\|d\|_2 \leq 1} \|e\|_2 \equiv \inf_{K \text{ adm}} \|T_{ed}\|_\infty \equiv \gamma_0$$

The bounded input being referred to as  $d$ , and the controlled output as  $e$ , are to decrease the possible conflict with parameters from the  $H_2$  section. These variables give the closed-loop transfer function  $d$  to  $e$  its  $T_{ed}$  notation. The  $\infty$ -norm of  $T_{ed}$  is defined as

$$\|T_{ed}(j\omega)\|_\infty \equiv \sup_\omega \bar{\sigma}[T_{ed}(j\omega)]$$

The  $H_\infty$  block diagram, Figure 2-3, shows the bounded input  $d$  and controlled output  $e$ .

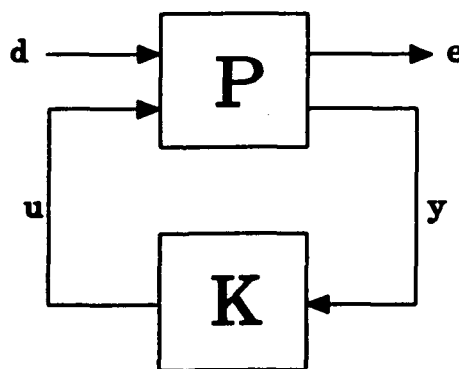


Figure 2-3.  $H_\infty$  Design Diagram

The state space solution for output feedback is also based on [DGKF89], with the actual program used in this work being the [SLC89] procedure. With the

$H_\infty$  notation comes a design plant  $P$  represented by Equation (2.3).  $P$  (as in  $H_2$ ) is linear, time-invariant, and includes design weights.

$$\dot{x} = Ax + B_d d + B_u u \quad (2.3a)$$

$$e = C_e x + D_{ed} d + D_{eu} u \quad (2.3b)$$

$$y = C_y x + D_{yd} d + D_{yu} u \quad (2.3c)$$

Assumptions on these nine  $H_\infty$  matrices are:

- (i)  $D_{ed} = 0$       (ii)  $D_{yu} = 0$
- (iii)  $(A, B_u)$  stabilizable &  $(C_y, A)$  detectable
- (iv)  $D_{eu}^T D_{eu}$  full rank ;  $D_{yd} D_{yd}^T$  full rank
- (v)  $\begin{bmatrix} A - j\omega I & B_u \\ C_e & D_{eu} \end{bmatrix}$  has full column rank for all  $\omega$
- (vi)  $\begin{bmatrix} A - j\omega I & B_d \\ C_y & D_{yd} \end{bmatrix}$  has full row rank for all  $\omega$

Again, these conditions must be known to the designer. The assumption (i), made to ease problem formulation, is not a requirement as in the  $H_2$  method because even if the closed-loop transfer function  $T_{ed}$  has a "D" term, the  $\infty$ -norm is not necessarily infinite. The condition on  $D_{yu}$  is not necessary, but simplifies the problem. For stabilizing solutions to exist, (iii) must be satisfied. Both conditions in (iv) are necessary to prevent possible singular

control problems. Conditions (v) and (vi) are required because of the solution procedure used. A complete examination of the approach assumptions for this [DGKF89] state space solution is given in [Gah92].

The same type of scaling on  $u$  and  $y$ , which is also internal to the  $H_\infty$  solution algorithm, can be used to strengthen (iv) to  $D_{eu}^T D_{eu} = I$  and  $D_{yd} D_{yd}^T = I$ . A complete description of this scaling process is in [Rid91]. The revised condition (iv) will always be satisfied when the original (iv) is met. As before, scalings will not be shown in the following  $H_\infty$  solution, i.e. they are assumed to be identity.

Because of the complication involved in parameterizing all  $H_\infty$  optimal controllers, the parameterization of all suboptimal controllers is explained. The procedure for finding the optimal value of  $\gamma$ , called  $\gamma_o$ , is an iteration technique that depends on three particular conditions. Even though this parameterization is for suboptimal controllers, a value of  $\gamma$  very close to  $\gamma_o$  can give a suboptimal controller almost the same as the optimal ( $\gamma_o$ ) one. Furthermore, it is known that the family of suboptimal controllers must satisfy  $\|T_{sd}\|_\infty < \gamma$  (with  $\gamma > \gamma_o$ ) and should yield an empty set for  $\gamma \leq \gamma_o$ . Now the parameterization can be given by  $J(s)$  in Equation (2.4).

$$J(s) = \left[ \begin{array}{c|cc} A_J & K_f & K_{f1} \\ \hline -K_c & 0 & I \\ K_{cl} & I & 0 \end{array} \right] \quad (2.4)$$

This  $J(s)$  will be completely known for a particular value of  $\gamma$ . The components of  $J(s)$  are

$$A_j = A - K_f C_y - B_u K_c + \gamma^2 Y_\infty C_c^T (C_c - D_{cu} K_c)$$

$$K_f = Y_\infty C_y^T + B_d D_{yd}^T$$

$$K_n = \gamma^2 Y_\infty C_c^T D_{cu} + B_u$$

$$K_c = (B_u^T X_\infty + D_{cu}^T C_c)(I - \gamma^2 Y_\infty X_\infty)^{-1}$$

$$K_{cl} = -(\gamma^2 D_{yd} B_d^T X_\infty + C_y)(I - \gamma^2 Y_\infty X_\infty)^{-1}$$

The separation principle in  $H_2$  optimization now falls apart because of the boldface term in  $A_j$ , which represents  $H_\infty$  coupling. As in the  $H_2$  explanation, the  $K_{cl}$  and  $K_n$  equations are not needed for the  $Q(s) = 0$  controller (the central  $H_\infty$  controller). There can be a central ( $Q(s) = 0$ )  $H_\infty$  optimal or suboptimal controller; likewise, there can be a noncentral ( $Q(s) \neq 0$ )  $H_\infty$  optimal or suboptimal controller. The  $X_\infty$  and  $Y_\infty$  matrices in the  $J(s)$  components are the solutions to the two AREs below, again without scalings.

$$(A - B_u D_{cu}^T C_c)^T X_\infty + X_\infty (A - B_u D_{cu}^T C_c) + X_\infty (\gamma^2 B_d B_d^T - B_u B_u^T) X_\infty + C_c^T (I - D_{cu} D_{cu}^T) (I - D_{cu} D_{cu}^T) C_c = 0$$

$$(A - B_d D_{yd}^T C_y) Y_\infty + Y_\infty (A - B_d D_{yd}^T C_y)^T + Y_\infty (\gamma^2 C_c^T C_c - C_y^T C_y) Y_\infty + B_d (I - D_{yd}^T D_{yd}) (I - D_{yd}^T D_{yd})^T B_d^T = 0$$



The choice of  $Q(s)$  must be stable and proper, satisfying  $Q \in RH_\infty$ , and the  $\gamma$  constraint must also be met by  $\|Q\|_\infty < \gamma$ . The three conditions that were referred to in the start of the suboptimal parameterization are:

- (i)  $H_x \in \text{dom}(\text{Ric})$  with  $X_\infty = \text{Ric}(H_x) \geq 0$
- (ii)  $H_y \in \text{dom}(\text{Ric})$  with  $Y_\infty = \text{Ric}(H_y) \geq 0$
- (iii)  $\rho(Y_\infty X_\infty) < \gamma^2$

These are also discussed in Chapter V, and depend particularly on two Hamiltonian matrices  $H_x$  and  $H_y$ .  $H_x$  is the Hamiltonian for the first ARE that yields  $X_\infty$ , and similarly  $H_y$  is the Hamiltonian for the second ARE that produces  $Y_\infty$  (see [Rid91,79-80]). The second conditions in both (i) and (ii) are to ensure positive semidefinite solutions to the AREs. The third condition written as a strict inequality depends on the spectral radius ( $\rho$ ) of the matrix  $Y_\infty X_\infty$ , and is typically an equality at the optimal solution, i.e.

$\rho(Y_\infty X_\infty) = \gamma_o^2$ . The problem that arises is in the boldface part of the  $K_c$  and  $K_{c1}$  equations of  $J(s)$ . The  $(I - \gamma^2 Y_\infty X_\infty)^{-1}$  term does not exist at

$\rho(Y_\infty X_\infty) = \gamma_o^2$ , but the problem can be removed by a descriptor system approach [GLDKS91]. This method produces a compensator with a "D" term and an order one less than the design plant (this is the case in the optimal designs of Chapter V). Remember the value of  $\gamma_o$  will be the infimum of  $\gamma$  that simultaneously satisfies all three conditions; therefore, an iterative solution technique must be utilized. A detailed description of the ARE

solutions for the  $H_\infty$  problem, particularly the  $\gamma$  domain, is given in [Li92].

The  $H_\infty$  optimal designs in this work are all central controllers, i.e.

$Q(s) = 0$ , with a unique compensator solution. Order of this optimal compensator will be one less than the order of the design plant, whereas the suboptimal solutions will be the same order as the plant.

## **2.4 Mixed $H_2/H_\infty$ Optimization**

The nonconservative tool that trades between  $H_2$  and  $H_\infty$  objectives is that developed by Ridgely [Rid91]. Because of the complexity involved in a full explanation of his theory and development, only a basic overview will be given. The need for an approach that competes  $H_2$  and  $H_\infty$  objectives is apparent from Chapter I. The objective of the mixed case is

$$\inf_{K \text{ adm}} \|T_{zw}\|_2, \text{ subject to the constraint } \|T_{ed}\|_\infty \leq \gamma$$

where  $T_{zw}$  and  $T_{ed}$  can be designed completely independent of each other.

Figure 2-4 shows the general setup for the mixed case, with the variables in the figure defined the same as before.

Two concerns that immediately arise are in the connection of these different procedures ( $H_2$  and  $H_\infty$ ) and the use of a nonzero  $Q(s)$  in the mixed problem. Regarding the later concern, this method provides a rationale for choosing a nonzero  $Q(s)$  (lowering of  $\|T_{zw}\|_2$ ), since in the previous  $H_\infty$

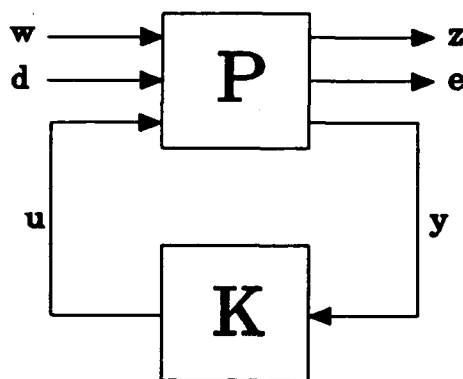


Figure 2-4. Mixed  $H_2/H_\infty$  Design Diagram

development a method for selecting a beneficial  $Q(s)$  is not given. It is important to note that the problem of choosing a  $Q(s)$  for an  $H_\infty$  design is continuously being studied. Now attention turns to adjoining the  $H_2$  and  $H_\infty$  design procedures to give this mixed methodology.

To begin with, the state space of  $P$  is now larger than that of the separate  $H_2$  and  $H_\infty$  designs. This can be seen in Figure 2-4 since there is now an additional input and output to the plant. The sixteen design plant matrices in the mixed  $P$  are

$$\dot{x} = Ax + B_d d + B_w w + B_u u \quad (2.5a)$$

$$e = C_e x + D_{ed} d + D_{ew} w + D_{eu} u \quad (2.5b)$$

$$z = C_z x + D_{zd} d + D_{zw} w + D_{zu} u \quad (2.5c)$$

$$y = C_y x + D_{yd} d + D_{yw} w + D_{yu} u \quad (2.5d)$$

The  $D_{zd}$  and  $D_{zw}$  matrices are not needed in the problem formulation. As in

the previous  $H_2$  and  $H_\infty$  discussions, many conditions are assumed for the individual matrices of Equation (2.5). For the mixed case these are basically a combination of the previous assumptions on the separate  $H_2$  and  $H_\infty$  procedures, and are given by the following:

- (i)  $D_{cd} = 0$       (ii)  $D_{zw} = 0$       (iii)  $D_{yu} = 0$
- (iv)  $(A, B_u)$  stabilizable &  $(C_y, A)$  detectable
- (v)  $D_{cu}^T D_{cu}$  full rank ;  $D_{yd} D_{yd}^T$  full rank
- (vi)  $D_{zu}^T D_{zu}$  full rank ;  $D_{yw} D_{yw}^T$  full rank
- (vii)  $\begin{bmatrix} A - j\omega I & B_u \\ C_c & D_{cu} \end{bmatrix}$  has full column rank for all  $\omega$
- (viii)  $\begin{bmatrix} A - j\omega I & B_d \\ C_y & D_{yd} \end{bmatrix}$  has full row rank for all  $\omega$
- (ix)  $\begin{bmatrix} A - j\omega I & B_u \\ C_z & D_{zu} \end{bmatrix}$  has full column rank for all  $\omega$
- (x)  $\begin{bmatrix} A - j\omega I & B_w \\ C_y & D_{yw} \end{bmatrix}$  has full row rank for all  $\omega$

First, the condition on  $D_{cd}$  being zero is for convenience in problem development. Requirement (ii) is to ensure a finite 2-norm for  $T_{zw}$ . The third condition is another assumed to make problem development easier, although it

is a practical assumption. Condition (iv) is necessary for stabilizing solutions to exist, and (v) and (vi) are for avoiding singular control problems. The remaining four conditions are duplicates of the individual  $H_2$  and  $H_\infty$  requirements that ensure admissible solutions in each case. It is again emphasized that these conditions need to be examined in the design problem formulation, and it will be seen in Chapter VI that one of these does create a problem.

For a finite 2-norm of  $T_{zw}$ , it is known that the compensator has no "D" term. With this, and  $u(s) = K(s)y(s)$ , the closed-loop system can be rewritten with a state vector that includes the compensator states as

$$\dot{\tilde{x}} = \tilde{A}\tilde{x} + \tilde{B}_d d + \tilde{B}_w w \quad (2.6a)$$

$$e = \tilde{C}_e \tilde{x} + D_{ew} w \quad (2.6b)$$

$$z = \tilde{C}_z \tilde{x} + D_{zd} d \quad (2.6c)$$

The individual closed-loop (tilde) matrices of Equation (2.6) are given by [Rid91,92-93], with the main point being that now the closed-loop transfer functions for the separate  $H_2$  and  $H_\infty$  diagrams can be written as

$T_{ed} = \tilde{C}_e (sI - \tilde{A})^{-1} \tilde{B}_d$  and  $T_{zw} = \tilde{C}_z (sI - \tilde{A})^{-1} \tilde{B}_w$ . Again the objective is to find a stabilizing  $K(s)$  that will be strictly proper and satisfies  $\|T_{ed}\|_\infty \leq \gamma$  while minimizing  $\|T_{zw}\|_2$ . With the closed-loop tilde matrices just shown, the 2-norm of  $T_{zw}$  can be expressed as  $\|T_{zw}\|_2^2 = \text{tr}[Q_2 \tilde{C}_z^T \tilde{C}_z]$ . The  $Q_2$  that appears in this new expression is the symmetric, positive semidefinite solution

to the Lyapunov equation

$$\tilde{A}Q_2 + Q_2\tilde{A}^T + \tilde{B}_w\tilde{B}_w^T = 0 \quad (2.7)$$

This enforces that  $\tilde{A}$  is stable, and  $K(s)$  is stabilizing, through Lyapunov theory. With a stabilizing solution guaranteed from the Lyapunov equation, the Bounded Real Lemma [Wil71] proves that the symmetric, positive semidefinite solution to the following ARE gives  $\|T_{cd}\|_\infty \leq \gamma$ .

$$\tilde{A}Q_\infty + Q_\infty\tilde{A}^T + \gamma^{-2}Q_\infty\tilde{C}_c^T\tilde{C}_cQ_\infty + \tilde{B}_d\tilde{B}_d^T = 0 \quad (2.8)$$

Now the mixed case can be formulated as finding the  $K(s)$  (strictly proper) that minimizes the index

$$J(A_c, B_c, C_c) = \text{tr}[Q_2\tilde{C}_z^T\tilde{C}_z] \quad (2.9)$$

subject to Equation (2.7) and such that

$$\tilde{A}Q_\infty + Q_\infty\tilde{A}^T + \gamma^{-2}Q_\infty\tilde{C}_c^T\tilde{C}_cQ_\infty + \tilde{B}_d\tilde{B}_d^T = 0$$

has a real, symmetric, positive semidefinite solution [Rid91]. This problem statement immediately lends itself to a Lagrange multiplier formulation because of the performance objective and the two constraint equations. Let the Lagrange multiplier mixed problem be to minimize Equation (2.10).

$$\begin{aligned}\mathcal{L} = & \text{tr}[Q_2 \tilde{C}_2^T \tilde{C}_2] + \text{tr}\{[\tilde{A}Q_2 + Q_2 \tilde{A}^T + \tilde{B}_w \tilde{B}_w^T]X\} \\ & + \text{tr}\{[\tilde{A}Q_\infty + Q_\infty \tilde{A}^T + \gamma^{-2}Q_\infty \tilde{C}_c^T \tilde{C}_c Q_\infty + \tilde{B}_d \tilde{B}_d^T]Y\}\end{aligned}\quad (2.10)$$

where  $X$  and  $Y$  are Lagrange multiplier matrices. The unknowns needed are  $X$ ,  $Y$ ,  $A_c$ ,  $B_c$ ,  $C_c$ ,  $Q_2$ , and  $Q_\infty$ . The assumptions for this minimization are  $Q_2 = Q_2^T \geq 0$  and  $Q_\infty = Q_\infty^T \geq 0$ . For this problem, the seven first order necessary conditions for a minimum are given by [Rid91,97-98]. The solution to these is found to lie on the boundary of the  $\infty$ -norm constraint when the  $H_2$  and  $H_\infty$  objectives are competing [Rid91, Theorem 4.2.3]. For theoretical interest into Ridgely's full order contributions, the theorems presented in [Rid91,100-109] are critical and give the foundation of his approach. A summary of additional information on the mixed solution is:

i) No mixed solution exists for  $\gamma < \gamma_0$ , and  $K_{2opt}$  is equivalent to the solution for  $\gamma \geq \gamma_2$  (where  $\gamma_2$  is the value of  $\|T_{ed}\|_\infty$  using  $K_{2opt}$ ) [Rid91, Theorems 4.2.1 and 4.2.2].

ii) The mixed solution comes from seven first order necessary conditions, which are highly coupled and nonlinear. This motivates the numerical method that is used by Ridgely and in this work.

iii) For  $\gamma_0 < \gamma < \gamma_2$ , a neutrally stabilizing ARE solution is required. Also a Lyapunov equation that has no constant term must be solved.

This last requirement (iii) leads to a suboptimal derivation to allow a

numerical solution. The modified "suboptimal" performance index, for  $\mu$  between zero and one, of Equation (2.9) is

$$J_\mu(A_c, B_c, C_c) = (1-\mu) \operatorname{tr}[Q_2 \tilde{C}_2^T \tilde{C}_2] + \mu \operatorname{tr}[Q_\infty \tilde{C}_c^T \tilde{C}_c]$$

The benefit of this is that the original solution (minimize Equation (2.9)) can be approached by driving  $\mu$  very close to zero, and the iteration procedure can start with a  $\mu$  value near one. For  $\mu = 1$ , the mixed problem yields the equivalent central  $H_\infty$  suboptimal compensator. The Lyapunov equation that had no constant term, which is one of the necessary conditions that must be solved, now has a constant term so that a Lyapunov solver can be used. Also, the ARE that required a neutrally stabilizing solution now requires a stabilizing solution. The seven necessary conditions for this suboptimal mixed procedure are in [Rid91, 116-117]. The important theorem of the suboptimal method approaching the optimal one, when  $\mu$  goes to zero, is given by [Rid91, Theorem 5.1.2]. The suboptimal Lagrangian is now

$$\begin{aligned} \mathcal{L}_\mu = & (1-\mu) \operatorname{tr}[Q_2 \tilde{C}_2^T \tilde{C}_2] + \mu \operatorname{tr}[Q_\infty \tilde{C}_c^T \tilde{C}_c] \\ & + \operatorname{tr}\{[\tilde{A}Q_2 + Q_2\tilde{A}^T + \tilde{B}_w\tilde{B}_w^T]X\} \\ & + \operatorname{tr}\{[\tilde{A}Q_\infty + Q_\infty\tilde{A}^T + \gamma^2 Q_\infty \tilde{C}_c^T \tilde{C}_c Q_\infty + \tilde{B}_d\tilde{B}_d^T]Y\} \end{aligned}$$

With the problem set up in this suboptimal context, the numerical solution is ready to be found for chosen values of  $\mu$ . The algorithm selected to solve this optimization problem, and a detailed explanation of the procedure for its use,



is discussed in Chapter VI. Since the three design techniques have been presented, an examination of current studies that yield weight locations and shapes is the focus.

## **2.5 Review of Related Work**

The majority of published material on selecting weights is for the mixed-sensitivity problem. A weight selection process includes choosing the transfer function to weight and designing the weight to put on this transfer function. In the mixed-sensitivity design, the transfer functions that are weighted consist of the sensitivity,  $S(s)$ ; the complimentary sensitivity,  $T(s)$ ; and the control sensitivity,  $K(s)S(s)$ . Recall  $S(s) = (1-G(s)K_b(s))^{-1}$  and  $T(s) = G(s)K_b(s)S(s)$ , where  $K_b(s)$  is the feedback compensator. These transfer functions, and their relevance to the closed-loop system are covered in Chapter III. The control sensitivity is commonly excluded from this type of design since it can be equated to  $T(s)$ . Easily seen in the SISO case,  $K_b(s)S(s)$  is identical to  $T(s)$  multiplied by the inverse of the plant. Because a large amount of examples are the mixed-sensitivity type, this translates into most designs being 1 DOF because the three mixed-sensitivity transfer functions depend only on the compensator in the feedback loop,  $K_b(s)$ . Now that the transfer functions to weight are known, consider how the shape of each weight is chosen.

Coincident with selecting weight shapes for this mixed-sensitivity problem,

a review of Chapter 4 in [DFT92] may be helpful to the reader. This reference gives a complete background look at  $S(s)$  and  $T(s)$ , and gives insight into ways to shape the weights on these transfer functions. The basis of the weight discussion is the Nyquist plot and the Small Gain Theorem [Zam66], with the result being a "nominal performance" constraint on  $S(s)$  and a "robust stability" constraint on  $T(s)$ . Also in [DFT92], Chapter 6 covers plant design limitations that are dependent on algebraic relationships and the necessity for closed-loop stability.

A common aircraft example is the  $H_2$  and  $H_\infty$  mixed-sensitivity fighter designs in [ChS88]. The unstable MIMO plant is for a longitudinal flight controller and uses the same weight selections for both the  $H_2$  and  $H_\infty$  designs. The weight on  $S(s)$  has a dc gain of 40 dB, a pole at 0.01 rad/sec, and a zero at 100 rad/sec. The weight on  $T(s)$  has a pair of zeros at the origin with a gain of 60 dB at 1 rad/sec. Note that these weights are the inverse of the desired transfer function magnitudes. Since these weights form penalties in the optimization, they will drive the transfer function magnitudes to their inverse.

A design using the exact setup as the [ChS88] fighter example is that of [Har90]. This is again a MIMO design on the longitudinal dynamics of a fighter, the F-18. This plant is stable at the chosen design point. Like [ChS88], both  $H_2$  and  $H_\infty$  optimal compensators are found. The first design in [Har90] uses the identical weight shapes given in [ChS88], while a second

attempt contains a modification to the weight on  $S(s)$  because of practical limitations on actuator deflections and rates. In this case  $T(s)$  instead of  $K_b(s)S(s)$  is weighted in the designs.

The mixed-sensitivity approach is also examined by [Ino90], with detailed explanations on weight shape selections for  $S(s)$ ,  $T(s)$ , and  $K_b(s)S(s)$ . Examples in [Ino90] also show a plant that is inner loop "conditioned" through classical techniques, followed by the use of the optimal control design on this "conditioned" plant. The design examples in [Ino90] are not for specific aircraft as in the previous references, but the choice of including this reference is based on the thorough descriptions of weight designs.

Although most references discuss weight shapes for the mixed-sensitivity problem, they address only a 1 DOF design. A major point in this thesis is not only designing for good sensitivity, like these methods can provide, but also for closed-loop tracking. Because of the necessity for tracking, a 2 DOF controller will be utilized for many designs. This warrants a summary of a recent 2 DOF design.

In most 2 DOF tracking designs the transfer function  $S(s)G(s)K_f(s)$ , where  $K_f(s)$  represents the feedforward compensator, is weighted in addition to the mixed-sensitivity ones. This transfer function is for closed-loop tracking and includes both the feedforward and feedback compensators. The paper of [MrR92], on which this work follows, is a collection of 2 DOF designs using three optimization techniques. The different designs come from using these

methods ( $H_2$ ,  $H_\infty$ , and mixed  $H_2/H_\infty$ ) on specific parts of an F-16 longitudinal tracking diagram. The plant is unstable, nonminimum phase, and basically the same plant used in this work. The tracking weight chosen in [MrR92] is a low-pass filter with a dc gain of 40 dB, and a pole at 0.02 rad/sec. The only other frequency weight in this design is on  $S(s)$ ; a dc gain of 40 dB, a zero at 1 rad/sec, and poles at 0.01 and 1000 rad/sec.

With the combination of the overview on optimization techniques and related work in choosing which transfer functions to weight (and weight shapes), the specific thesis problem can be set up. The development of the design model and methods to evaluate the compensators that result from the optimization routines are discussed in the upcoming chapter.

### **III. Pre-Design Process**

#### **3.1 F-16 Model Development**

This section presents the buildup of the longitudinal short period approximation model, and is followed by discussions on the evaluation process and design limitations. The development of the acceleration command following plant consists of the combination of an actuator servo, the short period approximation of the F-16 (for elevator commands), and a time delay representing the accelerometer measurement hold. The flight condition for this linearized model is Mach 0.6 at sea level. The plant used for compensator designs utilizes the short period mode only, whereas a "truth" plant that also contains the phugoid roots will be used as a stability measure and for one simulation. The design model that contains the short period mode (with servo and approximated time delay) is referred to as the lower order model (LO), while the one that includes the phugoid (along with increased orders of the servo and time delay approximation) is called the higher order model (HI). Components that make up these systems are a combination of those used in [Bic89] and [MrR92].

A series connection of the first order servo, the short period dynamics, and a first order Padé approximation is used for the lower order model buildup. The lower order model has four states; two from the short period

roots, and one each from the servo and time delay. The state space representations for the actuator, the short period plant, and the first order Padé approximation are shown in Equations (3.1) through (3.3), respectively.

$$\begin{bmatrix} \dot{\delta}_e \end{bmatrix} = \begin{bmatrix} -20 \end{bmatrix} \begin{bmatrix} \delta_e \end{bmatrix} + \begin{bmatrix} 20 \end{bmatrix} \begin{bmatrix} \delta_{e\_comm} \end{bmatrix} \quad (3.1)$$

$$\begin{bmatrix} \dot{\alpha} \\ \dot{q} \end{bmatrix} = \begin{bmatrix} -1.491 & 0.996 \\ 9.753 & -0.960 \end{bmatrix} \begin{bmatrix} \alpha \\ q \end{bmatrix} + \begin{bmatrix} -0.188 \\ -19.04 \end{bmatrix} \begin{bmatrix} \delta_e \end{bmatrix} \quad (3.2a)$$

$$\begin{aligned} \begin{bmatrix} \dot{d} \end{bmatrix} &= \begin{bmatrix} -40 \end{bmatrix} \begin{bmatrix} d \end{bmatrix} + \begin{bmatrix} 1 \end{bmatrix} \begin{bmatrix} N_z \end{bmatrix} \\ \begin{bmatrix} N_{z\_del} \end{bmatrix} &= \begin{bmatrix} 80 \end{bmatrix} \begin{bmatrix} d \end{bmatrix} + \begin{bmatrix} -1 \end{bmatrix} \begin{bmatrix} N_z \end{bmatrix} \end{aligned} \quad (3.3)$$

where the servo input  $\delta_{e\_comm}$  is the input to the system,  $\delta_e$  the elevator deflection,  $\alpha$  the angle-of-attack,  $q$  the pitch rate,  $N_z$  the normal acceleration, and  $N_{z\_del}$  the delayed normal acceleration. Equation (3.1), with a pole at -20, is a first order approximation of the aircraft's servo. Equation (3.2a), the short period approximation, can be represented in angular units of radians or degrees since all variables are angular measures. Radians will be used in the development of state space models in this chapter, although simulation outputs will be shown in degrees. The short period roots of Equation (3.2a) are 1.903 (unstable) and -4.354, and the reason this is (3.2a) is that the "C" and "D" matrices for the acceleration feedback system have not been derived at this

point. Examining Equation (3.3), the "d" state is only a dummy state used to represent the delay from the digital sampling of acceleration. A period of 0.05 seconds is chosen as a reasonable measure for this delay, and results in the state space of Equation (3.3) when using a first order Padé approximation. This approximation has a pole at -40, and introduces a nonminimum phase zero at +40.

In deriving the equation for normal acceleration, the location where this value is measured must be considered. For F-16 acceleration command following this measurement is needed at the pilot's location. The measurement is in the body's z-axis, with a positive acceleration up, and the resulting expression in G-level. The linearized equation below gives the normal acceleration at the pilot's seat with a positive measurement up [Bic89].

$$N_z = -[U_0(\dot{\alpha} - q) - X_a \dot{q}] / 32.2 \quad (3.4)$$

where  $X_a$  is the distance from the aircraft's center-of-gravity to the accelerometer location, and  $U_0$  is the forward velocity. The output acceleration,  $N_z$ , is in G-level for angular units in radians.  $X_a$  is chosen as 14 feet for the F-16, and from the flight condition of the linearized aircraft model  $U_0$  is 670 feet/sec. Utilizing Equations (3.2a) and (3.4), the "C" and "D" matrices to complete Equation (3.2a) can be found. This allows the

series connection of the design model components. With the above mentioned values for  $X_s$  and  $U_0$ , the following can be added to Equation (3.2a)

$$[N_z] = [35.264 \quad -0.334] \begin{bmatrix} \alpha \\ q \end{bmatrix} + [-4.367] [\delta_e] \quad (3.2b)$$

Now the first order servo is connected in series to the plant, and then this combination is joined with the first order Padé approximation. The design model as represented below is now complete.

$$\begin{bmatrix} \dot{\delta} \\ \dot{\alpha} \\ \dot{q} \\ \dot{d} \end{bmatrix} = \begin{bmatrix} -20.0 & 0 & 0 & 0 \\ -0.188 & -1.491 & 0.996 & 0 \\ -19.04 & 9.753 & -0.96 & 0 \\ -4.367 & 35.264 & -0.334 & -40 \end{bmatrix} \begin{bmatrix} \delta \\ \alpha \\ q \\ d \end{bmatrix} + \begin{bmatrix} 20 \\ 0 \\ 0 \\ 0 \end{bmatrix} [\delta_{e\_cmd}] \quad (3.5)$$

$$[N_{z\_cmd}] = [4.367 \quad -35.264 \quad 0.334 \quad 80] \begin{bmatrix} \delta \\ \alpha \\ q \\ d \end{bmatrix} + [0] [\delta_{e\_cmd}]$$

The higher order model is not shown connected in series like the lower order model since the higher order one will only be used to aid in the evaluation of controllers in Simulink™ [Sim92], not in the actual compensator designs. The simulation models will be explained in the next section. A fourth order Padé approximation is used to obtain transfer functions for the



higher order model, and a fourth order servo is combined with the fourth order "truth" plant (two extra plant states are necessary for the addition of the phugoid roots) to yield a total twelfth order system. The servo used in the higher order system is

$$\frac{\delta_e(s)}{\delta_{e_{\text{comm}}}(s)} = \frac{1.491 \times 10^7}{(s+20.2)(s+144.8)(s^2+105.1s+5100)} \quad (3.6)$$

Again for the "truth" plant the phugoid roots are included and the result is the fourth order state space model of Equation (3.7). The added phugoid roots are located at  $-0.0086 \pm 0.071j$ .

$$\begin{bmatrix} \dot{u} \\ \dot{\alpha} \\ \dot{\theta} \\ \dot{q} \end{bmatrix} = \begin{bmatrix} -0.01485 & 37.382 & -32.2 & -17.94 \\ -0.00008 & -1.491 & -0.0013 & 0.996 \\ 0 & 0 & 0 & 1 \\ -0.00036 & 9.753 & 0.00029 & -0.96 \end{bmatrix} \begin{bmatrix} u \\ \alpha \\ \theta \\ q \end{bmatrix} + \begin{bmatrix} 0.00214 \\ -0.188 \\ 0 \\ -19.04 \end{bmatrix} [\delta_e] \quad (3.7)$$

$$[N_z] = [0.0015 \quad 35.264 \quad 0.0272 \quad -0.334] \begin{bmatrix} u \\ \alpha \\ \theta \\ q \end{bmatrix} + [-4.366] [\delta_e]$$

where  $u$  is the forward velocity and  $\theta$  the pitch angle. State units in the above equation are  $u$  (ft/sec),  $\alpha$  (radians),  $\theta$  (radians),  $q$  (radians/sec), and  $N_z$  again in G's. The fourth order Padé transfer function for a 0.05 second delay from Pro-Matlab™ [PM90] is Equation (3.8).

$$\frac{N_{z_{HI}}(s)}{N_z(s)} = \frac{s^4 - 400s^3 + 7.2 \times 10^4 s^2 - 6.72 \times 10^6 s + 2.688 \times 10^8}{s^4 + 400s^3 + 7.2 \times 10^4 s^2 + 6.72 \times 10^6 s + 2.688 \times 10^8} \quad (3.8)$$

The above equation is only used in finding transfer functions for the higher order model (HI); in time simulations a zero order hold replaces it. A complete listing of all state space matrices along with associated zeros and poles is provided in Appendix A.

For the differences in the lower versus higher order magnitudes, Figure 3-1 shows that the midrange frequency correlation is very good. Outside of this midrange, however, there is quite a large difference in magnitude. The higher order model is the dashed line, showing the additional

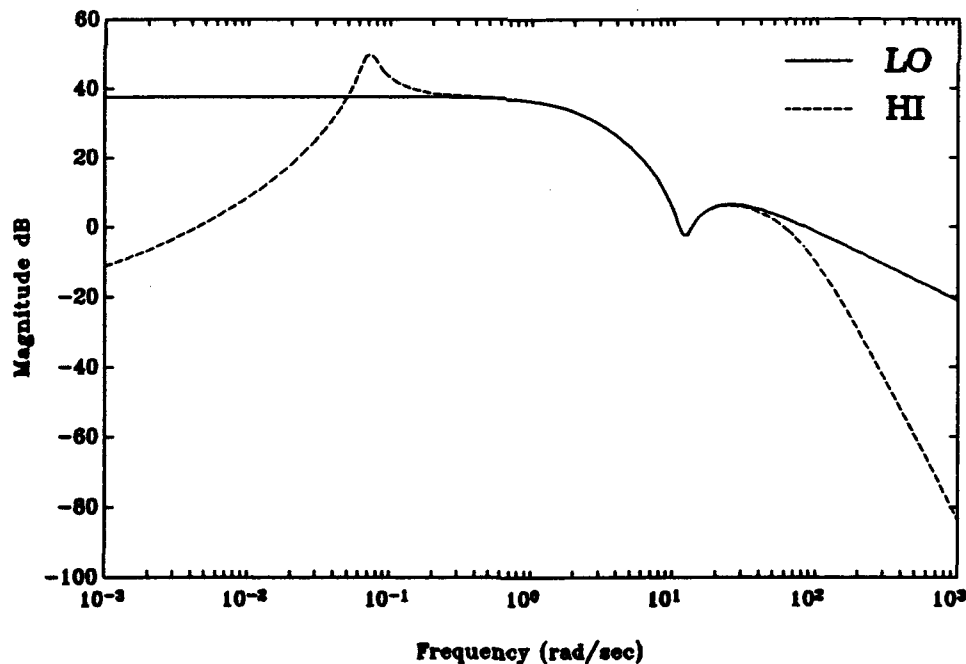


Figure 3-1. Lower Order Plant Magnitude Vs Higher Order

phugoid roots that stand out at low frequency; furthermore, the higher order model has a fourth order servo that can be seen to roll off much steeper than the first order case. The difference in going from a first order Padé to the fourth order one is not a factor in the magnitude plot since a time delay can be thought of as a pure phase shift. Magnitude differences in these models can also be found in a multiplicative or plant additive type of uncertainty [Dai90]. These uncertainty plots appear as Figures 3-2 and 3-3, respectively. Again, the low frequency uncertainty is dominated by the added phugoid roots, and the high frequency by the difference in servo dynamics. Now that the aircraft model is familiar, the compensator evaluation setup is examined.

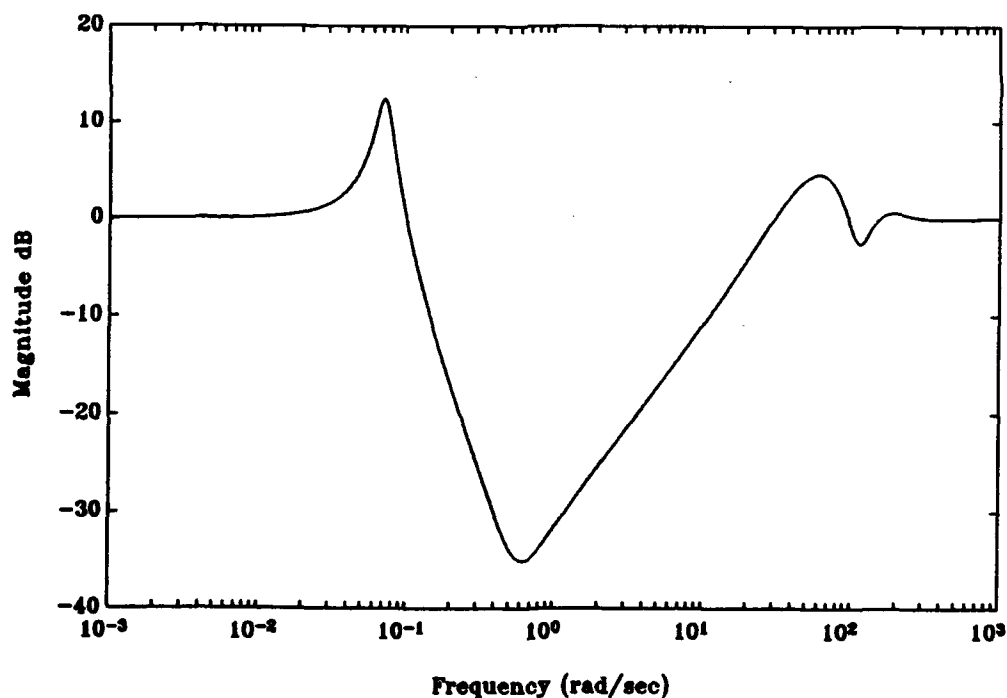


Figure 3-2. Multiplicative Uncertainty

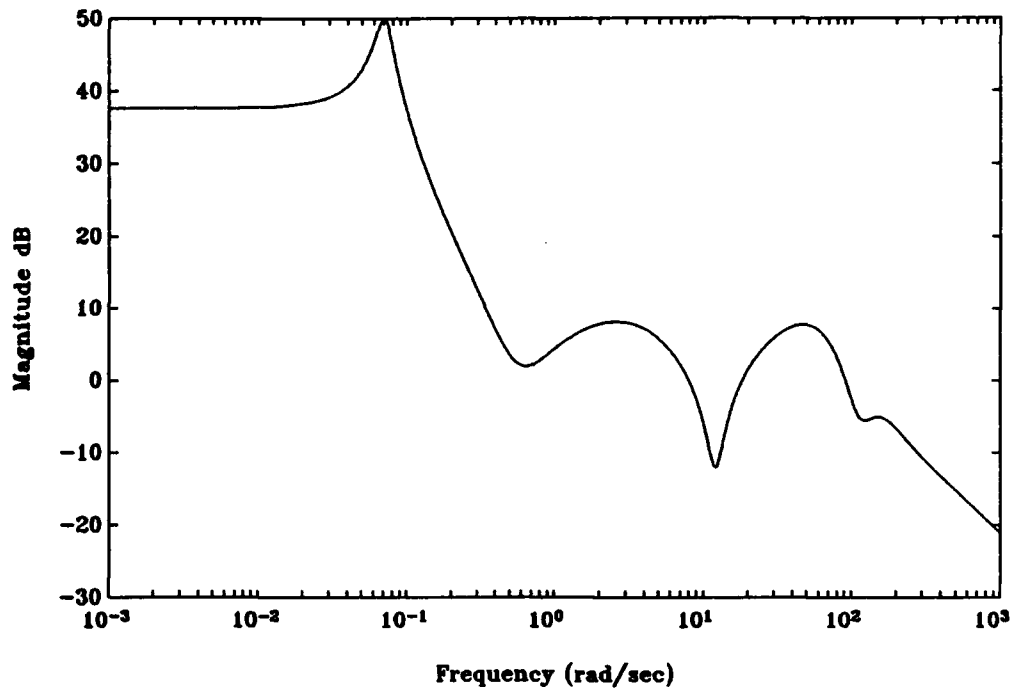


Figure 3-3. Plant Additive Uncertainty

### **3.2 Closed-Loop Evaluation Models**

The model used in finding transfer functions and in the simulation of lower order time responses is Figure 3-4. This diagram represents several models in itself. First, it serves as the closed-loop model that a controller is designed for. Therefore, it is also the model that remains after design weights are removed. The actual simulations for the lower order system ( $N_z$  doublet,  $N_z$  step, and  $\alpha$  state perturbation) are based on this diagram since it is used for the original compensator design. Hence, the closed-loop transfer functions are derived from Figure 3-4. Following the lines of deriving the closed-loop transfer functions, this diagram also serves as the transfer function model used

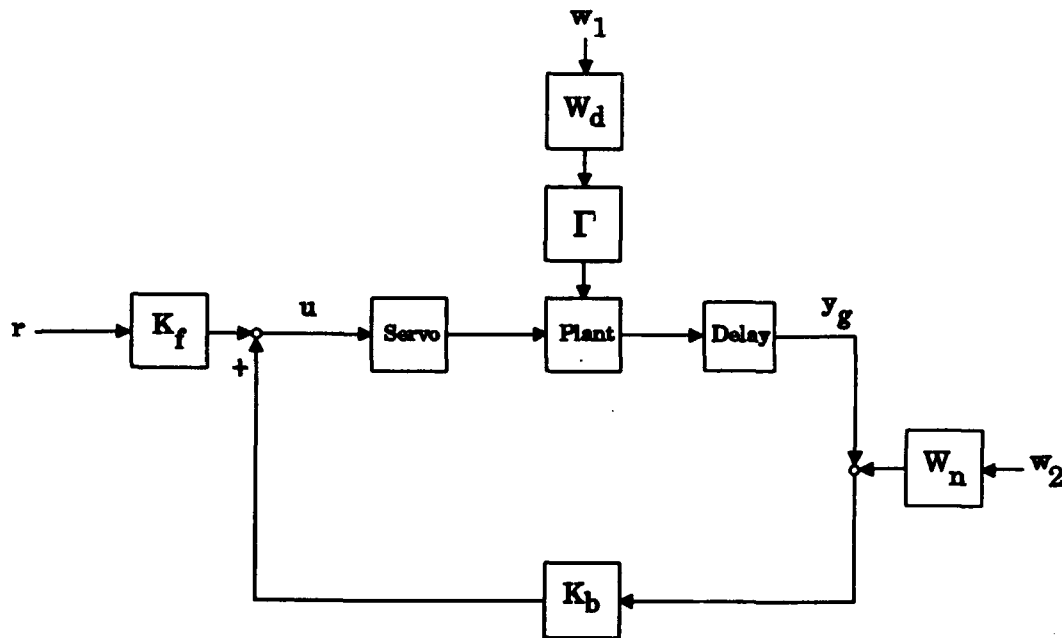


Figure 3-4. Transfer Function/Lower Order Simulation Model

in Simulink™. Note that the transfer function models for both the higher and lower order models follow this same structure. Open and closed-loop transfer functions from any points on this diagram are found by just adding input/output blocks to the Simulink™ model. By examining Figure 3-4, Laplace domain transfer functions can be obtained for the normal acceleration plant output ( $y_g$ ) and the control usage ( $u$ ), from both the white noise inputs ( $w$ ) and the commanded input ( $r$ ). These transfer functions are Equation (3.9) for a 1 DOF system, with  $G_{rd}(s)$  and  $W_n$  known. Note that for a 2 DOF system, the tracking closed-loop transfer function from  $r$  to  $y_g$  in Equation (3.9) is  $S(s)G(s)K_f(s)$ , not  $-T(s)$ . The differences in the 1 DOF and 2 DOF systems are examined in the  $H_2$  designs of Chapter IV.

$$\begin{aligned} y_g(s) &= -T(s)r + S(s)G_{rd}(s)w_1 + T(s)W_n w_2 \\ u(s) &= K_f(s)S(s)r + K_b(s)S(s)G_{rd}(s)w_1 + K_b(s)S(s)W_n w_2 \end{aligned} \quad (3.9)$$

where  $S(s) = (1-G(s)K_b(s))^{-1}$ ,  $T(s) = S(s)G(s)K_b(s)$ , and

$G_{rd}(s) = C_g(sI-A_g)^{-1}\Gamma W_d(s)$  for a SISO case. From the definitions of  $S(s)$  and

$T(s)$ , which are explained at the end of this section, it is clear that

$S(s)-T(s) = 1$  for this positive feedback system. In Equation (3.9) the  $G_{rd}(s)$  transfer function represents a disturbance entering at the plant output, although in the diagram (Figure 3-4) the actual disturbance is shown directly entering the plant. This wind gust feedthrough is plotted in Figure 3-5 and

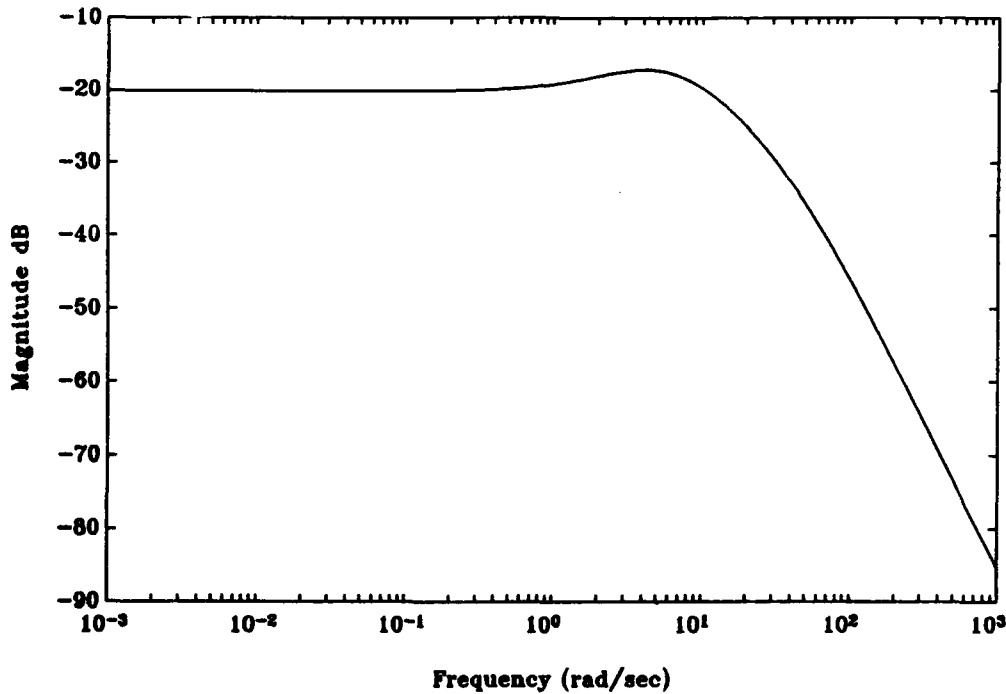


Figure 3-5. Magnitude of  $G_{rd}(s)$

will be important in frequency weighting strategies. The magnitude plot clearly shows higher gain at low frequencies, below around 10 rad/sec, with a low frequency gain of 0.1 (-20 dB). The value of  $W_a$  in Equation (3.9), and in the design/simulation models, is chosen to be 0.025 G's.

The wind disturbance that enters the plant as an  $\alpha$  perturbation is a Haines approximation to the Von Karman model represented by  $W_d(s)$  [ACD77]. The Von Karman wind disturbance model and the Haines approximation give the state variable model in Equation (3.10).

$$\dot{x}_d = -2\left(\frac{U_0}{L}\right)x_d + \frac{2\sigma}{\sqrt{\pi LU_0}} w \quad (3.10)$$

where  $U_0$  is the aircraft forward velocity in feet/sec,  $L$  is the scale length in feet,  $w$  the white noise input, and  $\sigma$  is the level of disturbance. Typical values for this disturbance level are given in [ACD77]. The value chosen for  $\sigma$ , 6 ft/sec, is the same as in [MrR92]. Completing the other variables in Equation (3.10) are the scale length  $L = 200$  feet, and the aircraft speed of  $U_0 = 670$  feet/sec. With the above values in the Von Karman model approximation, the wind disturbance is

$$\begin{aligned} \dot{x}_d &= [-6.7][x_d] + [0.0187][w] \\ \zeta &= [1][x_d] + [0][w] \end{aligned} \quad (3.11)$$

In Equation (3.11),  $\zeta$  is the wind disturbance output in radians. As mentioned previously, the wind enters the system as a perturbation in  $\alpha$ , represented by the static  $\Gamma$  matrix in Figure 3-4. This  $\Gamma$  matrix for the lower order design model is  $[0, -1.491, 9.753, 35.264]^T$ , i.e. the second column of Equation (3.5). In the same fashion for the higher order model, the  $\Gamma$  matrix is the second column of Equation (3.7).

The RMS value of the wind disturbance model for a unit intensity white noise is used in the disturbance model, causing the white noise input to the wind model in Simulink™ to be multiplied by a 12.23 value. The reason for this is that the Simulink™ white noise block does not produce the noise with intensity one, rather a "pseudo" white noise with  $\text{RMS} = 1$ . The value of 12.23 is the wind transfer function's RMS divided by the wind model output RMS for the Simulink™ white noise. A Lyapunov equation on the wind disturbance state space, Equation (3.11), gives the RMS for a zero-mean white noise of unit intensity [KwS72]. The RMS of the wind transfer function output is found by running the Simulink™ white noise through the wind gust transfer function, then calculating the standard deviation of the output (zero-mean signals are assumed). The mean was verified as being of small magnitude in cases of 1000 points, and as such is not subtracted from the input signal. The mean not being exactly zero will surface in some simulation plots, but does not alter the point of showing general trends. Also important is the fact that changing the sample times of simulations can change the RMS



of the wind transfer function output, but the only time lengths that are used (5 and 10 seconds) have RMS values within five percent of each other. The same scale value is subsequently used for both simulation time lengths because of this small difference. The seed, which operates on Simulink™ just as in Pro-Matlab™, is also held constant for the wind noise input since changing this can significantly alter the output RMS of the wind model. A different seed is used for the measurement noise to prevent any correlation.

Returning to the sensitivity transfer functions  $S(s)$ ,  $T(s)$ , and  $K_b(s)S(s)$ , these can be explained easier with the combination of Equation (3.9) and Figures 3-2 and 3-3. Possible weight shapes for these transfer functions were examined briefly in Chapter II for related work, but the significance of these was not given. Sensitivity is the response of the feedback system to disturbances at the plant output. It can also be explained in terms of the sensitivity of the closed-loop system to infinitesimal perturbations in the plant [DFT92].  $S(j\omega)$  having a small magnitude (note that  $s = j\omega$ ) implies that the closed-loop system is insensitive to output disturbances and plant variations. At frequencies where  $|S(j\omega)| > 1$ , the feedback system actually amplifies the disturbance input. For large loop gains, i.e. large  $|G(j\omega)K_b(j\omega)|$ , the magnitude of sensitivity is approximately the inverse of the loop gain. For small loop gains,  $|S(j\omega)|$  approaches unity (0 dB). Complimentary sensitivity represents the response of the closed-loop system to sensor noise. The inverse of  $|T(j\omega)|$  is also a measure of stability margin against unstructured

multiplicative uncertainty [FrL88]. A small magnitude of  $T(j\omega)$  reduces the sensor noise for the closed-loop system, whereas  $|T(j\omega)| > 1$  amplifies the sensor noise.  $|T(j\omega)|$  follows the loop gain at high frequencies, and is approximately unity (0 dB) at low frequencies. Sensor noise and disturbance feedthrough to the plant input (or control usage  $u$ ) is determined by  $|K_b(j\omega)S(j\omega)|$ , as in Equation (3.9), and this magnitude is also the inverse of allowable plant additive uncertainty. At low frequencies and high compensator magnitude,  $|K_b(j\omega)S(j\omega)|$  is approximately the reciprocal of the plant magnitude. With the model buildup and evaluation schemes covered, a continuation of the discussion on sensitivity transfer functions is given for limiting factors in this F-16 design.

### **3.3 Design Limitations**

This section presents possible limitations that affect a design for an unstable nonminimum phase plant, and is mainly a combination of [FrL88] and [DFT92]. It is well known that poles and zeros of a plant in the right-half-plane (RHP) can cause design specifications to not be achievable; therefore, an investigation of possible difficulties is warranted.

The magnitude of  $S(s)$  is the reciprocal of the distance from the Nyquist plot of  $G(s)K_b(s)$  to the critical point, since  $S(s) = (1 - G(s)K_b(s))^{-1}$ .  $|S(j\omega)|$  is less than one where the Nyquist plot of  $G(s)K_b(s)$  is outside of the unit circle centered at the critical point, and  $|S(j\omega)|$  is greater than one when the plot is

inside of the unit circle. This can be related to stability since a nearly unstable system will have a large  $\|S\|_{\infty}$  and comes close to the Nyquist plot critical point. Classical gain and phase margins only measure the distance from the critical point to the Nyquist plot in certain directions. Furthermore, large classical margins can be evident even when the Nyquist plot comes close to the critical point. For this reason the simultaneous changes in gain and phase represented by the complex margins will be the concentration, since these are a worst case margin. The value of  $\|S\|_{\infty}$  is independent of frequency though, and a large perturbation in  $G(s)K_b(s)$  at frequencies away from the critical point may be possible. In compensator evaluations, the complex margins will be given by  $\|S\|_{\infty}$  and  $\|T\|_{\infty}$  [Dai90].

Nonminimum phase zeros of the open-loop transfer function create a direct analytical tradeoff in a design on  $S(s)$ . The result is that desirable magnitudes of  $S(s)$  at certain frequencies must be given up to improve the sensitivity magnitude at other frequencies [FrL88]. It is not possible to gain a given amount of  $|S(j\omega)|$  at one frequency band by allowing  $|S(j\omega)|$  to exceed one by a small amount over a large frequency range, when a RHP zero is in the plant. This phenomenon is called the "waterbed effect" and limits the effective length of the  $j\omega$ -axis [DFT92]. The "waterbed effect" differs from the Bode area rule on sensitivity magnitude. For this F-16 plant, the Bode area rule is not valid since there is a RHP pole, but a sensitivity area rule has been extended by [FrL88] for unstable plants. The results of this extension

are that the area above the 0 dB line for  $|S(j\omega)|$  exceeds the area below  $|S(j\omega)|$  (for a linear frequency scale), and the actual area difference depends on the location of the unstable pole. Bode's method gives equal areas above and below 0 dB. A formula for finding a bound on the smallest value of  $\|S\|_{\infty}$ , that depends on the Blaschke product and the location of RHP poles/zeros, is given by [Mid91].

To summarize knowledge on  $S(s)$  for this plant, it is known that an area rule does apply and that the area below the  $|S(j\omega)| = 0$  dB line cannot arbitrarily be traded for an area above 0 dB because of the RHP zero. So the result is that if  $|S(j\omega)|$  is pushed down at certain frequencies, including a peak, the magnitude has to pop up at other frequencies.

Complimentary sensitivity,  $T(s)$ , also has constraints due to this F-16 design plant. The effect of RHP poles in  $G(s)K_b(s)$  on  $T(s)$  parallels the development of RHP zeros limiting sensitivity. Similar to  $S(s)$ , properties of  $T(s)$  must be traded at different frequencies. Equation (3.3.6) of [FrL88] gives the integral constraint on  $T(s)$ , and shows that since  $T(s)$  is related to multiplicative uncertainty that a tradeoff of  $|T(j\omega)|$  will affect both the allowable uncertainty and sensor noise attenuation. According to [FrL88], design tradeoffs on  $T(s)$  are aggravated by RHP zeros. As in the sensitivity case, a formula for finding the smallest value of  $\|T\|_{\infty}$  is given by [Mid91].

In this section some possible designs problems for unstable, nonminimum phase plants have been examined. Other factors, such as the initial response

for a nonminimum phase plant being in the reverse direction, do not present significant difficulties in this case. These limitations, combined with the F-16 model buildup and compensator evaluation scheme, complete the preliminary design process. Now weight locations and shapes can be investigated, with the first designs utilizing  $H_2$  optimization.

## **IV. H<sub>2</sub> Designs**

### **4.1 H<sub>2</sub>/LQG Regulator**

The objective of the optimal H<sub>2</sub> designs presented here is to develop a regulator that limits white noise feedthrough to the normal acceleration plant output ( $y_p$ ) and the control usage ( $u$ ). Regulation of initial conditions, such as in the  $\alpha$  state, is also desired. It is known that LQG is a special case of H<sub>2</sub> optimization, depending on weight locations and types. The basic LQG design uses static weights on both the control usage and states, and the basis here is to show trends by varying these two parameters. These quadratic weighting matrices can be seen in the LQG performance index

$$J = \int_0^{\infty} (\mathbf{x}^T \mathbf{Q} \mathbf{x} + u^T \mathbf{R} u) dt \quad (4.1)$$

where  $\mathbf{Q}$  is the state weighting (not to be confused with  $Q(s)$  from the JQ-type compensator parameterization) and  $\mathbf{R}$  the control weighting. Although in this design the control usage and states are weighted statically, the H<sub>2</sub> methodology has the potential of including frequency weights in the design model.

Furthermore, there are many popular LQG approaches (not discussed in this work) that examine choosing specific values of  $\mathbf{Q}$  and  $\mathbf{R}$ . The H<sub>2</sub> regulator design plant, showing the static weights on the control usage and states, is Figure 4-1. Since only one compensator is being designed in this

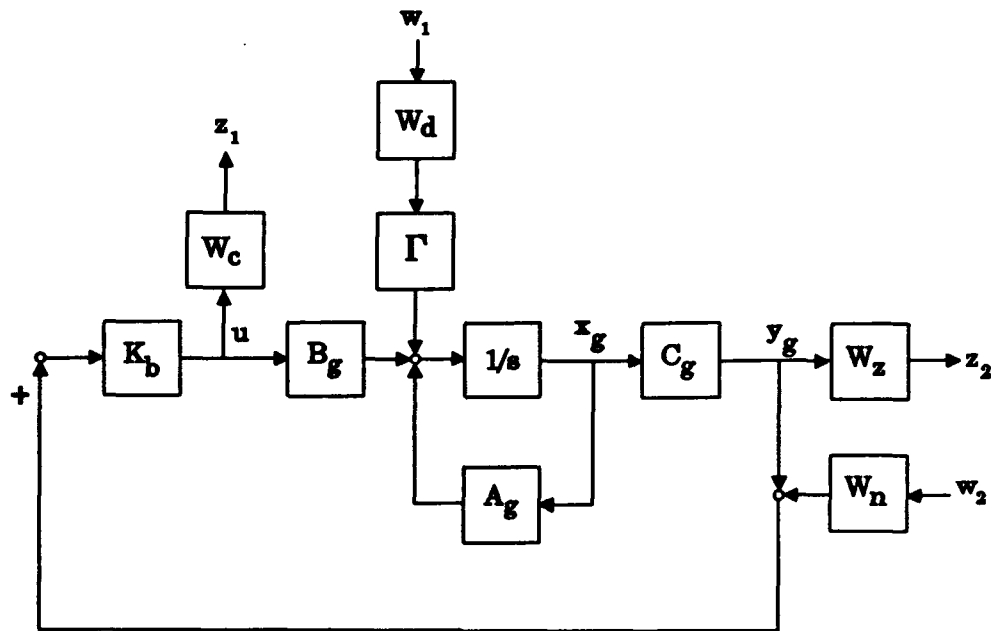


Figure 4-1.  $H_2$ /LQG Regulator Diagram

diagram, it will be a one degree-of-freedom (1 DOF) controller design. The weight on the states is  $W_z C_g$ , which actually means that the weight is on  $N_z$  since  $N_z = C_g x_g$ . If a particular design requires a weight to be placed directly on a state, all that is necessary is to move the location of  $W_z$  to the left of the  $C_g$  block in Figure 4-1. By moving the weighting block to this location, all the states plus the plant output could be weighted separately. The weight on control usage will be the scalar  $W_c$ .

Energy from the white noise inputs,  $w_1$  and  $w_2$ , will be minimized with respect to the chosen outputs,  $z_1$  and  $z_2$ , by the compensator design.

Figure 4-1 shows the state space matrices of the aircraft plant as  $A_g$ ,  $B_g$ , and

$C_r$ . These plant matrices represent the lower order model from the previous chapter; recall these include approximations for the second order short period, the first order servo, and the first order time delay. The wind disturbance for the design model uses the combination of  $W_d(s)$ ,  $\Gamma$ , and the input noise  $w_1$ . The white noise input  $w_2$  is added to the feedback signal as a measurement noise approximation. Notice this 1 DOF regulator problem has its compensator located on the right side of the summing junction in Figure 4-1. To examine tracking properties the feedback compensator has to be duplicated to match the 2 DOF simulation/transfer function model, Figure 3-4, that includes a feedforward compensator. Furthermore, since the  $H_2$  design of Figure 4-1 does not recognize the sign of a reference input that is zero, the feedforward compensator must be negated to get the proper output response.

For the closed-loop model, the transfer functions for the output of the plant and the control usage to all inputs are known. Repeated from Chapter III for a 1 DOF system, these are

$$\begin{aligned} y_g(s) &= -T(s)r + S(s)G_{Td}(s)w_1 + T(s)W_n w_2 \\ u(s) &= K_f(s)S(s)r + K_b(s)S(s)G_{Td}(s)w_1 + K_b(s)S(s)W_n w_2 \end{aligned} \quad (4.2)$$

In Equation (4.2) the output weightings  $W_c$  and  $W_z$  are removed since these are weighting functions for the performance index only. The noise inputs  $w_1$  and  $w_2$  are still included since they are in the simulation. Before the  $H_2$  optimization algorithm can be used, the design plant must be represented in



state space form. From Chapter II, the state space for the  $H_2$  design plant (denoted as  $P$ ) is

$$\dot{x} = Ax + B_w w + B_u u \quad (4.3a)$$

$$z = C_z x + D_{zw} w + D_{zu} u \quad (4.3b)$$

$$y = C_y x + D_{yw} w + D_{yu} u \quad (4.3c)$$

Using the  $H_2$  regulator diagram, Figure 4-1, the state space matrices in Equations (4.4) through (4.6) can be determined.

$$\begin{bmatrix} \dot{x}_s \\ \dot{x}_d \end{bmatrix} = \begin{bmatrix} A_s & \Gamma \\ 0 & A_d \end{bmatrix} \begin{bmatrix} x_s \\ x_d \end{bmatrix} + \begin{bmatrix} 0 & 0 \\ B_d & 0 \end{bmatrix} \begin{bmatrix} w_1 \\ w_2 \end{bmatrix} + \begin{bmatrix} B_s \\ 0 \end{bmatrix} [u] \quad (4.4)$$

$$\begin{bmatrix} z_1 \\ z_2 \end{bmatrix} = \begin{bmatrix} 0 & 0 \\ W_z C_s & 0 \end{bmatrix} \begin{bmatrix} x_s \\ x_d \end{bmatrix} + \begin{bmatrix} 0 & 0 \\ 0 & 0 \end{bmatrix} \begin{bmatrix} w_1 \\ w_2 \end{bmatrix} + \begin{bmatrix} W_c \\ 0 \end{bmatrix} [u] \quad (4.5)$$

$$[y] = [C_s \ 0] \begin{bmatrix} x_s \\ x_d \end{bmatrix} + [0 \ W_n] \begin{bmatrix} w_1 \\ w_2 \end{bmatrix} + [0][u] \quad (4.6)$$

This is the point where the  $H_2$  constraints discussed in Chapter II must be examined. The basic conditions that are checked here include  $D_{zw} = 0$ ,  $D_{yu} = 0$ ,  $D_{zu}^T D_{zu}$  full rank, and  $D_{yw} D_{yw}^T$  full rank. These will be met by the design with a nonzero  $W_n$  and  $W_c$ , so the design diagram is properly set up and the compensator development can continue.

### 4.1.1 $H_2$ /LOG Weight Selection

The design problem now centers on which signals to weight, and how to weight these signals. From the design diagram of Figure 4-1, the signals to weight (control usage and the plant output) have already been selected. Now consider how to choose these weights, keeping in mind that  $H_2$  optimization is minimizing the 2-norm of the transfer function matrix  $T_{zw}$ . As explained in the basic  $H_2$  diagram of Chapter II, this transfer function matrix will have white noise inputs ( $w$ ), and designer chosen outputs ( $z$ ).  $W_c$  and  $W_z$  are shown in the  $H_2$  regulator's  $T_{zw}$  as

$$T_{zw} = \begin{bmatrix} W_c K_b(s) S(s) G_{rd}(s) & W_c K_b(s) S(s) W_n \\ W_z S(s) G_{rd}(s) & W_z T(s) W_n \end{bmatrix} \quad (4.7)$$

An examination of Equation (4.7) should be used in conjunction with Equation (4.2) to determine choices of  $W_c$  and  $W_z$ . It is clear that as the dimensions of  $T_{zw}$  are increased, by adding more input white noises or outputs, it is easy to lose sight of the minimization process with respect to the individual transfer functions in  $T_{zw}$ . An important fact from Chapter II is that the 2-norm is an integral over all frequency, so looking at a logarithmic scale is deceiving since the integral is calculated on a linear scale. Recall that  $W_n$  and  $G_{rd}(s)$  are known fixed quantities in  $T_{zw}$ , with the magnitude plot of  $G_{rd}(s)$  appearing as Figure 3-5. It was shown that this transfer function is

predominantly low frequency, below 10 rad/sec, with a magnitude around 0.1 (-20 dB). In comparing this magnitude to that of the static  $W_n$  (0.025), it is evident that the  $G_{rd}(s)$  dc gain is about four times greater than  $W_n$ . Since  $W_n$  is supposedly an "all frequency" signal, it will be significant when integrating over all frequency. Looking again at  $T_{zw}$ , the left column that contains  $G_{rd}(s)$  will dominate the low frequency range. Similarly, the right column with  $W_n$  will dominate the high frequency range since  $G_{rd}(s)$  has rolled off. From the fact that both design weights are scalars, an iterative search of  $W_c$  and  $W_z$  will suffice. Now that the design background has been analyzed and the weight selection determined to be simple iterations, the weight selection results are investigated.

#### **4.1.2 $H_2$ /LOG Results**

Although cases of  $W_c = 0.01, 0.1, 1, 10, \text{ and } 100$  are examined, only the magnitude plots and time responses for the last three will be shown because of the complexity of graphics, and since the first two cases are unreasonable from a practical aspect. With small control usage weightings in these first two cases, the elevator deflections and subsequent responses are very fast and oscillatory. Margins for all five cases will be shown. Remember the object is to design a regulator that hopefully has good margins, since these are not guaranteed or designed in this setup. Even though  $W_z$  has not been mentioned, it is equally as important as  $W_c$ . As a matter of fact, it is exactly

the same as varying  $W_c$ . This can be seen by first looking at the conflict in the two parameters. If  $W_c$  and  $W_z$  are raised by equal ratios, the resulting controllers are identical. The only thing different would be the weighted value of the 2-norm of  $T_{zw}$ , and its value would go up by the exact same ratio each time. An example would be using  $W_c = 0.1$  and  $W_z = 1$ , then using  $W_c = 1$  and  $W_z = 10$ . Again the only difference in the two would be the 2-norm of  $T_{zw}$  being a value ten times higher in the second case. Thus, the value of  $W_z$  is held at one and  $W_c$  is varied. The values of  $W_c$  examined, weighted 2-norm of  $T_{zw}$ , and margin trends for these various  $W_c$  values are shown in Table 4-1.

Table 4-1.  $H_2$ /LQG Results ( $W_z=1$ ), LO

$W_c$	$\  T_{zw} \ _2$ Weighted	Bode Gain Margin (dB)	Bode Phase Margin (deg)	Complex Gain Margin (dB)	Complex Phase Margin (deg)
0.01	0.25	-7.7, 8.6	$\pm 78$	-7.7, 8.3	$\pm 36$
0.1	0.26	-7.6, 8.9	$\pm 79$	-7.6, 8.2	$\pm 36$
1.0	0.29	-6.4, 8.9	$\pm 83$	-6.4, 8.8	$\pm 37$
10.0	0.43	-3.3, 21	$\pm 34$	-3.3, 5.5	$\pm 27$
100.0	1.06	-1.5, 8.9	$\pm 14$	-1.5, 1.9	$\pm 11$

As noted in Table 4-1, the 2-norm of  $T_{zw}$  includes weights, and this can be used as a way to expose conflicting weights that may have been chosen.

Recall that Bode gain and phase margins are for a pure change in gain or phase, and the complex margins are based on the magnitude plots of sensitivity and complimentary sensitivity. It is obvious from Table 4-1 that the complex margins decrease as  $W_c$  rises from 1 to 100, and these margins are close from  $W_c = 0.01$  to 1. The case of  $W_c = 10$  is peculiar to this example with its increased Bode gain margin.

With concern for stability of the higher order model, closed-loop transfer function poles are also checked for each compensator. In examining the higher order system poles, each case reveals exactly one root just to the right of the origin. This unstable pole slowly migrates farther into the RHP as the value of  $W_c$  increases. For  $W_c = 1$  the unstable root is at 0.0595, and ends up at 0.1434 for  $W_c = 100$ . Remember that the unstable root is only occurring in the higher order transfer function model, not in the lower order model. From the  $H_2$  background in Chapter II, recall that the compensator will stabilize the lower order model. This unstable root will be noticeable in the upcoming higher order step response.

The analysis now shifts to  $T_{zw}$ , transfer function magnitudes, and time responses. It is known that the 2-norm of  $T_{zw}$  is being minimized with a stabilizing (not necessarily stable) compensator, and that this optimization is conducted through an integral over frequency. The key point here is that the integral is not based on a logarithmic scale. From  $T_{zw}$  (Equation 4.7), the bottom elements ( $W_z S(s) G_{rd}(s)$  and  $W_z T(s) W_u$ ) will dominate the minimization

when  $W_c$  is very small. The top two elements,  $W_c K_b(s) S(s) G_{rd}(s)$  and  $W_c K_b(s) S(s) W_n$ , will control the optimization process when  $W_c$  is large. The effect on these transfer functions will be seen in the magnitude plots. This again assumes  $W_z$  is held at one.

Transfer function magnitudes and simulation time responses for the three compensators are now examined. In all  $H_2$  regulator plots the solid line represents  $W_c = 1$ , the dashed line  $W_c = 10$ , and the dotted line  $W_c = 100$ . These are also noted on each plot. Use of the lower order model is given by LO, and the higher order model by HI.

Figure 4-2 shows the compensator magnitude decreasing as  $W_c$  is raised, which helps retard high frequency noise amplification by the compensator. The problem is that the compensator does not have as much freedom to cancel out the complex zero pair of the plant when  $W_c$  is at a high value. It is clear in the  $W_c = 1$  case that the compensator is starting to "notch out" the unwanted plant dynamics. From examining the two cases with lower values of  $W_c$  (not plotted), it was seen that the zero pair in the plant is nearly canceled by the compensator when the open loop transfer function is formed.

The open loop transfer function magnitude, or loop shape, is Figure 4-3. A desired high gain at low frequencies is definitely missing. Again, the canceling of unwanted plant dynamics is more apparent in the  $W_c = 1$  case, that does not follow the magnitude dip of the plant as much as the higher values of  $W_c$ . Even though the high frequency gain drops more as

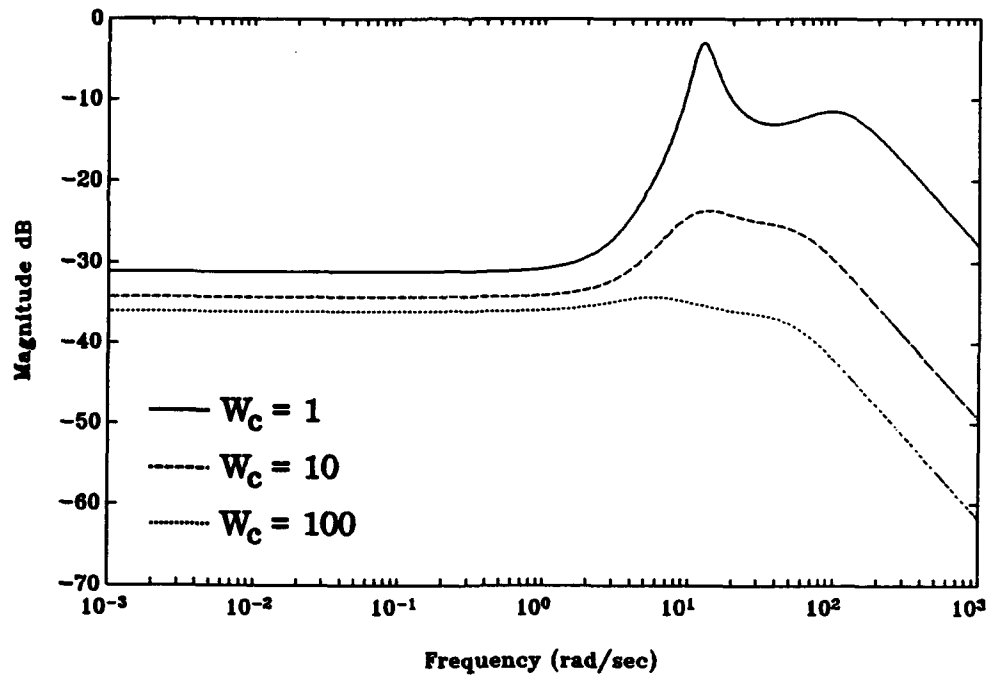


Figure 4-2. Compensator Magnitude

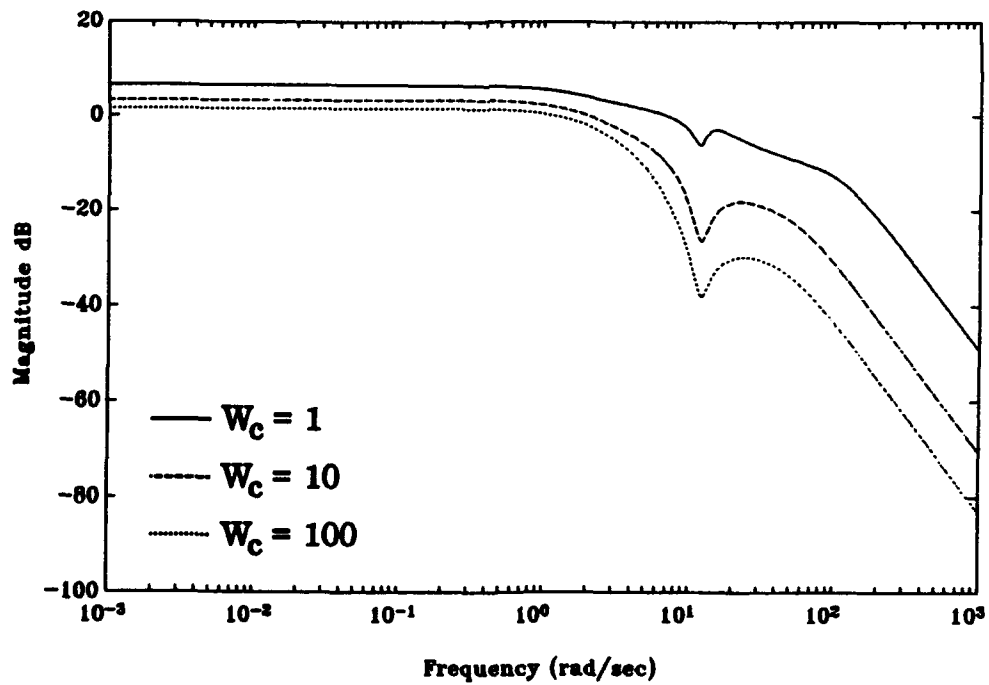


Figure 4-3. Magnitude of  $G(s)K_b(s)$ , LO

$W_c$  increases, the poor low frequency gain does not outweigh the benefit of a lower noise amplification at high frequencies.

The next frequency plot is the sensitivity transfer function magnitude, Figure 4-4. This shows that the low frequency wind disturbance will corrupt the  $W_c = 100$  case the most. The preferred shape would have a low gain at frequencies under around 10 rad/sec to attenuate the wind disturbance, based on the magnitude plot of  $G_{Td}(s)$ . The peak magnitude of each curve explains some of the trend of decreasing complex margins as  $W_c$  increases, although these margins also depend on the complimentary sensitivity magnitude plot. A sensitivity area tradeoff is also apparent between high and low frequencies.

An important term that appears in both  $T_{zw}$  and the control usage closed-loop transfer function is  $K_b(s)S(s)$ , plotted in Figure 4-5. From Equation (4.2), this gives an indication of the noise feedthrough to control usage.  $K_b(s)S(s)$  dominates the top row of  $T_{zw}$  since these elements are both the weighted control sensitivity. Hence, the drop in high frequency magnitude of  $K_b(s)S(s)$  as  $W_c$  is raised is caused by the integral dependence of the  $H_2$  methodology. For high loop gains, the highest is the  $W_c = 1$  case, the magnitude of  $K_b(s)S(s)$  is approaching the inverse of the plant magnitude (as explained in Chapter III). At low loop gains this magnitude follows the compensator gain shown previously. Furthermore, the inverse of the  $K_b(s)S(s)$  magnitude is the allowable plant additive uncertainty. The  $W_c = 1$  case exhibits the largest allowable additive uncertainty at low frequencies, and the



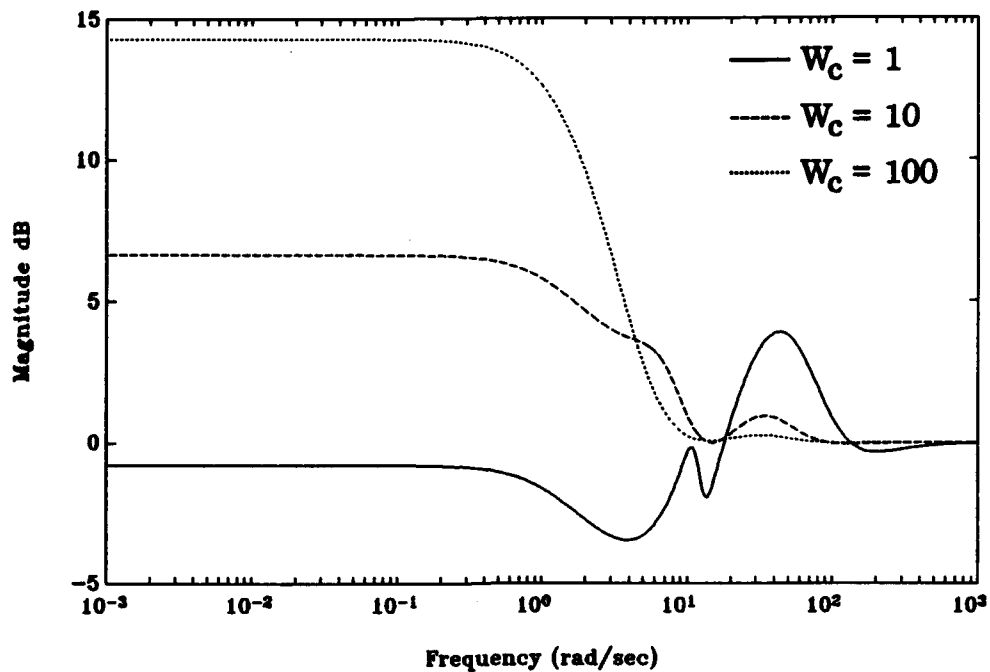


Figure 4-4. Sensitivity Magnitude, LO

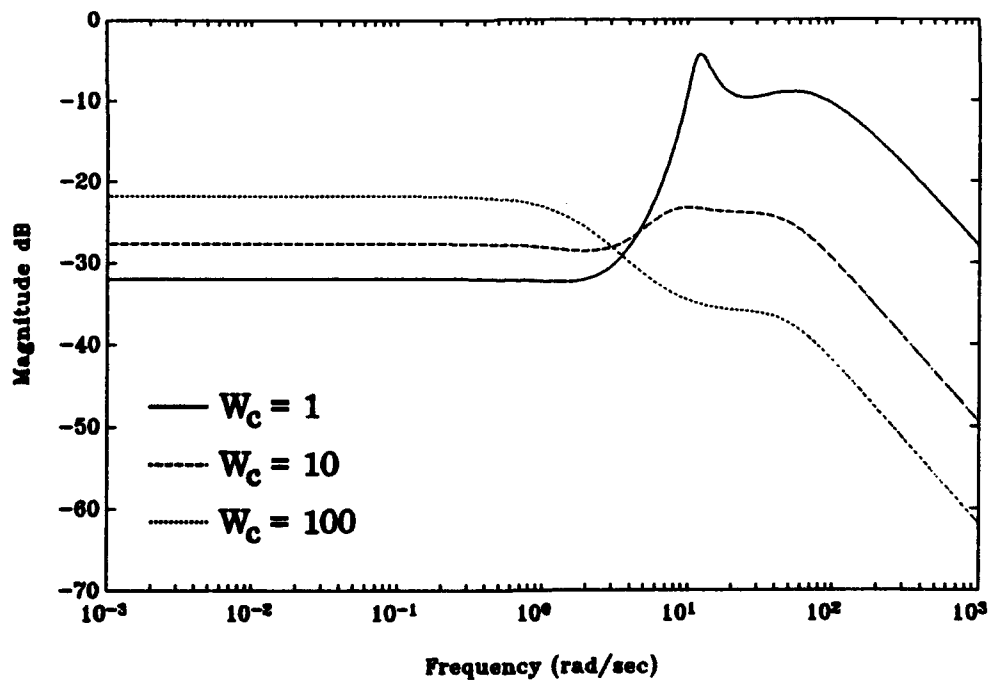


Figure 4-5. Magnitude of  $K_b(s)S(s)$ , LO

smallest amount at high frequencies.

The remaining magnitude plot is the complimentary sensitivity, Figure 4-6. This represents the measurement noise feedthrough to the plant output, the inverse of the allowable multiplicative uncertainty, and the closed-loop tracking transfer function. The measurement noise will be most evident in the  $W_c = 1$  case at high frequencies because of the larger gain. For the allowable multiplicative uncertainty, the  $W_c = 100$  case yields the most at high frequencies, and the least at low frequencies. It is evident that none of these three cases will give good tracking since the gain is above 0 dB at low frequencies and would still roll off too early even if the low frequency gain were adjusted in the simulation's feedforward compensator.

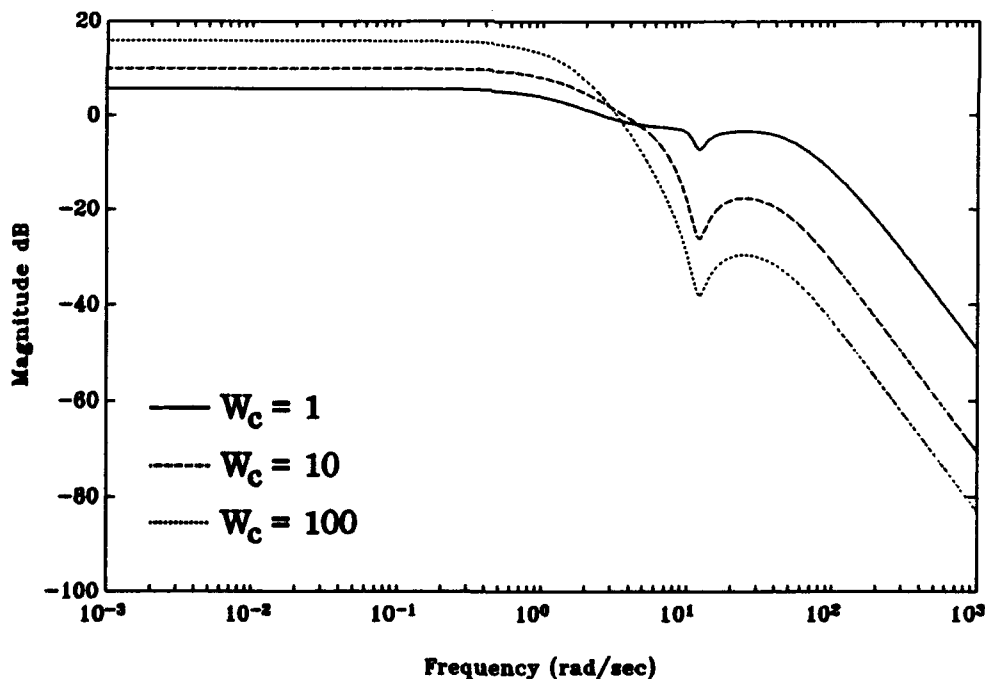


Figure 4-6. Complimentary Sensitivity Magnitude, LO

With the transfer function magnitudes covered, the focus now shifts to time responses. The first time response plot is the initial  $\alpha$  equal to 5 degrees simulation of Figure 4-7. It is not surprising that as the control weight increases from 1 to 100, the response goes from a fast oscillatory one with several overshoots to a slow highly damped one that takes close to 1.5 seconds to get near  $\alpha = 0$  degrees. Note that low frequency noises affect the  $W_c = 100$  case more, and a reason for this is that less control power is being allowed to correct the nonzero  $\alpha$ . Although this is not the plant output, the magnitude plots of  $S(s)$  and  $T(s)$  gave insight that low frequency noise would dominate the plant output for the  $W_c = 100$  case. These plots showed the least low frequency magnitude for noise corrupting the  $W_c = 1$  case.

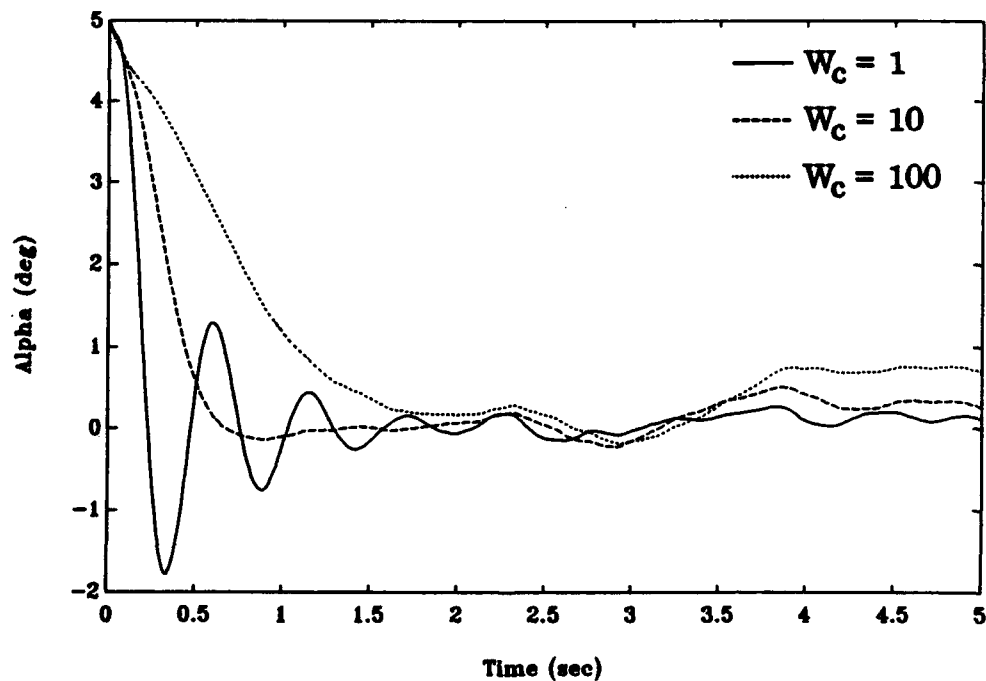


Figure 4-7.  $\alpha$  from  $\alpha(0) = 5$  deg, LO

Control usage appears in Figure 4-8 and confirms the analysis of the  $K_b(s)S(s)$  magnitude on the plant input. That magnitude plot, Figure 4-5, gives the direct feedthrough of the wind disturbance and measurement noise to control usage. The measurement noise in the  $W_c = 1$  time response is therefore from the high gain of  $K_b(s)S(s)$  at high frequency. Furthermore, on a smaller graph scale both low frequency noises were seen to corrupt the  $W_c = 100$  case, as Figure 4-5 foreshadowed. The elevator deflection was also checked and found to be within the 25 degree limit for the F-16. Note that control usage is the servo input, and elevator deflection the servo output.

Figure 4-9, the step responses for the lower order model, shows large steady state errors for all three cases. Although a step input is unrealistic for

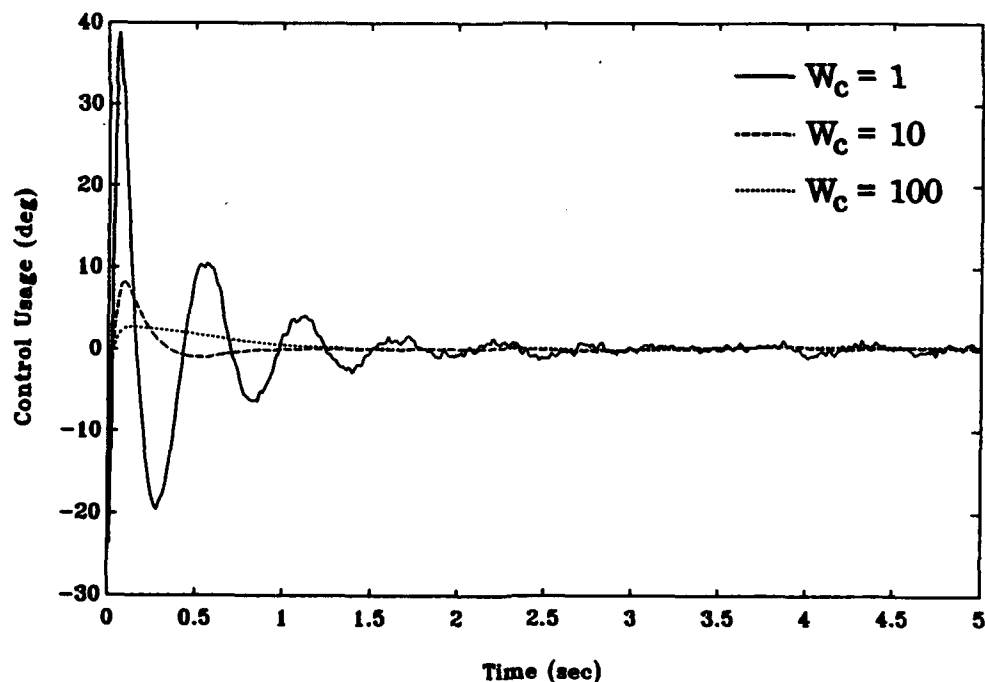


Figure 4-8. Control Usage ( $u$ ) from  $\alpha(0) = 5$  deg, LO

an  $N_z$  command, the resulting plot serves as a baseline for time response evaluations. The  $W_c = 100$  case is by far the worst, and shows the large low frequency noise effects that depend on  $S(s)$  and  $T(s)$ . Higher frequency noise is evident in the  $W_c = 1$  case, and it has the least steady state error. Recall that tracking is not specified as a requirement for this design, and since no weight is specifically used to help tracking the design process ignores this.

The higher order step response is Figure 4-10. This is included to show the unstable higher order system explained earlier. As seen in the  $W_c = 100$  case, with the RHP pole farther from the origin than the other two cases, the unstable root causes a rapid departure of  $N_z$ . Since the unstable root is very close to the origin, it does not show up in the ten second simulation for the

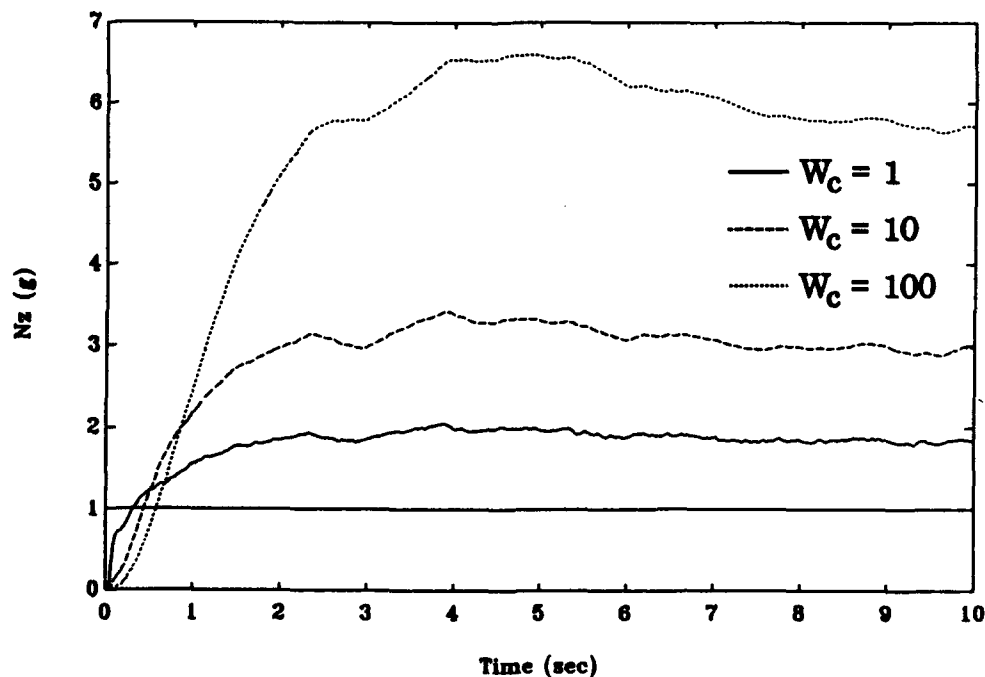


Figure 4-9.  $N_z$  from  $N_z$  Command Step, LO

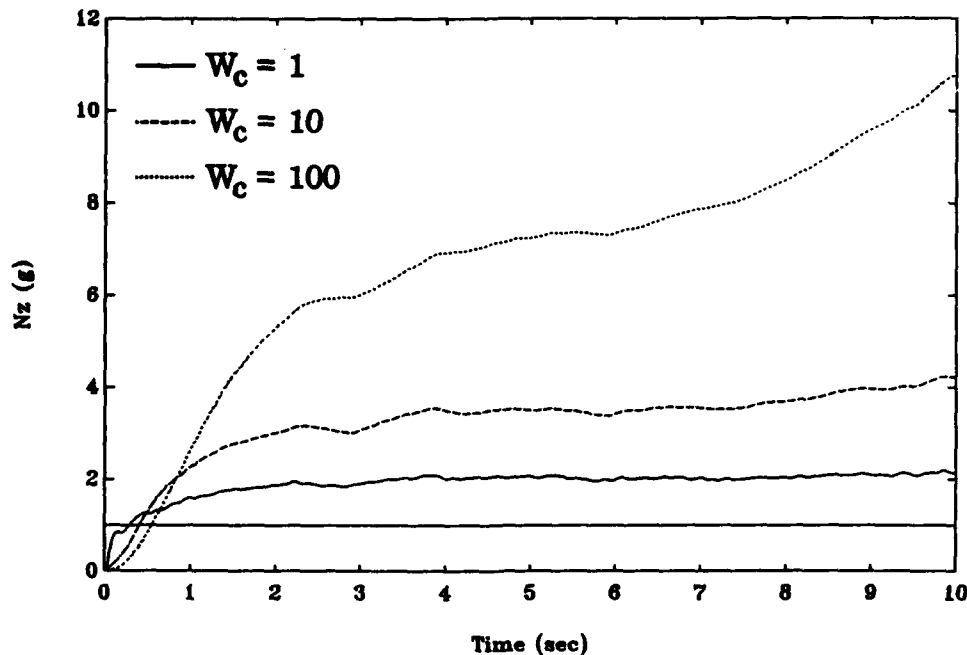


Figure 4-10.  $N_z$  from  $N_z$  Command Step, HI

$W_c = 1$  case, and is barely evident in the  $W_c = 10$  case. The remaining higher order time responses are similar to the lower order ones, therefore they are not shown.

The conclusions from this design can be summarized in the following:

- i). A good  $\alpha$  regulator can be successfully designed for this plant, although gain and phase margins must be watched since LQG does not guarantee them. The best regulator for the initial  $\alpha$  condition is the  $W_c = 10$  case, since the  $W_c = 1$  case had large oscillations and the  $W_c = 100$  case is fairly slow.
- ii). The unstable higher order pole near the origin slowly migrates to the right, on the real axis, as  $W_c$  rises. This caused the step response departure

in the higher order plot, that is most evident with the  $W_c = 100$  case (recall a zero order hold is the time delay in the HI model).

iii). Any form of useful tracking seems to have been a failure, but is not asked for in the design diagram.

iv). As  $W_c$  rises, more low frequency noise will corrupt the plant output and control usage, and less high frequency measurement noise will affect both. This is a direct result of the transfer function magnitudes, that are again weighted statically. Specifically the low frequency magnitudes of  $S(s)$ ,  $T(s)$ , and  $K_b(s)S(s)$  all rise as  $W_c$  increases. The high frequency magnitudes of  $S(s)$ ,  $T(s)$ , and  $K_b(s)S(s)$  all decrease as  $W_c$  increases.

v). The compensator cancels the plant's complex zero pair better with the lowest control weighting ( $W_c = 1$ ), which also gives the highest compensator magnitude at all frequencies when compared to the other  $W_c$  cases.

vi). The open-loop transfer function magnitude (loop shape) decreases as  $W_c$  increases, and to a much larger extent at high frequencies.

vii). The complex gain and phase margins decrease substantially as  $W_c$  rises from 1 to 100.

With these in mind, the issue approached is the case of the higher order transfer function model being unstable, and the transfer function magnitudes ( $S(s)$ ,  $T(s)$ , and  $K_b(s)S(s)$ ) not being shaped to both reduce noise levels and give some form of closed-loop tracking. This leads to the following section on  $H_2$  sensitivity.

## **4.2 $H_2$ /LQG Sensitivity**

The purpose of this section is to improve on the instability of the higher order closed-loop model from the previous LQG design, with the overall objective being to robustly design a stabilizing  $H_2$  compensator by use of a weighting on sensitivity. It was also apparent that the basic LQG design exhibited poor tracking, but the tracking problem will not be directly addressed in this section. Although the goal here is to stabilize the higher order transfer function model, the key is to not lose the good regulation properties of the basic LQG design in the process. This approach of trying to stabilize the higher order model will depend solely on increasing the complex margins of the lower order system. By adding a dynamic sensitivity weighting to the  $H_2$ /LQG design, it is possible to affect the sensitivity transfer function so that complex margins may be improved. Not only can these complex margins be altered, but also the wind disturbance that reaches the plant output can be significantly reduced.

The sensitivity weighting is included in the design model as shown in Figure 4-11. This weight,  $W_s(s)$ , is a transfer function which introduces the first frequency dependent weight to the  $H_2$  design process. By placing this frequency weight on  $S(s)$ , disturbances entering at the plant output can be minimized since the low frequency gain of  $S(s)$  can now be lowered. The



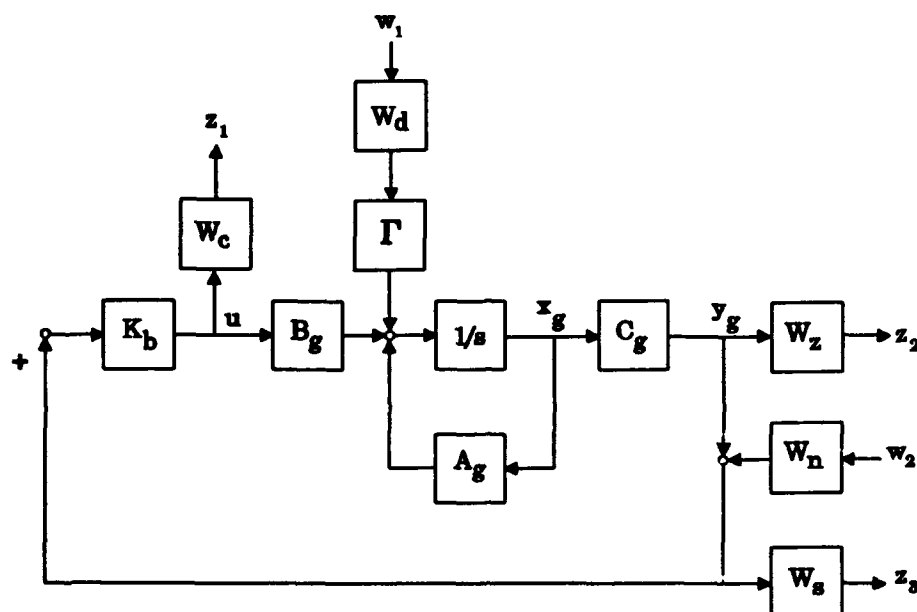


Figure 4-11.  $H_2$ /LQG Sensitivity Diagram

closed-loop transfer functions are repeated below to emphasize the significance of  $S(s)$  on the low frequency wind disturbance that reaches the plant output, from the white noise  $w_1$ .

$$\begin{aligned} y_g(s) &= -T(s)r + S(s)G_{Td}(s)w_1 + T(s)W_n w_2 \\ u(s) &= K_f(s)S(s)r + K_b(s)S(s)G_{Td}(s)w_1 + K_b(s)S(s)W_n w_2 \end{aligned} \quad (4.8)$$

The magnitude of  $G_{Td}(s)$ , plotted in Chapter III, is again a low-pass filter with energy mainly below 10 rad/sec.

The  $H_2$  design diagram, Figure 4-11, is expressed in the required matrix form of the design plant state space by Equations (4.9) through (4.11).

$$\begin{bmatrix} \dot{x}_g \\ \dot{x}_d \\ \dot{x}_s \end{bmatrix} = \begin{bmatrix} A_g & \Gamma & 0 \\ 0 & A_d & 0 \\ B_s C_g & 0 & A_s \end{bmatrix} \begin{bmatrix} x_g \\ x_d \\ x_s \end{bmatrix} + \begin{bmatrix} 0 & 0 \\ B_d & 0 \\ 0 & B_s W_n \end{bmatrix} \begin{bmatrix} w_1 \\ w_2 \end{bmatrix} + \begin{bmatrix} B_g \\ 0 \\ 0 \end{bmatrix} [u] \quad (4.9)$$

$$\begin{bmatrix} z_1 \\ z_2 \\ z_3 \end{bmatrix} = \begin{bmatrix} 0 & 0 & 0 \\ W_s C_g & 0 & 0 \\ D_s C_g & 0 & C_s \end{bmatrix} \begin{bmatrix} x_g \\ x_d \\ x_s \end{bmatrix} + \begin{bmatrix} 0 & 0 \\ 0 & 0 \\ 0 & D_s W_n \end{bmatrix} \begin{bmatrix} w_1 \\ w_2 \end{bmatrix} + \begin{bmatrix} W_c \\ 0 \\ 0 \end{bmatrix} [u] \quad (4.10)$$

$$[y] = \begin{bmatrix} C_g & 0 & 0 \end{bmatrix} \begin{bmatrix} x_g \\ x_d \\ x_s \end{bmatrix} + \begin{bmatrix} 0 & W_n \end{bmatrix} \begin{bmatrix} w_1 \\ w_2 \end{bmatrix} + [0][u] \quad (4.11)$$

Again the first things to check are the basic  $H_2$  constraints on  $D_{zw}$ ,  $D_{yu}$ ,  $D_{zu}$ , and  $D_{yw}$ . As long as the scalars  $W_c$  and  $W_n$  are nonzero, the matrices of  $D_{zu}^T D_{zu}$  and  $D_{yw} D_{yw}^T$  are full rank. It is evident that  $D_{yu} = 0$  is satisfied, but requiring  $D_{zw} = 0$  directly limits  $D_s$  (the "D" term of the sensitivity weight's state space) to be zero, since  $W_n$  cannot be zero from the previous constraints. This means that  $W_s(s)$  must be strictly proper, i.e. the  $W_s(s)$  magnitude must roll off at least 20 dB/decade. If  $W_s(s)$  were to have a nonzero "D" term, the optimization problem would be ill-posed. From a physical standpoint, a nonzero "D" term in  $W_s(s)$  would give a direct path of the infinite energy white noise to the performance index.

### 4.2.1 H<sub>2</sub>/LQG Sensitivity Weight Selection

Knowing that  $W_s(s)$  must have at least a 20 dB/decade roll off, the question of exactly what  $W_s(s)$  should look like is now examined. Since the weight is chosen to represent the inverse of the desired sensitivity transfer function magnitude, a low-pass filter is needed. This low-pass filter will add only one state to the optimal H<sub>2</sub> compensator. Examining  $T_{zw}$ , Equation (4.12), it is seen that  $W_s(s)$  directly weights  $S(s)$  in the bottom row.

$$T_{zw} = \begin{bmatrix} W_c K_b(s) S(s) G_{rd}(s) & W_c K_b(s) S(s) W_n \\ W_z S(s) G_{rd}(s) & W_z T(s) W_n \\ W_s(s) S(s) G_{rd}(s) & W_s(s) S(s) W_n \end{bmatrix} \quad (4.12)$$

After the 2-norm of  $T_{zw}$  is minimized to a certain value, it is known that the 2-norm of each individual transfer function inside  $T_{zw}$  can be at most equal to the overall 2-norm of  $T_{zw}$ . From this, think of  $S(s)$  as being the inverse of  $W_s(s)$  so that the resulting 2-norms of  $T_{zw}$ 's bottom elements are at most equal to the 2-norm of  $T_{zw}$ . However, this does not work in reverse order. It is not true that if each individual transfer function's 2-norm is less than some value, then the 2-norm of  $T_{zw}$  will be that value. To create a basis for judging the individual transfer function elements of  $T_{zw}$ , recall that several of the components in these elements are known. Known values in  $T_{zw}$  are  $W_n = 0.025$ ,  $W_z = 1$ ,  $W_c$  (a chosen scalar), the magnitude of  $G_{rd}(s)$ , and the

design weighting  $W_s(s)$ . When  $W_s(s)$  has very high gain at low frequencies, it is seen from  $T_{zw}$  that the bottom row will impact the low frequency range in the 2-norm calculation. It is also known that  $S(s)$  must eventually go to 0 dB at high frequency since the lower order model rolls off, as in most physical systems. By choosing  $W_s(s)$  as the inverse of  $S(s)$ , the  $H_2$  design methodology should return a compensator that gives a sensitivity function shaped like that which is desired at low frequency, although this goes back to the integral's dependence on frequency in the 2-norm calculation. The high frequency area will be dominated by the right column of  $T_{zw}$  (from  $W_n$ ). Even when  $W_s(s)$  has large magnitude at low frequencies, the 2-norm of  $T_{zw}$  will not be controlled at high frequency by the  $T_{zw}(3,2)$  element because  $W_s(s)$  has to roll off there. When the overall magnitude of  $W_s(s)$  is small, the sensitivity weighting is nullified and the design returns to the previous LQG type; only this time there are unnecessary compensator states because of the weight being a transfer function.

A first order sensitivity weighting transfer function, the low-pass filter, is given by [Ino90] as

$$W_s(s) = \frac{(\omega_x)}{(s + \epsilon)} \quad (4.13)$$

In Equation (4.13),  $\omega_x$  is a measure of the desired  $W_s(s)$  0 dB crossover frequency, and  $\epsilon$  is a positive number ( $\epsilon \ll 1$ ) chosen so that the pole is not a

pure integrator. A pure integrator would serve to complicate the process by possibly introducing an undetectable pole. Hence, the value of  $\epsilon$  will be set to 0.01 in all subsequent work.

As explained in Chapter III, to increase the complex margins that depend on  $S(s)$ , the maximum magnitude of  $S(s)$  must be minimized. Since this plant typically yields two peaks for  $|S(j\omega)|$ , the focus is to try and equalize these peak magnitudes by weighting the one at lower frequency. This is accomplished by altering the dc gain of  $W_s(s)$ , or equivalently the  $\omega_x$  value in Equation (4.13). The results of changing  $\omega_x$  and  $W_c$  in this  $H_2$  design are now analyzed.

#### **4.2.2 $H_2$ /LOG Sensitivity Results**

A total of six cases are examined, with three values of  $\omega_x$  and two values for  $W_c$ . The values of  $\omega_x$  tested include 1, 10, and 100. With  $W_z = 1$  for all cases, the different values of  $\omega_x$  are investigated for  $W_c = 1$  and  $W_c = 10$ . Table 4-2 shows the values for the weighted 2-norm of  $T_{zw}$  and the margins in each of these six cases. The boldface row in Table 4-2 represents the only case out of the six that produces all stable poles for the higher order transfer function model. Of interest is that the stable case shows a much larger complex phase margin. In a comparison to Table 4-1 for the same value of  $W_c = 1$  (using  $\omega_x = 10$ ), it is seen that the complex phase margin is around 10 degrees higher, but the complex gain margins have decreased. Other

cases, specifically the ( $W_c = 10$ ,  $\omega_x = 1$ ) combination, give better complex margins over the "best regulator" from the LQG section.

Table 4-2.  $H_2$ /LQG Sensitivity Results ( $W_z=1$ ), LO

$\omega_x$	$W_c$	$\ T_{zw}\ _2$ Weighted	Bode Gain Margin (dB)	Bode Phase Margin (deg)	Complex Gain Margin (dB)	Complex Phase Margin (deg)
1	1	0.306	-9.0, 8.7	$\pm 74$	-8.6, 8.3	$\pm 37$
10	1	0.438	-17.5, 6.1	$\pm 47$	-13, 5.7	$\pm 46$
100	1	1.56	-26.1, 3.0	$\pm 25$	-4.0, 2.9	$\pm 21$
1	10	0.486	-4.8, 18.4	$\pm 34$	-4.4, 7.5	$\pm 34$
10	10	0.961	-9.9, 11.7	$\pm 37$	-7.9, 7.1	$\pm 35$
100	10	3.11	-19.4, 4.7	$\pm 35$	-7.1, 4.3	$\pm 33$

The concentration now turns to four of these six cases to further evaluate. Since the  $W_c = 10$  value gives desired LQG regulation properties, this is combined with  $\omega_x$  values of 1, 10, and 100. Of importance is that the higher order transfer function model is unstable in each of these three cases. The fourth case will be the stable one, ( $W_c = 1$ ,  $\omega_x = 10$ ). The first look is at the unstable poles for the  $W_c = 10$  cases. Varying  $\omega_x$  from 1 to 100 does not cause the unstable pole to migrate slowly into the RHP like the LQG design displayed, but this is not the same type of parameter change as with  $W_c$  (see the top and bottom rows of  $T_{zw}$ , Equation (4.12)). In the LQG design the

control weighting ( $W_c$ ) was varied, whereas now the control weight is held constant and the sensitivity weight crossover (at 0 dB) is varied. The ( $W_c = 10$ ,  $\omega_x = 1$ ) case is examined in greater detail since it will turn out to be the best regulator in the time response evaluations. The pole closest to the origin in this case is located at 0.009, whereas in the LQG design this pole was at a 0.093 value. Therefore, adding the sensitivity weighting has moved this unstable root of the higher order transfer function model closer to the origin, and given better complex margins for this particular example. The stable case has its closest pole to the origin at -0.0004; almost in the RHP, but stable.

In the following evaluation of these four cases, all plots will have the three cases of constant  $W_c = 10$  ( $\omega_x = 1$ , 10, and 100) denoted by  $\omega_x = 1$  as the solid line,  $\omega_x = 10$  as the dashed line, and  $\omega_x = 100$  as the dotted line. The stable ( $W_c = 1$ ,  $\omega_x = 10$ ) case is shown as the dot-dash curve. The trends of the three unstable cases will be the concentration, since at least two of these will be practical from a regulation aspect.

The first magnitude plot, Figure 4-12, is the compensator. The overall shapes of these magnitudes are very similar. As  $\omega_x$  increases by the factor of ten, the compensator magnitude shifts up 12 to 15 dB in each of the  $W_c = 10$  cases. The only difference shows up around 10 rad/sec where the plant complex zero pair is being cancelled out better as  $\omega_x$  rises. The stable case appears very close to the  $\omega_x = 100$  one. The closeness of these cases goes

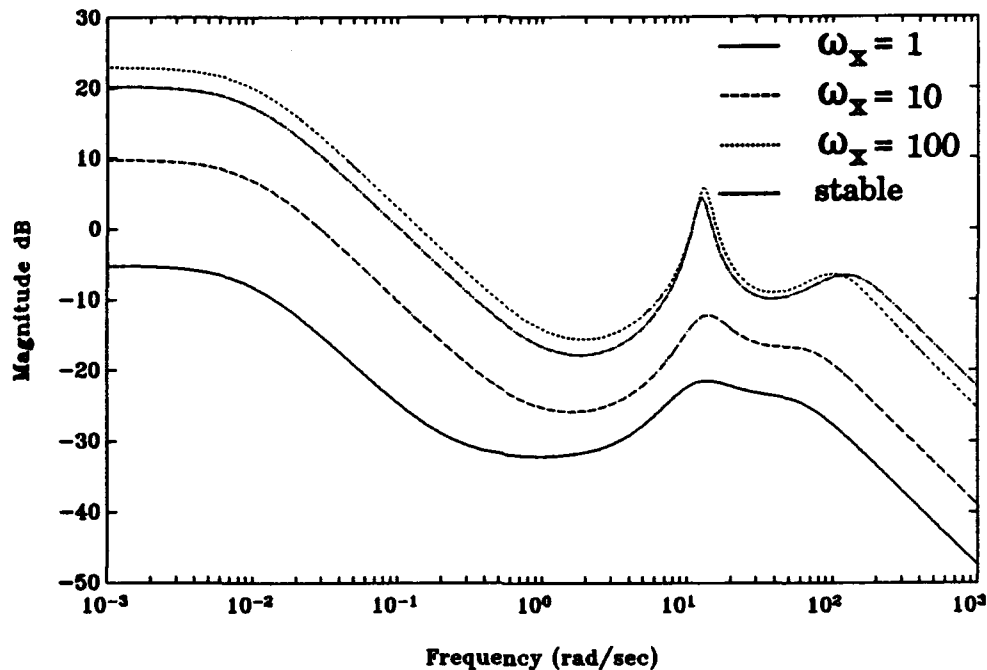


Figure 4-12. Compensator Magnitude

back to what was seen in the basic LQG design with the ratio of  $W_c$  versus  $W_x$ . In this likeness, the same factor of ten ratio is used on both  $W_c$  and  $\omega_x$ , but the difference here is that there is an extra row in  $T_{zw}$  (second row) that causes the ratio in sensitivity to not produce the exact same compensator. An example would be using ( $W_c = 1$ ,  $\omega_x = 10$ ) versus ( $W_c = 10$ ,  $\omega_x = 100$ ). As the values of  $W_c$  and  $\omega_x$  increase, the second row of  $T_{zw}$  becomes less important to the 2-norm calculation. This is assuming the static value of  $W_z$  remains at one. Therefore, it is this second row of  $T_{zw}$  that keeps the ( $W_c = 1$ ,  $\omega_x = 10$ ) and ( $W_c = 10$ ,  $\omega_x = 100$ ) compensators close in magnitude, but not exactly the same.



The loop shape is presented in Figure 4-13. This looks more like the classic loop shape that is desired since there is high gain at low frequency, and a preferred roll off at 100 rad/sec. The trend is generally consistent as  $\omega_x$  is raised, although the higher  $\omega_x$  value shows the unwanted plant dynamics being countered better. The stable case appears to notch out the complex plant zero pair the best.

The magnitude plots of the sensitivity transfer function that are shaped by  $W_s(s)$  appear in Figure 4-14. Although the general shape follows the inverse of  $W_s(s)$  at low frequency, the starting value at  $10^{-3}$  rad/sec is different for these cases (not a 20 dB spread like  $W_s(s)$  had). This can be attributed to the relative unimportance of the 2-norm over the low frequency range and

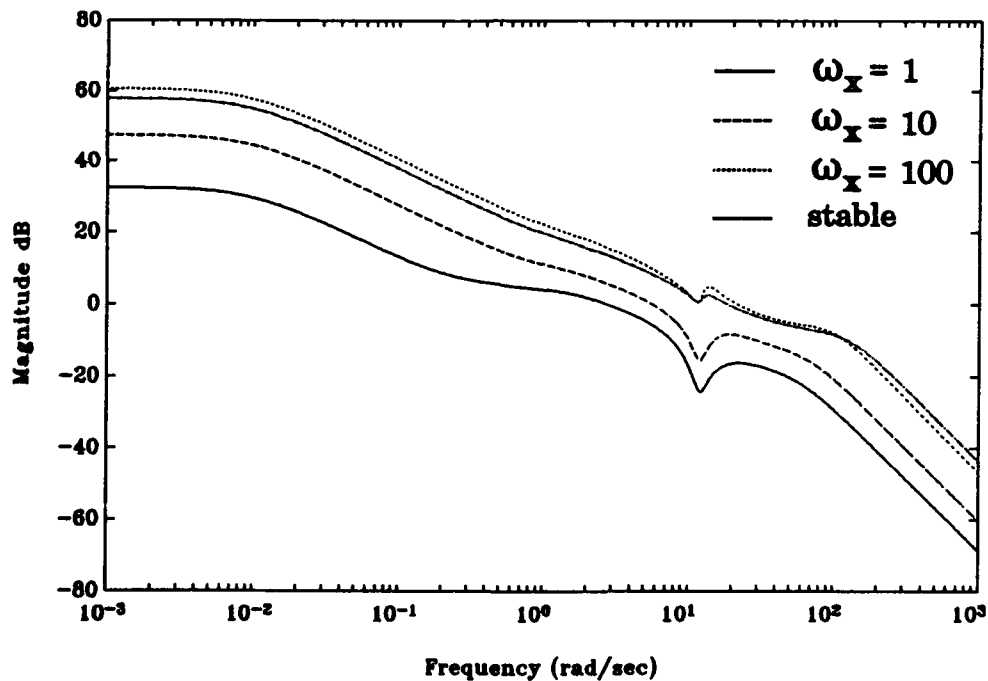


Figure 4-13. Magnitude of  $G(s)K(s)$ , LO

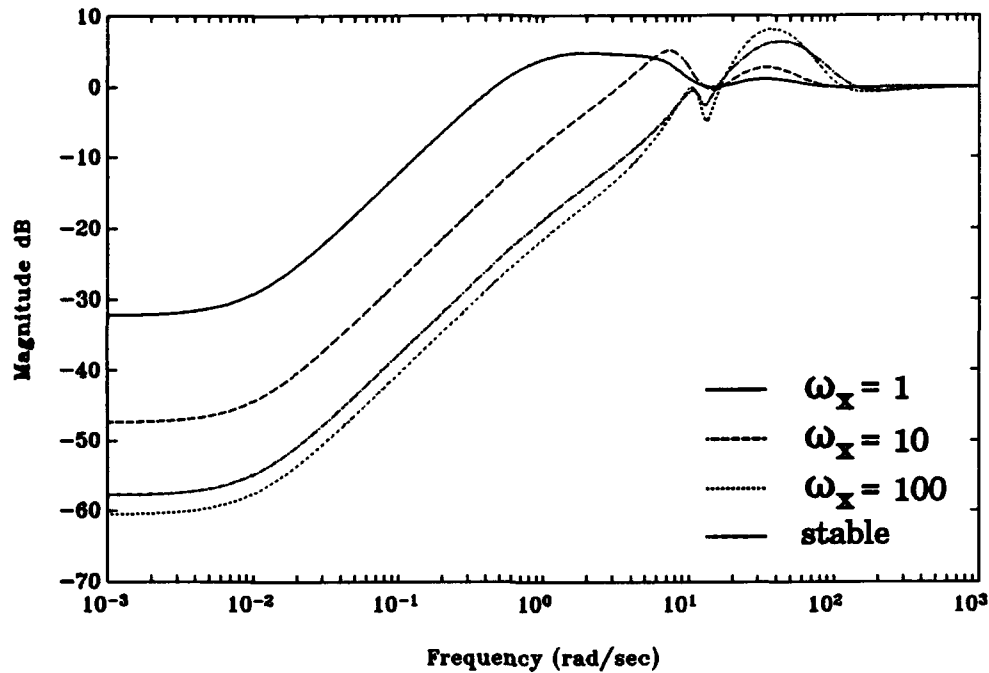


Figure 4-14. Sensitivity Magnitude, LO

the many other elements in  $T_{zw}$  that include  $S(s)$ . The peaks in the  $S(s)$  magnitudes are seen to shift as  $\omega_x$  rises (the highest of the two also increases), which is the cause of the decreasing upper complex gain margin. The shape of  $S(s)$  looks very good at low frequencies in comparison to the pure LQG designs. This small gain at low frequencies will directly cause a decrease in the amount of wind disturbance that corrupts the plant output. Furthermore, the sensitivity area rule and "waterbed effect" are evident in Figure 4-14.

The magnitude of  $T(s)$  appears in Figure 4-15. Several results of this plot stand out immediately. To begin with, the  $\omega_x = 1$  case is clearly a poor tracker because of the peak centered at 1 rad/sec and the early roll off.

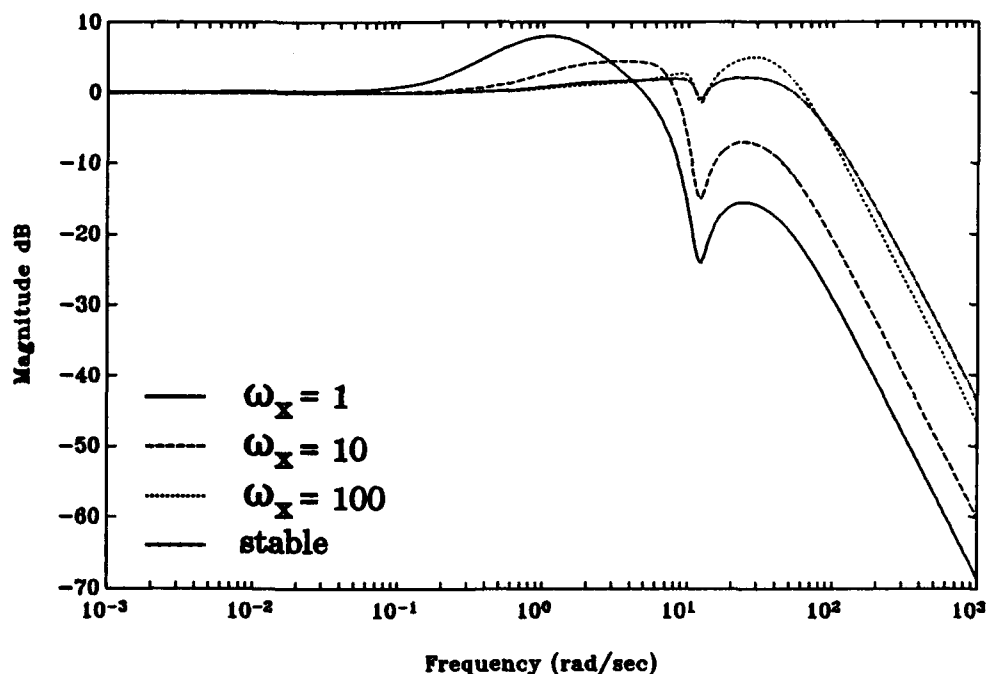


Figure 4-15. Complimentary Sensitivity Magnitude, LO

The higher peak of this curve will lower the complex margins that depend on  $T(s)$  more than the other three cases. The low frequency gain of 0 dB for  $T(s)$  shows that any low frequency measurement noise will directly feed through to the plant output, although it is not amplified like the LQG design was (except above 0.1 rad/sec). The trend in  $T(s)$  is that increasing  $\omega_x$  will cause more high frequency measurement noise to corrupt  $y_e(s)$  since the high frequency gain is increasing with  $\omega_x$ . The best case for complex margins that depend on  $T(s)$  is by far the stable one. The  $\omega_x = 1$  case does have the largest allowable multiplicative uncertainty at high frequencies, whereas the stable and  $\omega_x = 100$  cases show the least.

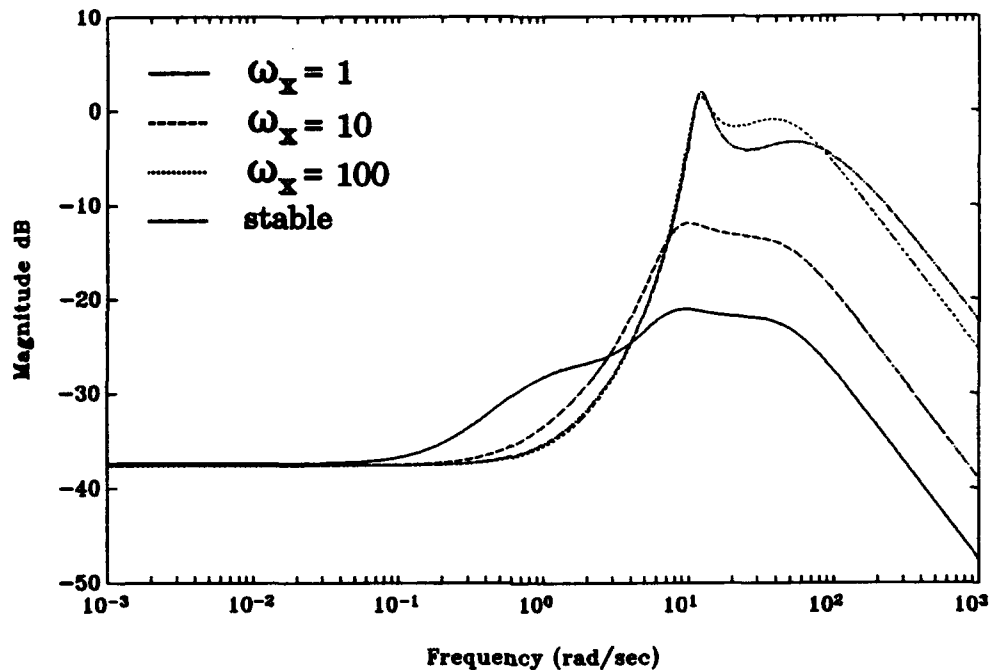


Figure 4-16. Magnitude of  $K_b(s)S(s)$ , LO

The magnitude of  $K_b(s)S(s)$  is shown in Figure 4-16, and is again tied to noise corruption of the control usage. The trend definitely shows that as  $\omega_x$  increases, more high frequency measurement noise passes to the control usage. All low frequency noises will be attenuated very well since the loop shape has large enough gain at low frequencies to drive the magnitude of  $K_b(s)S(s)$  to the inverse of the plant magnitude. A predictable trend is shown by this plot as  $\omega_x$  varies, and again the  $\omega_x = 100$  case is very close to the stable one. Note that the  $\omega_x = 100$  and the stable cases yield the least allowable plant additive uncertainty, yet the most high frequency noise corruption of control usage. This is a direct result of the changing compensator magnitude.

Figure 4-17 is the  $\alpha$  initial condition response for the lower order system. The  $\omega_x = 1$  case is clearly the best of the four that are shown, but it does exhibit the largest amount of low frequency noise corruption. Both the stable case and the  $\omega_x = 100$  case again are similar, and undesirable. These last two cases are very fast and oscillatory, although they do not exhibit large amounts of noise corruption.

Control usage for the  $\alpha(0) = 5$  degrees initial condition is Figure 4-18. This clearly demonstrates that high deflections and fast rates will be evident in the elevator. Remember that this is the servo input, not the elevator deflection. Recall that Figure 4-16, the magnitude of  $K_b(s)S(s)$ , indicates

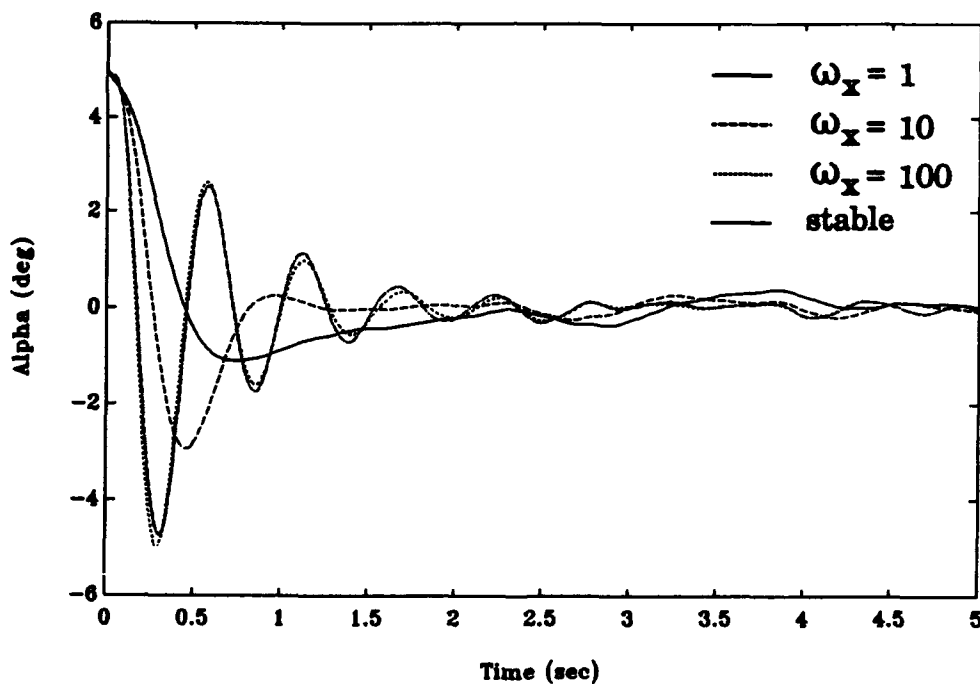


Figure 4-17.  $\alpha$  from  $\alpha(0) = 5$  deg, LO

that high frequency measurement noise will corrupt this response more as  $\omega_x$  rises. This is evident in the control response for the  $\omega_x = 100$  and stable cases, both of which also oscillate much longer than the other two cases.

The time response for the  $N_z$  step command is Figure 4-19.

As expected from the magnitude plot of  $T(s)$  in Figure 4-15, the  $\omega_x = 1$  case shows a very large overshoot. Recall that this  $\omega_x = 1$  case is the best regulator though. Also, low frequency noise corrupts the  $\omega_x = 1$  case the most, and is a result of the higher magnitudes of  $S(s)$  and  $T(s)$  at low frequencies. High frequency noise corrupts the best two trackers the most ( $\omega_x = 100$  and the stable case), and again is based on the same magnitudes

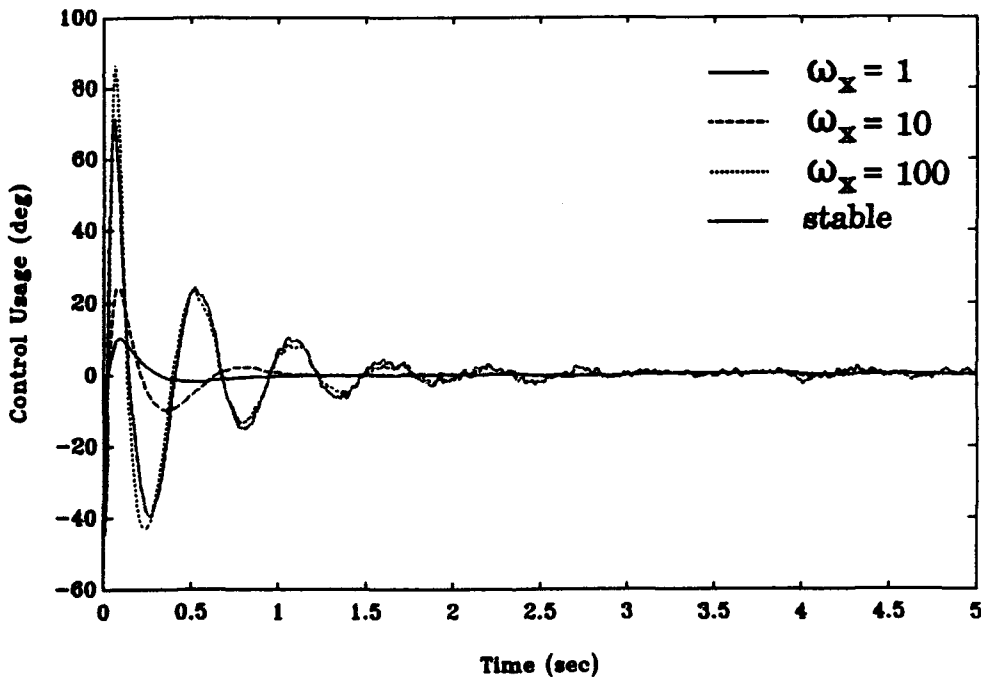


Figure 4-18. Control Usage ( $u$ ) from  $\alpha(0) = 5$  deg, LO

of  $S(s)$  and  $T(s)$ . Thus, not only is there a change in tracking as  $\omega_x$  varies, but there also is a tradeoff in the frequency range of the corrupting noise. Another feature of Figure 4-19 is that the step responses track the 1 G command value well, unlike the previous LQG design.

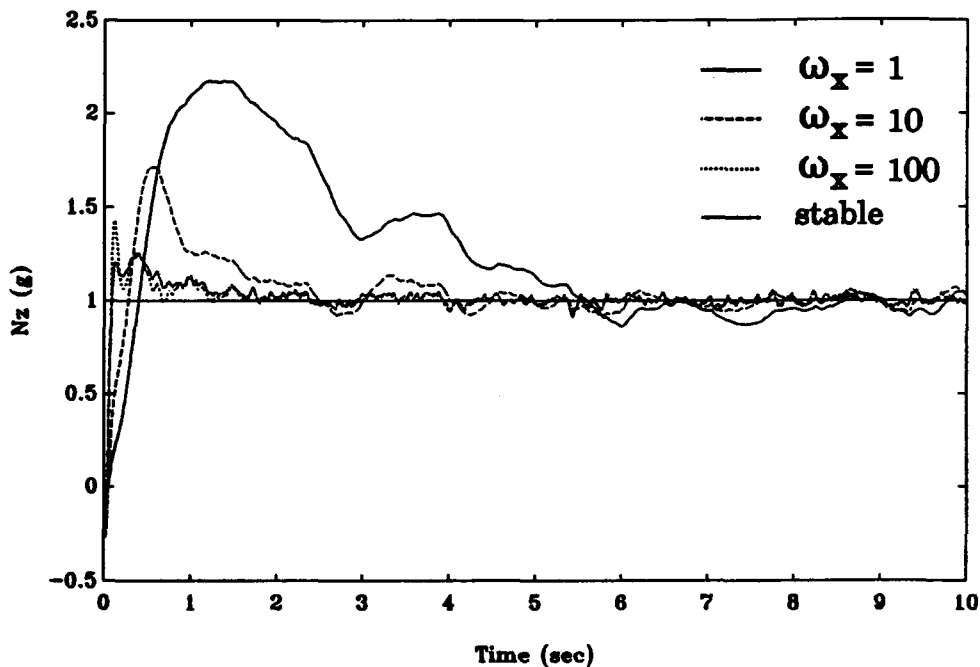


Figure 4-19.  $N_z$  from  $N_z$  Command Step, LO

Higher order responses are not shown since they were similar to the lower order ones. The unstable pole was not seen in the ten second step response because of its larger time constant.

The evaluation results of this design can be concluded in the following:

- i). The goal of stabilizing the higher order model has been achieved with the  $(W_e = 1, \omega_x = 10)$  case, which gives a poor regulator, but a good tracker.

ii). The complex margins are increased over the basic LQG design's "best regulator", in comparison to the ( $W_c = 10$ ,  $\omega_x = 1$ ) case, which still exhibits poor tracking. Although it is unstable, the RHP pole in this case is almost at the origin (+0.009), which is closer than the basic LQG design (+0.093).

iii). The steady state error for a step input to the lower order model is very small, whereas the previous LQG step response never returned near 1 G.

iv). Sensitivity was shaped as desired, directly reducing the wind disturbance feedthrough to the plant output and indirectly provided tracking performance. By asking for improved sensitivity at low frequencies, good tracking in some cases has been given.

v). As  $\omega_x$  was increased, the compensator magnitude rose at all frequencies and canceled the plant's complex zero pair better. Likewise, the magnitude of the loop shape also rose at all frequencies for increasing  $\omega_x$ .

vi). The high frequency magnitudes of  $T(s)$  and  $K_b(s)S(s)$  both increased as  $\omega_x$  was raised, which resulted in sensor noise passing to the plant output and control usage to a greater extent.

vii). The complex margins did not follow a pattern as  $\omega_x$  was varied, but only three values of  $\omega_x$  were examined.

viii). The unstable pole near the origin, for the five unstable cases in Table 4-2, did not follow a migration pattern like the LQG unstable root did.

With these in mind, a 2 DOF system will be examined next to see if further tracking improvements can be directly achieved.



### **4.3 H<sub>2</sub>/LQG Tracking**

The purpose of this section is to demonstrate a 2 DOF H<sub>2</sub> controller in the tracking role. Stability of the higher order transfer function model is again a desire. Weighting constraints will be continued on the control usage and the plant output as in previous designs. As a review of the H<sub>2</sub> design using the sensitivity weight, satisfactory inner loop regulation and higher order system stability is achievable. A problem with this method is in the case of tracking an input command. In the 1 DOF designs from Sections 4.1 and 4.2, the closed-loop transfer function from  $r(s)$  to  $y_g(s)$  is  $-T(s)$ , and from this came the problems associated with poor tracking performance for the good regulators. Having this significant limit on performance is somewhat circumvented in the 2 DOF controller design covered in this section.

The H<sub>2</sub> tracking diagram used to design this 2 DOF compensator is shown in Figure 4-20. A tracking weight is added to the previous design, and the sensitivity weight is removed. The error between the plant output and the command input  $w_3$  is weighted by  $W_t(s)$ . This tracking weight,  $W_t(s)$ , is a low-pass filter designed to allow the minimization of the low frequency error for an input  $r(s)$  to the plant output  $y_g(s)$  in the simulation model. Raising the low frequency gain of  $W_t(s)$  allows the tracking weight to dominate in the crucial low frequency range, therefore giving a compensator that tracks low

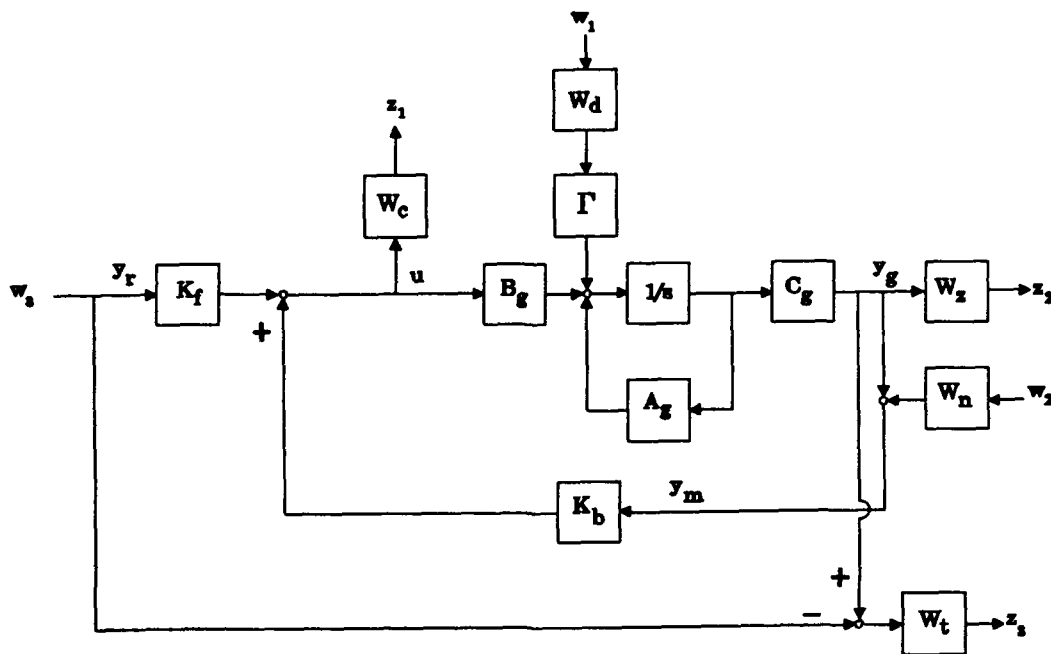


Figure 4-20.  $H_2/LQG$  Tracking Diagram

frequency input commands. The feedback controller  $K_b(s)$  is the compensator that determines closed-loop stability and regulation. Although the 2 DOF setup appears to be the straightforward solution with the feedback compensator controlling stability/regulation properties, and the feedforward compensator providing the desired tracking, remember that in this 2 DOF design the compensators are constrained to share the same poles.

The closed-loop transfer functions for the 1 DOF and 2 DOF controllers are obviously different with respect to the input signal  $r(s)$  (represented by  $w_3$  in Figure 4-20). These closed-loop transfer functions are repeated in Equation (4.14) to stress the relationship between  $r(s)$  and  $y_g(s)$ , which is  $S(s)G(s)K_f(s)$ . In the previous designs this transfer function is the negated

complimentary sensitivity,  $-T(s)$ , and using the magnitude of  $T(s)$  is a severe handicap for tracking (in the cases examined thus far).

$$\begin{aligned} y_g(s) &= S(s)G(s)K_f(s)r(s) + S(s)G_{rd}(s)w_1 + T(s)W_n w_2 \\ u(s) &= K_f(s)S(s)r(s) + K_b(s)S(s)G_{rd}(s)w_1 + K_b(s)S(s)W_n w_2 \end{aligned} \quad (4.14)$$

It is now necessary to set up the 2 DOF design in the required  $H_2$  form. From the design diagram, Figure 4-20, the state space representation for the  $H_2$  design plant is

$$\begin{bmatrix} \dot{x}_g \\ \dot{x}_d \\ \dot{x}_t \end{bmatrix} = \begin{bmatrix} A_g & \Gamma & 0 \\ 0 & A_d & 0 \\ B_t C_g & 0 & A_t \end{bmatrix} \begin{bmatrix} x_g \\ x_d \\ x_t \end{bmatrix} + \begin{bmatrix} 0 & 0 & 0 \\ B_d & 0 & 0 \\ 0 & 0 & -B_t \end{bmatrix} \begin{bmatrix} w_1 \\ w_2 \\ w_3 \end{bmatrix} + \begin{bmatrix} B_g \\ 0 \\ 0 \end{bmatrix} [u] \quad (4.15)$$

$$\begin{bmatrix} z_1 \\ z_2 \\ z_3 \end{bmatrix} = \begin{bmatrix} 0 & 0 & 0 \\ W_r C_g & 0 & 0 \\ D_t C_g & 0 & C_t \end{bmatrix} \begin{bmatrix} x_g \\ x_d \\ x_t \end{bmatrix} + \begin{bmatrix} 0 & 0 & 0 \\ 0 & 0 & 0 \\ 0 & 0 & -D_t \end{bmatrix} \begin{bmatrix} w_1 \\ w_2 \\ w_3 \end{bmatrix} + \begin{bmatrix} W_c \\ 0 \\ 0 \end{bmatrix} [u] \quad (4.16)$$

$$\begin{bmatrix} y_r \\ y_m \end{bmatrix} = \begin{bmatrix} 0 & 0 & 0 \\ C_g & 0 & 0 \end{bmatrix} \begin{bmatrix} x_g \\ x_d \\ x_t \end{bmatrix} + \begin{bmatrix} 0 & 0 & 1 \\ 0 & W_n & 0 \end{bmatrix} \begin{bmatrix} w_1 \\ w_2 \\ w_3 \end{bmatrix} + \begin{bmatrix} 0 \\ 0 \end{bmatrix} [u] \quad (4.17)$$

The most noticeable difference from the previous forms is in the 2 DOF it is necessary to have two  $y$ 's in Equation (4.17). This is from the fact that

$u(s) = K(s)y(s)$  in the developmental theory, and therefore yields

$$[u] = [K_f \ K_b] \begin{bmatrix} y_f \\ y_m \end{bmatrix} \quad (4.18)$$

The actual compensator returned by the  $H_2$  algorithm is  $K = [K_f \ K_b]$ , which is given in state space form. The "B" matrix of this state space is then broken up to give the state space of each individual compensator. The "D" matrix is not of much concern since it will be zero. Having the common "A" matrix in each compensator's state space again emphasizes the fact that the poles of each compensator are the same. Checking the four basic  $H_2$  constraints on  $D_{zw}$ ,  $D_{yu}$ ,  $D_{zu}$ , and  $D_{yw}$ , it is seen that values of  $W_c$  and  $W_n$  cannot be zero, but  $D_t$  has to be zero. This directly says that  $W_t(s)$  must roll off at least 20 dB/dec. With the buildup now shown, some results of choosing various  $W_t(s)$  shapes are examined.

#### **4.3.1 $H_2$ /LOG Tracking Weight Selection**

$W_t(s)$  is the only frequency weight in the tracking design, but this is not solely to achieve simplicity. Over 100 cases of choosing different frequency weights for sensitivity, and for a weighting in the feedforward path that will be referred to as  $W_r(s)$ , were examined for this section. Also, two locations were tested for  $W_r(s)$ ; one before  $w_3$  is fed forward for tracking error and one after. The basic design results of including only  $W_t(s)$ , leaving  $W_r(s)$  and

$W_r(s)$  out, are very close to the results with these extra weights left in. Not only did the cases come very close, but by including only the tracking error weight the resulting controller size is smaller. The advantage of designing a smaller compensator outweighs any visible increase in performance from adding the extra weights, and some of the increased performance for the larger systems could be a result of just the larger compensator (since  $K_f(s)$  and  $K_b(s)$  share poles). Thus, it may be possible to add poles to the  $W_t(s)$  transfer function, making it the same order as when  $W_r(s)$  and  $W_s(s)$  were tested, and get a slight increase in performance. The performance differences were considered trivial in this design. This should not be meant to deter the use of  $W_r(s)$  or  $W_s(s)$  for another example, but with this plant and the numerous combinations explored, it turned out to be undesirable.

$W_s(s)$  may be a possible "over" constraint, as seen in  $T_{zw}$  for Figure 4-20, given by

$$T_{zw} = \begin{bmatrix} W_c K_b(s) S(s) G_{rd}(s) & W_c K_b(s) S(s) W_n & W_c K_f(s) S(s) \\ W_z S(s) G_{rd}(s) & W_z T(s) W_n & W_z S(s) G(s) K_f(s) \\ W_t(s) S(s) G_{rd}(s) & W_t(s) T(s) W_n & W_t(s) (S(s) G(s) K_f(s) - 1) \end{bmatrix} \quad (4.19)$$

and by comparison of Figures 4-20 and 4-11. The  $T_{zw}(3,1)$  transfer function is a direct constraint on  $S(s)$ , just as it appears in the previous section. Using  $W_t(s)$  is not needed to shape  $S(s)$  for good tracking as in the 1 DOF designs, but it is possible to shape  $S(s)$  at low frequency through the tracking weight.

Although this is an added benefit of the tracking design, the real importance is in the (3,3) element of  $T_{zw}$ . Recalling that the 2-norm is in a sense trying to minimize each individual transfer function over all frequency, it is seen that the transfer function weighted by  $W_t(s)$  in  $T_{zw}(3,3)$  is  $S(s)G(s)K_f(s)-1$ . It is the closed-loop transfer function from  $r(s)$  to  $y_g(s)$ ,  $S(s)G(s)K_f(s)$ , that is the design target. Thus, the transfer function to focus on minimizing is  $S(s)G(s)K_f(s)-1$ . This is exactly what is desired, i.e. magnitude of  $S(s)G(s)K_f(s) = 1$  at low frequencies. Making  $W_t(s)$  very large where tracking is desired should give this, but remember the two other transfer function constraints from  $W_t(s)$  (the (3,1) and (3,2) elements of  $T_{zw}$ ).

#### **4.3.2 $H_2$ /LOG Tracking Results**

The controller investigation begins by choosing the  $W_t(s)$  transfer function. As a baseline, consider a low-pass filter with a dc gain of 50 dB, and a single pole located at  $s = -0.1$ . This is the second row of Table 4-3, whereas the other cases in Table 4-3 are slight variations to this transfer function weight. The first and third rows represent a 10 dB shift of the original 50 dB dc gain, and the last two rows show the constant 50 dB dc gain with the pole moved left and right by a factor of ten. The two boldface rows are stabilizing controllers for the higher order transfer function model. Notice, as in the sensitivity design, these stabilizing controllers yield larger complex phase margins compared to the remaining cases. These two also

show some of the largest complex gain margins in the table. The trend as the dc gain of  $W_i(s)$  is raised, with a fixed  $W_i(s)$  pole, shows increasing complex phase and lower gain margins. The upper complex gain margins, as well as the complex margins for the  $W_i(s)$  pole being shifted with a constant dc gain, do not reveal any patterns.

Table 4-3.  $H_2/LQG$  Tracking Results ( $W_z=1, W_c=20$ ), LO

$W_i(s)$ dc gain (dB)	$W_i(s)$ pole	$\ T_{zw}\ _2$ Weighted	Bode Gain Margin (dB)	Bode Phase Margin (deg)	Complex Gain Margin (dB)	Complex Phase Margin (deg)
40	0.1	6.2	-8.0, 15	$\pm 32$	-6.3, 6.0	$\pm 30$
50	0.1	15.8	-11.2, 10	$\pm 36$	-8.1, 7.1	$\pm 35$
60	0.1	39.6	-15.1, 6.2	$\pm 44$	-9.7, 5.7	$\pm 39$
50	0.01	2.7	-5.3, 16	$\pm 27$	-4.5, 5.4	$\pm 27$
50	1	95.9	-26, 4.1	$\pm 31$	-5.9, 3.8	$\pm 29$

The analysis will now focus on magnitude and time response plots. Only the runs with the constant pole are shown in plots, but the other two are briefly explained at the end of the section. The three cases shown in the plots will have a solid line for the 40 dB dc gain of  $W_i(s)$ , a dashed line for the 50 dB dc gain case, and a dotted line for the 60 dB dc gain case.

The magnitude of the feedforward compensator, which is critical to tracking performance, is plotted in Figure 4-21. This plot gives rise to some interesting facts about the closed-loop transfer function from  $r(s)$  to  $y_e(s)$ . It is evident that as the dc gain of  $W_f(s)$  rises, the low frequency gain of  $K_f(s)$  falls; this low frequency gain also shifts to the right. The insight here is that the higher gain choice of 60 dB will likely give better tracking for higher frequency inputs because of this gain shift to the right. Of course, the closed-loop tracking transfer function also depends on  $S(s)$  and  $G(s)$  directly. Notice that the high frequency magnitude, which increases as the dc gain of  $W_f(s)$  rises, will pass through increasing amounts of high frequency noises that enter with the input command.

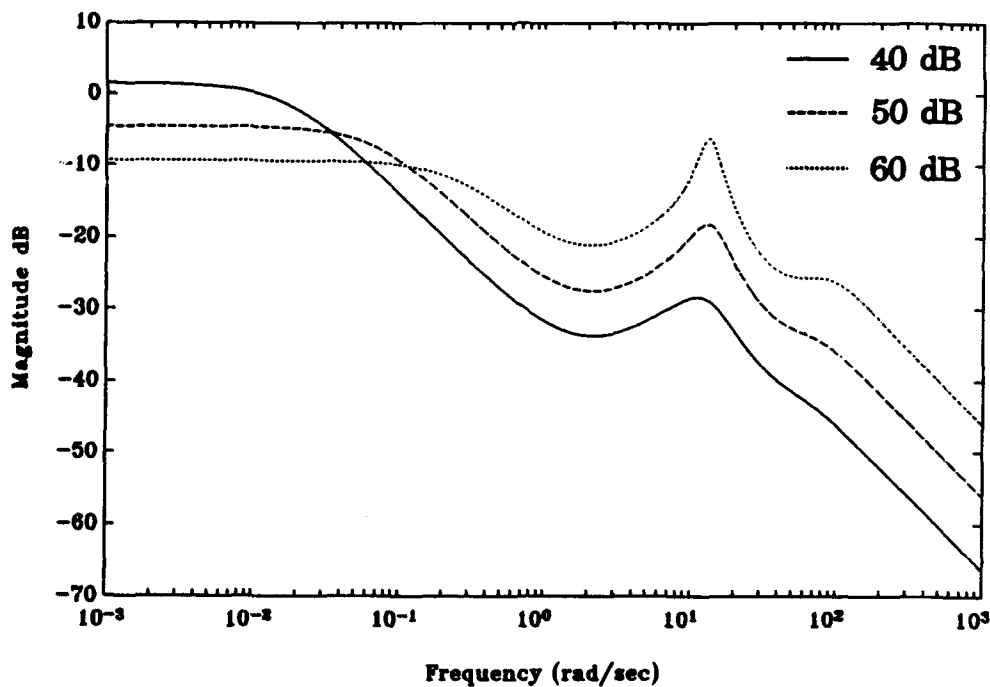


Figure 4-21. Feedforward Compensator Magnitude



The feedback compensator magnitude, shown in Figure 4-22, basically follows the same trend as the feedforward one (again they both share the same poles). More importantly, this magnitude plot resembles those in the sensitivity section, and this compensator determines loop performance such as stability and regulation. The increased magnitude at high frequencies shows that amplification of high frequency noises will take place to a larger extent as the gain of  $W_c(s)$  rises. The notching out of the complex plant zero is slightly more evident in the feedback compensator cases, especially with the dc gain case of 60 dB.

The loop shape is shown in Figure 4-23. The tradeoffs are apparent in the gains at high and low frequencies, and in the crossover frequency. High

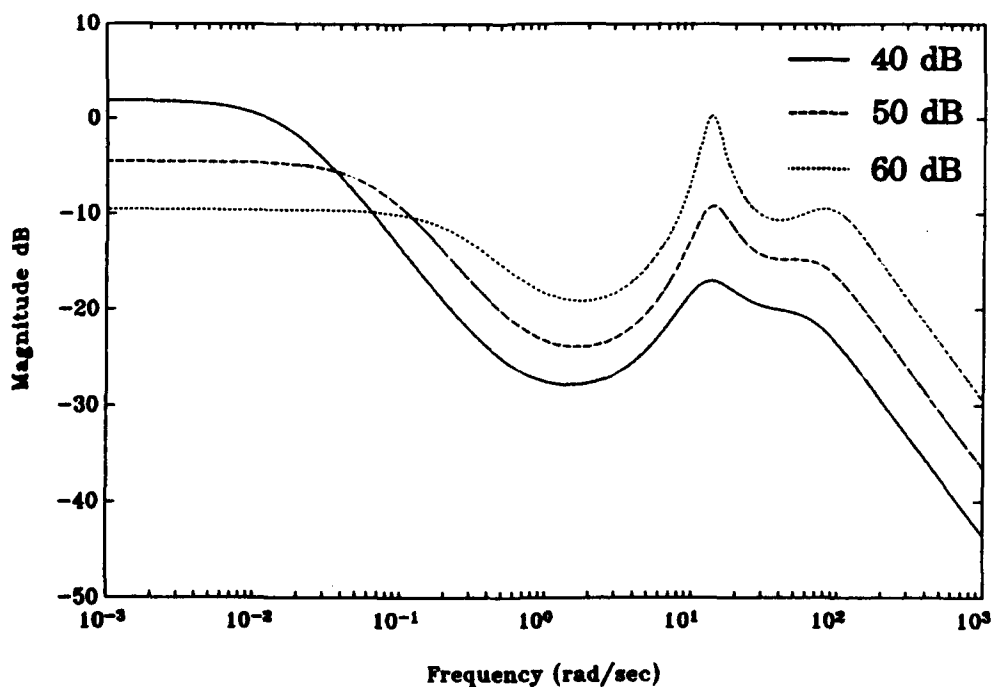


Figure 4-22. Feedback Compensator Magnitude

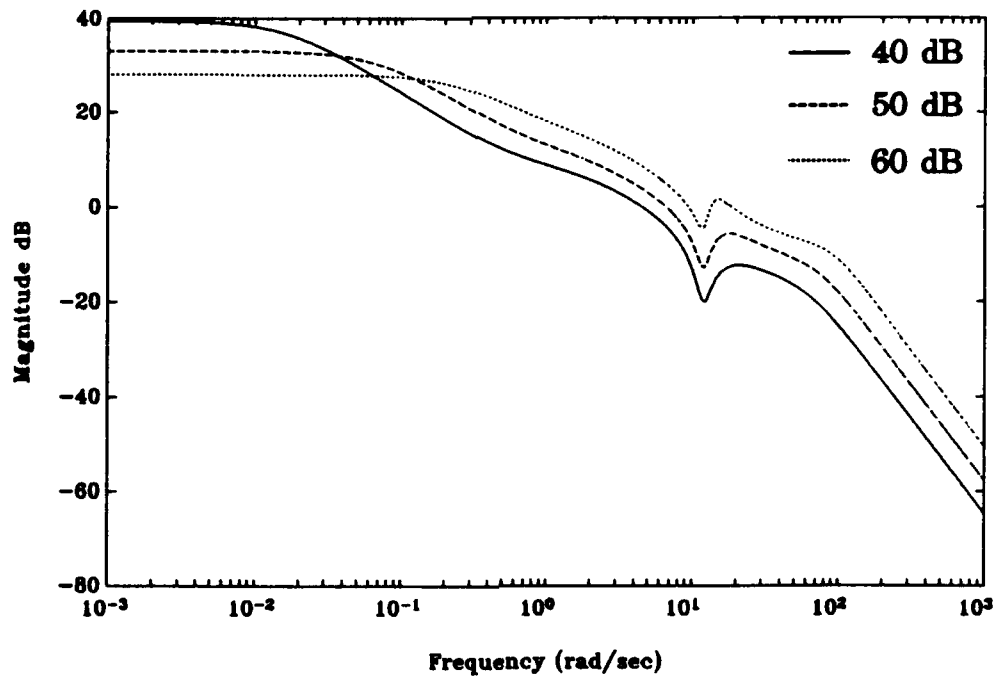


Figure 4-23. Magnitude of  $G(s)K_b(s)$ , LO

gain at low frequency is desired from a classical sense, but with a 2 DOF controller this is not necessarily the same. In the 1 DOF design the loop shape magnitude at low frequencies needs to be very high so that  $S(s)$  will be low there, and in turn having a small magnitude of  $S(s)$  at low frequencies gives a  $T(s)$  magnitude near unity (or 0 dB). This  $T(s)$  magnitude near one at low frequencies gives the 1 DOF tracking performance. In the 2 DOF design  $S(s)$  still affects the disturbances the same way, but now the tracking dependence on  $T(s)$  is changed. The 40 dB case has the highest magnitude at low frequencies and the lowest magnitude at high frequencies, but does not cancel the plant's complex zero pair as well.

Figure 4-24 is the magnitude of the sensitivity transfer function for the

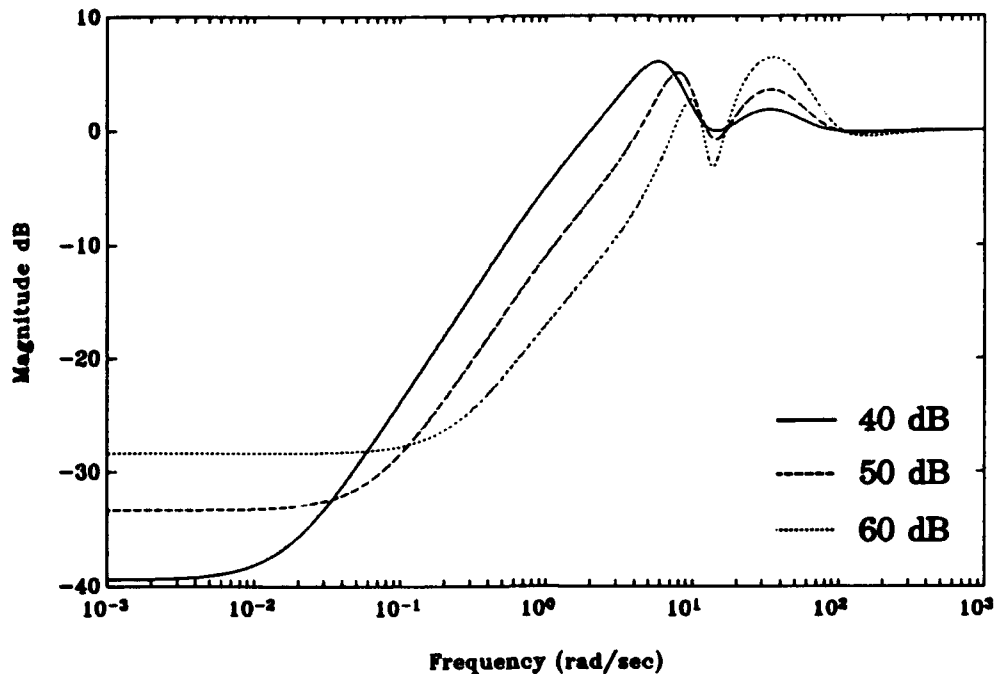


Figure 4-24. Sensitivity Magnitude, LO

lower order model. The overall shape is similar to the results from the sensitivity section, and seeing that  $S(s)$  also depends on  $W_t(s)$  in  $T_{zw}$  explains part of this. A difference in the  $S(s)$  plot here versus the previous section is in the trend reversal at low frequencies. This trend reversal could be a result of the numerous other elements in  $T_{zw}$ , or possibly the "waterbed effect" or area rule that are explained in Chapter III. There could be advantages to each case for disturbance rejection, depending on the disturbance frequency. The change in the upper complex gain margin of Table 4-3, that did not show a pattern, is explained by the maximum magnitude of  $S(s)$  being lowest in the 50 dB dc gain case. By choosing a dc gain between 50 and 60 dB, the two sensitivity peaks could be equalized in magnitude to give the best upper

complex gain margin.

The complimentary sensitivity magnitude in Figure 4-25 explains the rise in the lower complex gain margin as the dc gain of  $W_i(s)$  increases. As for fine tuning the peaks of  $S(s)$  for a better upper complex gain margin, it is evident that this would decrease the lower complex gain margin, which is largest for the 60 dB dc gain. A drawback to increasing the lower margin by raising the dc gain of  $W_i(s)$  is the much larger noise feedthrough for the sensor, which is also a decrease in the allowable multiplicative uncertainty at high frequencies, but the highest dc gain cases do stabilize the higher order model.

The closed-loop transfer function magnitude used for tracking is shown in

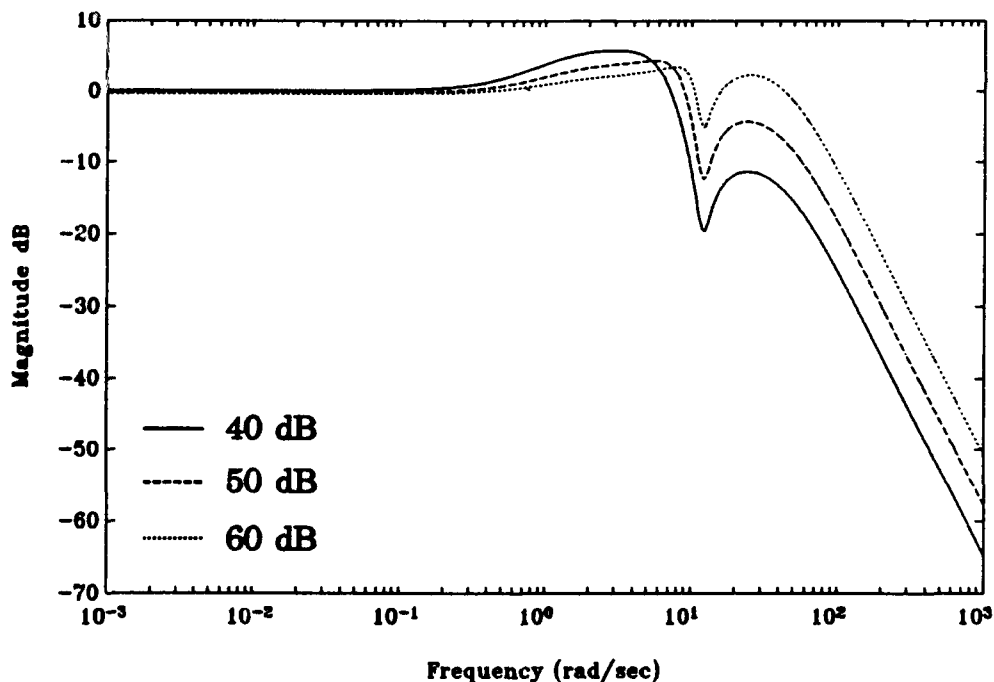


Figure 4-25. Complimentary Sensitivity Magnitude, LO

Figure 4-26. This is the transfer function given in  $y_g(s)/r(s) = S(s)G(s)K_r(s)$ . Clearly, the fastest responding tracker is the case of the highest dc gain in  $W_i(s)$ . This magnitude curve breaks away from one (or 0 dB) around 10 rad/sec, whereas the lower dc gains in  $W_i(s)$  cause earlier departures of this magnitude from the 0 dB line. The earlier departure can be crucial to tracking, depending on the frequency of the input and the rise time needed. As an aside, this plot also shows that any high frequency noise that enters with the input signal is amplified at increasing levels as the dc gain of  $W_i(s)$  is increased. Comparing Figure 4-26 to the previous plot of  $T(s)$ , a definite difference is noticed. It is the peak of  $T(s)$  that disrupts good tracking performance in the sensitivity section, and the large tracking overshoot comes

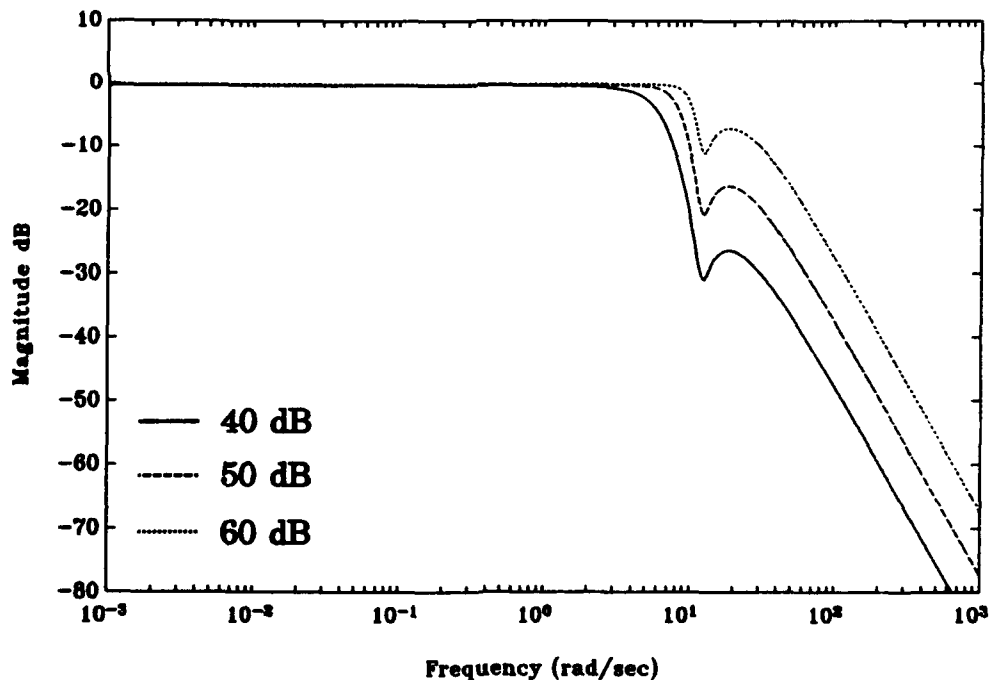


Figure 4-26. Closed-Loop Transfer Function Magnitude, LO

from the peak of  $T(s)$  being above the 0 dB line. By using the 2 DOF controller design this overshoot problem is circumvented by the feedforward compensator, which is mainly dependent on the tracking error weight  $W_t(s)$ .

In order to look at the noise effects on control usage, the magnitude of  $K_b(s)S(s)$  is given in Figure 4-27. This uncovers a tradeoff that introduces a problem into the seemingly good design. It is evident that high frequency noise will corrupt the control usage at increasing levels of  $W_t(s)$  dc gain. The jump in magnitude around 20 rad/sec is almost exactly 8 dB for each 10 dB shift up in the dc gain of  $W_t(s)$ . Thus, even though the previous figure shows the bandwidth increasing as the dc gain rises, the burden of increased noise corrupting the plant input is the tradeoff. Another drawback to the higher dc

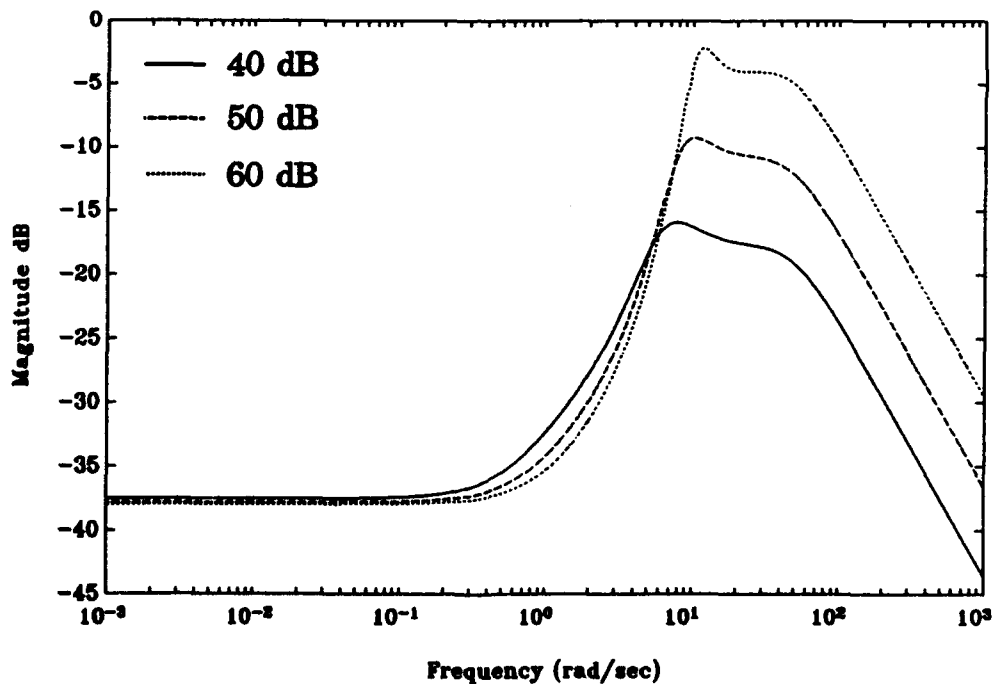


Figure 4-27. Magnitude of  $K_b(s)S(s)$ , LO

gain case is the lower allowable plant additive uncertainty in the high frequency range.

The time responses begin as before with the regulation of the initial angle-of-attack perturbation. The  $\alpha$  response due to an  $\alpha(0)$  of 5 degrees is shown in Figure 4-28 and demonstrates trends similar to the previous section. Initial overshoot and oscillations of the  $\alpha$  response increase as the dc gain of  $W_i(s)$  rises. Although the  $\alpha$  response shapes are different from each other, the time to regulate the perturbation is relatively constant at 1.5 seconds. Larger amounts of low frequency noise are evident in the case with the lower dc gain. Remember the concentration here is for a good tracker, even though the regulation responses appear to be acceptable in a practical sense.

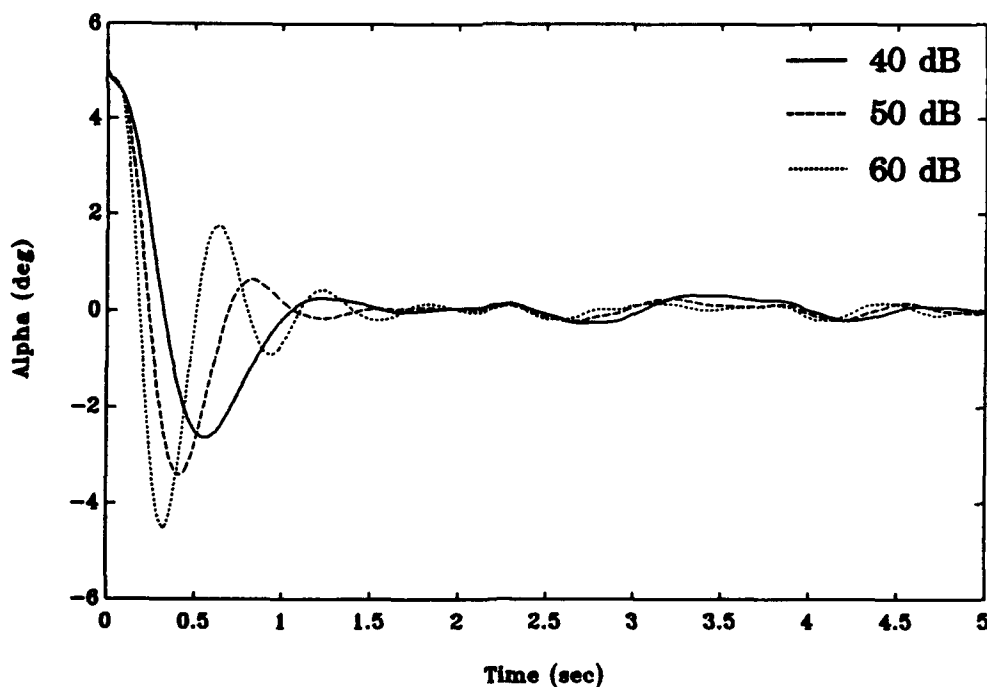


Figure 4-28.  $\alpha$  from  $\alpha(0) = 5$  deg, LO

The effect of noise on the control usage is somewhat visible in Figure 4-29. As mentioned in the discussion of the magnitude plot for  $K_b(s)S(s)$ , the noise (mainly high frequency) that affects the control usage increases as the dc gain of  $W_i(s)$  rises. With the scale of Figure 4-29 it is hard to see the noise effects, but the separate plots of each case confirmed the noise corruption was the largest in the 60 dB gain case. The other problem with this 60 dB gain case is that the elevator deflection reaches 38 degrees, which is beyond practical limits of the F-16. Using 50 dB as the low frequency gain of  $W_i(s)$  gives a maximum elevator deflection of around 21 degrees. Recall that elevator deflection is the output of the servo, not the input to the servo (which is this plot). The regulation time coincides with the

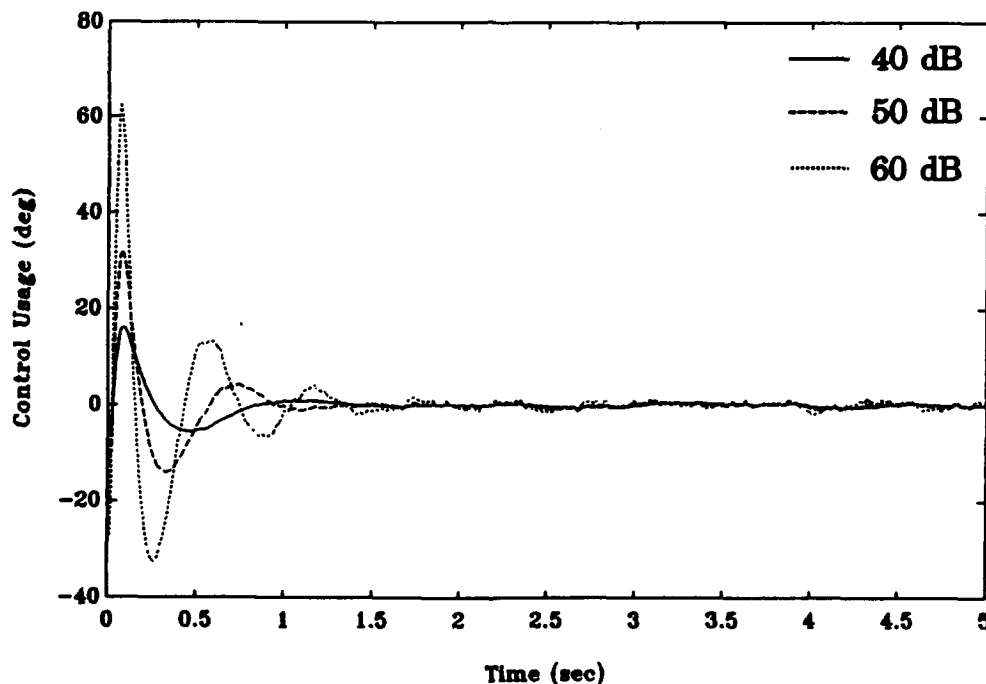


Figure 4-29. Control Usage ( $u$ ) from  $\alpha(0) = 5$  deg, LO



previous  $\alpha$  time response figure for this perturbation in being around 1.3 to 1.5 seconds.

The tracking response for a step input is Figure 4-30. Note that the overshoot is much less than in the sensitivity design, but with rise times being slightly longer. The trend in rise times getting lower as the dc gain of  $W_1(s)$  increases is foreshadowed by the closed-loop transfer function magnitude plot of Figure 4-26. The return towards small steady state error is very fast for all three cases, although the large amount of simulation noise makes this hard to decipher. Low frequency noise corrupts the 40 dB dc gain simulation the most, with the 60 dB dc gain case showing a combination of high and low frequency corruption.

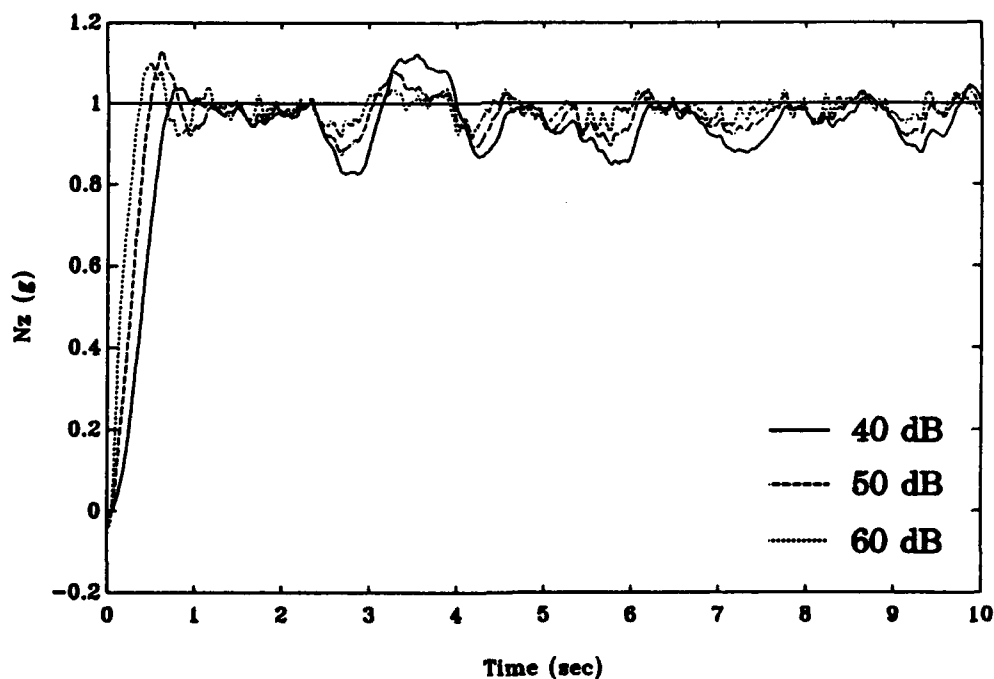


Figure 4-30.  $N_z$  from  $N_z$  Command Step, LO

Concern for the low bandwidth causing slow rise times led to the examination of the decade shift in the pole of  $W_i(s)$ , with the dc gain fixed at 50 dB. The 2-norm value and margins are also shown in Table 4-3 for these two extra cases (magnitude plots and time responses are not shown). When the pole is moved up one decade,  $s = -1$ , the rise time decreases because the bandwidth goes up. As a matter of fact the rise time decreased a large amount; about half of what it is for the  $s = -0.1$  case. The tradeoff is in lower complex margins, because the peaks of  $S(s)$  and  $T(s)$  both rose, and in more noise corruption to the plant output and control usage. All frequency plots tend to shift their peaks to the right, i.e. the plot of  $K_b(s)S(s)$  not only grew in magnitude but it moved to higher frequency, indicating higher frequency noise corruption for the control usage. Most response histories were very oscillatory in this case, as expected from the very fast rise time.

When this same pole in  $W_i(s)$  is moved to a lower frequency by one decade,  $s = -0.01$ , the exact opposite of the previous  $s = -1$  case occurs. The  $N_z$  response is slower and low frequency noise corrupts it more. The reason for the lower frequency noise corruption is that  $S(s)$  and  $T(s)$  have their peaks increased and moved left when compared to the baseline case. The magnitude peak of  $K_b(s)S(s)$  moves to a lower frequency and its overall magnitude decreases. Hence, moving the pole of  $W_i(s)$  (with fixed dc gain) gives information that this weight change could also be used to alter design parameters.

The evaluation results can be concluded as:

- i). Two stabilizing trackers are found, and both exhibit good  $N_z$  command following properties. The 60 dB dc gain case has large deflections for the  $\alpha$  initial condition, but this 5 degree perturbation is very large to begin with.
- ii). The 50 dB dc gain case has good regulation features, much better than the stable  $H_2$ /Sensitivity baseline case.
- iii). Limited shaping of the sensitivity transfer function is possible with the weight on tracking.
- iv). Rise times for the two stable cases are a little slower than the sensitivity designs, although they seem fast enough from a practical sense.
- v). The allowable additive and multiplicative uncertainties decrease at high frequencies as the dc gain of  $W_t(s)$  rises.
- vi). The high frequency compensator magnitude increases as the dc gain of  $W_t(s)$  does, and cancels the plant's complex zero pair better.
- vii). The loop shape at low frequencies decreases as the dc gain of  $W_t(s)$  increases, but the loop shape above approximately 0.1 rad/sec increases as the dc gain of  $W_t(s)$  increases.
- viii). Raising the dc gain of  $W_t(s)$  gave lower rise times for tracking the  $N_z$  step and gave more of an oscillatory response for regulating the initial  $\alpha$  perturbation. Control usage increased greatly as the dc gain of  $W_t(s)$  was raised.

As a summary of the  $H_2$  design chapter, continued progress is seen by first

weighting sensitivity, and then using a 2 DOF controller with a tracking weight. In the basic LQG design, good  $\alpha$  regulators are achievable, but the higher order model is unstable. Furthermore, good tracking is not found, and the sensitivity transfer function is not shaped to reject low frequency disturbances. By adding the sensitivity weighting in Section 4.2, a preferred sensitivity magnitude is found that helps reject low frequency disturbances and indirectly causes a very small steady state tracking error. Most importantly, the goal of the sensitivity section is accomplished by designing a controller that stabilizes the higher order system. The stabilizing controller from the sensitivity design is a good tracker, but a poor regulator. With the focus on a 2 DOF controller in this section, two stabilizing cases are seen that both give good tracking. One of these is also a good regulator for the  $\alpha$  perturbation, the baseline case. This baseline 2 DOF tracking case appears to be the best design when considering the regulation of the  $\alpha$  perturbation, tracking a 1 G step, and stabilizing the higher order model. Now the design methodology will change to the  $H_\infty$  type, with again stabilizing compensators that give good performance being the goal of the weight selection/location process.

## V. $H_\infty$ Design

### 5.1 $H_\infty$ /Robust Tracker

The purpose of this chapter is to show an  $H_\infty$  design for a robust tracker. Previously,  $H_2$  regulators and trackers have demonstrated very good performance traits, but had tendencies to destabilize the higher order model because of the additional phugoid mode. This is no surprise since the  $H_2$  methodology does not directly address robustness to plant variations, as the  $H_\infty$  process does. The  $\infty$ -norm is much more powerful in this uncertainty environment because of its submultiplicative property. The Small Gain Theorem (SGT) can be combined with this submultiplicative property to yield a robustness level that depends on  $\|T_{ed}\|_\infty$  [Zam66]. The level of robustness is  $\|\Delta\|_\infty$ ; if  $\|T_{ed}\|_\infty$  is less than  $1/\|\Delta\|_\infty$ , the robustness test is passed. Although this does look very straightforward and preferable as a test for allowable uncertainty, the results of failing this test actually give no information on stability of the closed-loop system for the given  $\|\Delta\|_\infty$ . Not only is this robustness test conservative from the submultiplicative property and the SGT, but it also depends on  $\infty$ -norms that are the maximum magnitude of a transfer function over all frequency. The exact frequency that may be of interest (possibly phugoid frequency) could actually have large allowable uncertainties, yet the robustness test may fail because of a peak at a

completely meaningless frequency. Weighting functions may be introduced into the design to help alleviate this problem. Even though this test appears to be a major advantage, in many cases it yields no useful information, as will be seen in this section. If this test is failed, there actually is some  $\Delta(s)$ , not necessarily linear or time-invariant, that will destabilize the closed-loop system  $T_{ed}$ . When the robustness test does fail, closing the loop and checking the poles is the recourse. The compensator is still optimized for this  $\Delta(s)$  since the  $\infty$ -norm of  $T_{ed}$  is always being minimized with the  $H_\infty$  optimal design, and whether the robustness test for a certain  $\Delta(s)$  fails or not, it is still true that

$$\|T_{ed}\|_\infty < \frac{1}{\|\Delta\|_\infty} \quad (5.1)$$

for guaranteed closed-loop stability. Therefore, minimizing  $\|T_{ed}\|_\infty$  is still maximizing the allowable  $\|\Delta\|_\infty$ . This  $T_{ed}$  is the unweighted closed-loop transfer function from  $d$  to  $e$ . Another common method is to make chosen weights overbound the magnitude of an expected  $\Delta(s)$ , then if  $\|T_{ed}\Delta\|_\infty < 1$  (or in other words  $\|T_{ed}W\|_\infty < 1$ ) the robustness test is passed.

The peak magnitude of  $K_b(s)S(s)$  gives the inverse of the allowable additive plant uncertainty as an  $\infty$ -norm value. This additive uncertainty plot of  $K_b(s)S(s)$  also gives the frequencies where the magnitude of the allowable uncertainty can be, and does not depend on only one maximum value over all frequency. Multiplicative uncertainty is a function of  $T(s)$ , whereas the

complex margins are based on  $\|T\|_{\infty}$  and  $\|S\|_{\infty}$ . Thus, the  $\infty$ -norm computations give the worst case gain margins, phase margins, and allowable uncertainties over all frequencies, but not necessarily the frequency that may be of interest.

The  $H_{\infty}$  controllers designed in this section are all optimal  $H_{\infty}$  designs with  $Q(s) = 0$  (i.e. central) in the [DGKF89] formulation.  $H_{\infty}$  suboptimal compensators are discussed in Section 5.2, although these will still be the central controller design. The optimal  $H_{\infty}$  designs are compared here because they represent minimizing  $\|T_{ed}\|_{\infty}$ . One problem that arises from using the optimal controller is in noise corruption. This is from the fact that noise energy is not being minimized as in  $H_2$ , and the  $H_{\infty}$  optimal compensator normally has a "D" term that allows more high frequency noise to pass through. Hence, time responses for the  $H_{\infty}$  optimal designs are shown without noise simulation since noise rejection is not the point of this section. Noise is included in the section on suboptimal controllers to show the advantage of backing off of the optimal  $\gamma$  value,  $\gamma_0$ . The criteria for finding  $\gamma_0$  in these cases is when the controller drops to the order of the design plant minus one, where the "D" term appears.

A reason for showing the central  $H_{\infty}$  controller is due to the problem of picking a  $Q(s)$  to use in the (J,Q)-type compensator parameterization for a noncentral controller, as seen in Chapter II. There really does not seem to be a well defined approach, other than mixed  $H_2/H_{\infty}$  optimization, to give a value

of  $Q(s)$  that would give results better than choosing  $Q(s) = 0$ .

The  $H_\infty$  design diagram is shown as Figure 5-1. Notice that the exogenous inputs are now denoted as  $d$  ( $w$  in  $H_2$  design), and the controlled outputs as  $e$  ( $z$  in  $H_2$ ). This notation change is to prevent confusion between the two different design methodologies. The exogenous inputs are now assumed to be

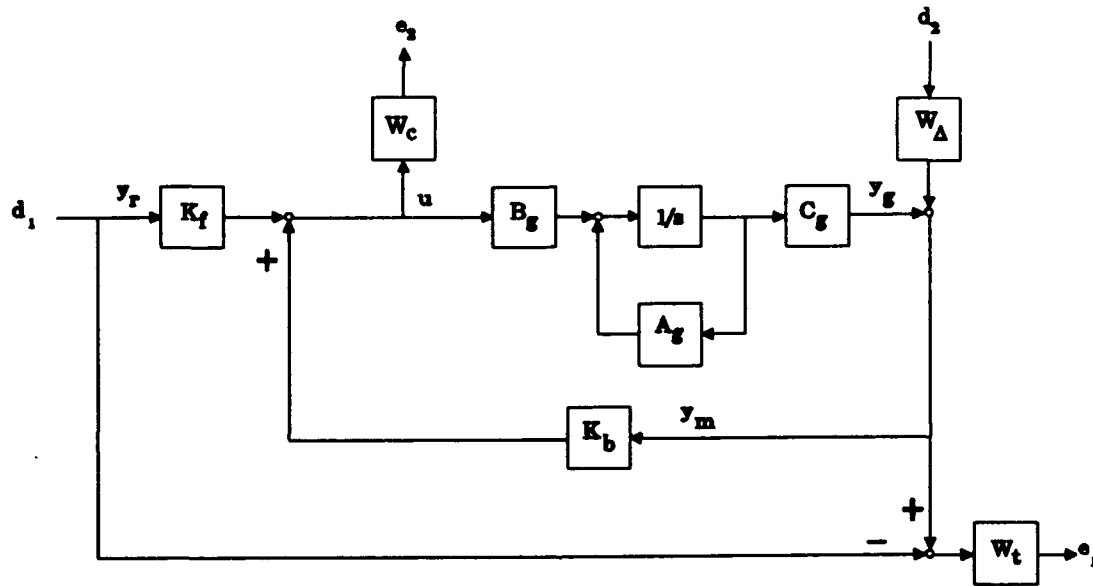


Figure 5-1.  $H_\infty$  Robust Tracker Design Diagram

bounded energy, not unit intensity white noise. The input  $d_2$  is at the plant output partly so that a  $\Delta(s)$  uncertainty can be input as additive to the design plant through the use of the  $W_\Delta(s)$  and  $W_c$  weights. As before,  $W_c$  is taken to be a scalar and its presence is necessary to satisfy [DGKF89] requirements. The combination of  $W_c$  and  $W_\Delta(s)$  is the additive plant  $\Delta(s)$  weight, i.e. the



magnitude of these should look like the expected  $\Delta(s)$  if only additive plant uncertainty is modelled. The tracking weight  $W_t(s)$  will again be a low-pass filter that penalizes the error between the commanded input  $d_1$  and the combination of the plant output and the weighted input  $W_\Delta(s)d_2$ . For this design the actual shape of  $W_\Delta(s)$  is also driven by the combined weight of  $W_t(s)$  and  $W_\Delta(s)$ , which will be the weight on sensitivity. This is covered in the upcoming discussion of  $T_{cd}$ . With these weights in mind, recall that the  $H_\infty$  optimal design will be minimizing  $\|T_{cd}\|_\infty$ . As in the  $H_2$  cases, the  $H_\infty$  design also needs to be manipulated into the state space form for the design plant  $P$ , given by

$$\begin{bmatrix} \dot{x}_s \\ \dot{x}_\Delta \\ \dot{x}_t \end{bmatrix} = \begin{bmatrix} A_s & 0 & 0 \\ 0 & A_\Delta & 0 \\ B_t C_s & B_t C_\Delta & A_t \end{bmatrix} \begin{bmatrix} x_s \\ x_\Delta \\ x_t \end{bmatrix} + \begin{bmatrix} 0 & 0 \\ 0 & B_\Delta \\ -B_t & B_t D_\Delta \end{bmatrix} \begin{bmatrix} d_1 \\ d_2 \end{bmatrix} + \begin{bmatrix} B_s \\ 0 \\ 0 \end{bmatrix} [u] \quad (5.2)$$

$$\begin{bmatrix} e_1 \\ e_2 \end{bmatrix} = \begin{bmatrix} D_t C_s & D_t C_\Delta & C_t \\ 0 & 0 & 0 \end{bmatrix} \begin{bmatrix} x_s \\ x_\Delta \\ x_t \end{bmatrix} + \begin{bmatrix} -D_t & D_t D_\Delta \\ 0 & 0 \end{bmatrix} \begin{bmatrix} d_1 \\ d_2 \end{bmatrix} + \begin{bmatrix} 0 \\ W_c \end{bmatrix} [u] \quad (5.3)$$

$$\begin{bmatrix} y_r \\ y_m \end{bmatrix} = \begin{bmatrix} 0 & 0 & 0 \\ C_s & C_\Delta & 0 \end{bmatrix} \begin{bmatrix} x_s \\ x_\Delta \\ x_t \end{bmatrix} + \begin{bmatrix} 1 & 0 \\ 0 & D_\Delta \end{bmatrix} \begin{bmatrix} d_1 \\ d_2 \end{bmatrix} + \begin{bmatrix} 0 \\ 0 \end{bmatrix} [u] \quad (5.4)$$

Like the  $H_2$  designs, there are several constraints that can be checked immediately. These are  $D_{cd} = 0$ ,  $D_{yu} = 0$ ,  $D_{cu}^T D_{cu}$  full rank, and  $D_{yd} D_{yd}^T$  full rank.  $D_{yu}$  is already equal to zero, and  $D_{yd} D_{yd}^T$  full rank will be met when  $W_\Delta(s)$  has a "D" term.  $D_{cu}^T D_{cu}$  full rank is satisfied for a nonzero  $W_c$ , and  $D_{cd} = 0$  can only result when  $D_t = 0$ , i.e.  $W_t(s)$  must roll off. A full discussion of these limitations is in [Gah92], and briefly discussed in Chapter II. Again the 2 DOF compensator is given by  $[K_f \ K_b]$  as in

$$[u] = [K_f \ K_b] \begin{bmatrix} y_r \\ y_m \end{bmatrix} \quad (5.5)$$

As before, the poles of  $K_f(s)$  and  $K_b(s)$  will be the same. Now that the design setup is established, the weightings in Figure 5-1 can be examined.

### **5.1.1 $H_\infty$ /Robust Tracking Weight Selection**

A key to selecting available weights in this  $H_\infty$  design is with the  $W_\Delta(s)$  transfer function. From Figure 5-1, it is the combination of  $W_\Delta(s)$  and  $W_c$  that is the direct weight on additive uncertainty for the plant. The weights  $W_\Delta(s)$  and  $W_t(s)$  are constraints on the sensitivity transfer function, and will be used to try and lower the magnitude of  $S(s)$  around the phugoid frequency. Refer to the models of multiplicative and additive uncertainty, Figures 3-2 and 3-3, for the uncertainties between the lower order and higher order models. The  $W_\Delta(s)$  weight is chosen as a low-pass filter since the phugoid (at

0.07 rad/sec) is destabilizing the higher order model. If this is modelled as an additive plant uncertainty,  $W_c$  and  $W_\Delta(s)$  can be used to improve the allowable additive uncertainty. Since  $W_c$  is a scalar, it serves to raise or lower the magnitude shape of  $W_\Delta(s)$ . In this design  $W_c$  and  $W_\Delta(s)$  weight the high frequency additive uncertainty since the low frequency magnitude of  $K_b(s)S(s)$  will follow the inverse magnitude of the design plant (magnitude of  $K_b(s)S(s)$  tends to start at -37.5 dB), and the low frequency magnitude of the plant is larger than the dc gain of  $W_c W_\Delta(s)$ . This inverse magnitude following of the design plant, at frequencies where the compensator has large magnitudes only, is the same as discovered in most  $H_2$  designs. The commonly referenced transfer function  $K_b(s)S(s)$  is with  $W_\Delta(s)$  and  $W_c$  in the (2,2) element of  $T_{ed}$ , represented by the transfer function matrix

$$T_{ed} = \begin{bmatrix} W_t(s)(S(s)G(s)K_r(s)-1) & W_t(s)S(s)W_\Delta(s) \\ W_c K_r(s)S(s) & W_c K_b(s)S(s)W_\Delta(s) \end{bmatrix} \quad (5.6)$$

As in the  $H_2$  tracking design,  $W_t(s)$  is the direct weight on the tracking error  $S(s)G(s)K_r(s)-1$ , in the  $T_{ed}(1,1)$  transfer function. Hence, this error needs to be small at low frequencies to ensure that the magnitude of  $S(s)G(s)K_r(s)$  is close to one. The other element of importance is  $T_{ed}(1,2)$ , containing the sensitivity transfer function. This is weighted by the combination of  $W_t(s)$  and  $W_\Delta(s)$ , which makes a large penalty at low frequencies. One purpose of the

$W_\Delta(s)$  weight on  $S(s)$  comes from the fact that very large magnitude weights on the tracking error create time responses in which the elevator deflection tends to pass the 25 degree limit. Most importantly, the magnitude of  $S(s)$  can be penalized severely at low frequencies (i.e. phugoid frequency), unlike the  $H_2$  designs where low frequency weights are less important because of the frequency integral used in the 2-norm calculation. Also in the  $H_2$  designs the higher frequency peak of  $S(s)$  increased greatly when trying to drive the low frequency magnitude of  $S(s)$  down, a result of the "waterbed effect". The (2,1) element of  $T_{ed}$  is not an area of concentration since tracking is being controlled by the (1,1) term, and  $K_r(s)$  appears in this  $T_{ed}(2,1)$  transfer function. Now that the design has been discussed and weight dependencies analyzed, the focus shifts to design results.

### **5.1.2 $H_\infty$ /Robust Tracking Results**

Low-pass filters for  $W_\Delta(s)$  and  $W_t(s)$  are kept for all cases, as is a scalar  $W_c$ .  $W_\Delta(s)$  is chosen with a dc gain of 20 dB and a pole at 0.1 rad/sec to help weight the low frequency magnitude of  $S(s)$ . A zero at 1 rad/sec is added to  $W_\Delta(s)$  to give a nonzero  $D_\Delta$  term in  $D_{yd}$  so that [DGKF89] requirements are met. The tracking weight starts with a 40 dB dc gain, and a pole at 0.05 rad/sec. Iterations were then performed on  $W_c$  to yield results comparable to the time responses of the  $H_2$  tracking section. The resulting  $W_c$  value was taken to be  $W_c = 5$ . This becomes the "baseline" selection that is

seen as the second row of Table 5-1 (boldface). The same  $W_\Delta(s)$  is held for all cases in Table 5-1 since the higher order system is stable for each. First the pole location in  $W_t(s)$  is shifted left and right (i.e. to lower and higher frequencies) to examine the responses and margins. The first four rows of Table 5-1 show that the complex gain margins seem to jump with the pole shift from 0.025 to 0.05 rad/sec, then the lower margin increases while the upper margin decreases with the pole moving to 0.075 and 0.1 rad/sec.

Table 5-1.  $H_\infty$ /Robust Tracking Results, LO

$W_t(s)$ pole (rad/sec)	$W_c$	$\ T_{cd}\ _\infty$ Weighted ( $\gamma_o$ )	Bode Gain Margin (dB)	Bode Phase Margin (deg)	Complex Gain Margin (dB)	Complex Phase Margin (deg)
0.025	5.0	1.2208	-7.7, 13.2	$\pm 34$	-6.1, 7.4	$\pm 33$
<b>0.05</b>	<b>5.0</b>	<b>1.7753</b>	<b>-9.3, 10.8</b>	<b><math>\pm 39</math></b>	<b>-7.3, 9.0</b>	<b><math>\pm 38</math></b>
0.075	5.0	2.2221	-10.3, 9.8	$\pm 43$	-8.1, 8.8	$\pm 37$
<b>0.1</b>	<b>5.0</b>	<b>2.6064</b>	<b>-11.1, 9.1</b>	<b><math>\pm 46</math></b>	<b>-8.8, 8.0</b>	<b><math>\pm 37</math></b>
0.05	2.5	1.3082	-10.9, 9.1	$\pm 46$	-8.7, 8.0	$\pm 37$
<b>0.05</b>	<b>7.5</b>	<b>2.1307</b>	<b>-8.4, 12.0</b>	<b><math>\pm 36</math></b>	<b>-6.6, 8.0</b>	<b><math>\pm 35</math></b>

The complex phase also shows an increase up to  $\pm 38$  degrees for the baseline case, then it stays approximately the same for the pole at 0.075 and 0.1 rad/sec. Changing the value of  $W_c$  is then checked for the baseline case.

The reason for choosing this baseline case is that the  $W_t(s)$  pole location of 0.025 rad/sec causes a slow time response for a step input, and the cases of pole locations at 0.075 and 0.1 rad/sec both have elevator deflections (due to the initial  $\alpha$  of 5 degrees) above the 25 degree limit for the F-16. The bottom two rows of Table 5-1 are for  $W_c$  values of 2.5 and 7.5, respectively.

Margins for the  $W_c = 2.5$  case match closely with the row above it that represents the fastest  $W_t(s)$  pole, whereas the  $W_c = 7.5$  case is closer to the slowest  $W_t(s)$  pole of 0.025 rad/sec. The  $W_c = 2.5$  case also has an elevator deflection that exceeds 25 degrees for an initial  $\alpha$  of 5 degrees.

The three cases chosen for magnitude and time response plots are the underlined ones in Table 5-1. The  $W_t(s)$  pole at 0.05 rad/sec with the  $W_c$  value of 5, which is the baseline, appears in the magnitude and time response plots as the solid line. The  $W_t(s)$  case with the fastest pole, at 0.1 rad/sec, is the dashed line. A dotted line represents the case of  $W_c = 7.5$  with the  $W_t(s)$  pole at 0.05 rad/sec.

Figure 5-2 is the singular value plot for  $T_{ed}$ . The pair of lines for each case are the two singular values, since  $T_{ed}$  is a 2 x 2 transfer function matrix. The maximum singular value of  $T_{ed}$  is flat for  $H_\infty$  optimal designs, i.e. it appears to be an all-pass filter as described in Chapter II. Hence, the value of  $\gamma_o$  is equal to  $\|T_{ed}\|_\infty$  for these optimal cases (as seen on the vertical magnitude axis of the Figure 5-2), and is shown to be the same as that given in Table 5-1.

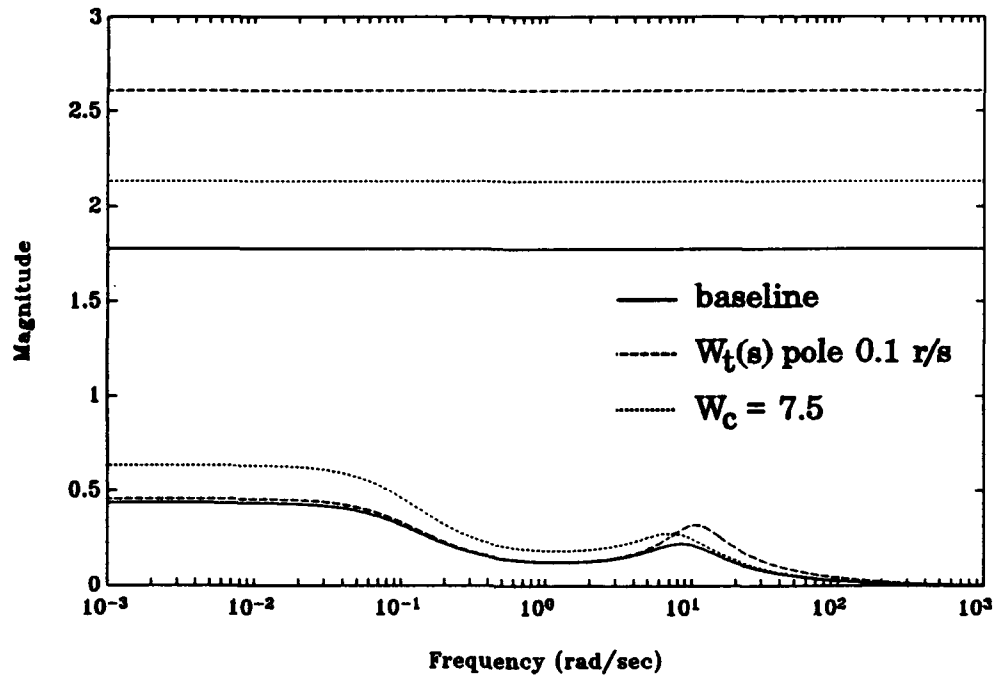


Figure 5-2. Singular Values of  $T_{cd}$ , LO

The next two plots, Figures 5-3 and 5-4, represent the feedforward and feedback compensators, respectively. As in the  $H_2$  tracking section that is also 2 DOF, the magnitudes here are very similar in shape. At low frequencies where tracking is weighted, these should be the same because the low frequency magnitude of  $T(s)$  is fine for tracking. The problem with using  $T(s)$  as the closed-loop transfer function is in the peak above 0 dB and the possible early roll off. It will be seen that the compensator magnitudes differ at frequencies where  $T(s)$  and the closed-loop transfer function are not the same magnitude, i.e. the magnitude of  $T(s)$  rises above the 0 dB line. Other than this change in compensator magnitude because of  $T(s)$ , the feedback

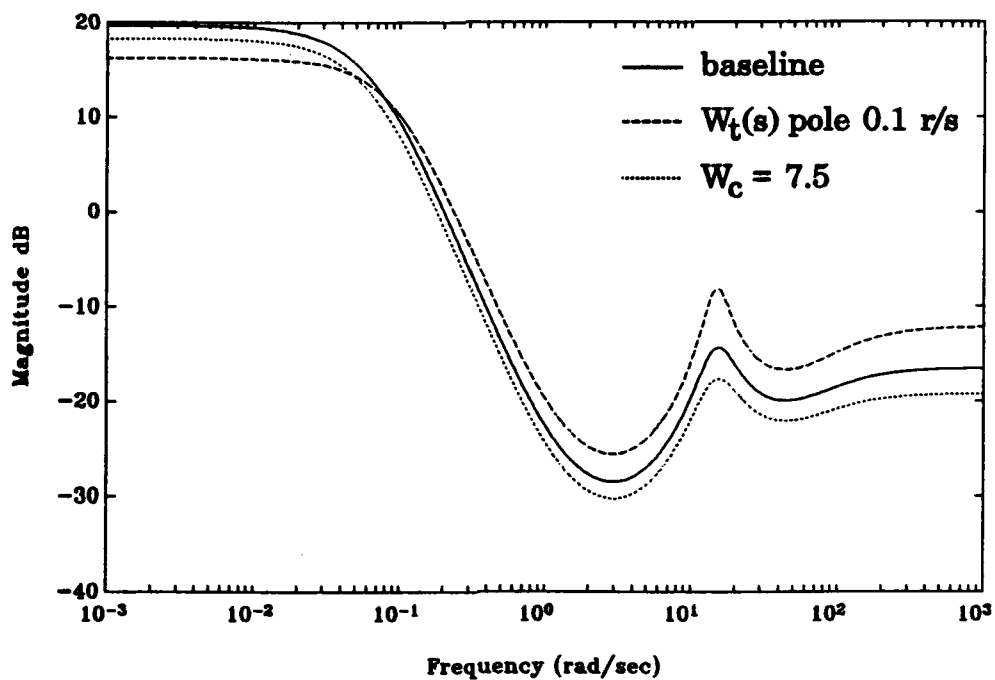


Figure 5-3. Feedforward Compensator Magnitude

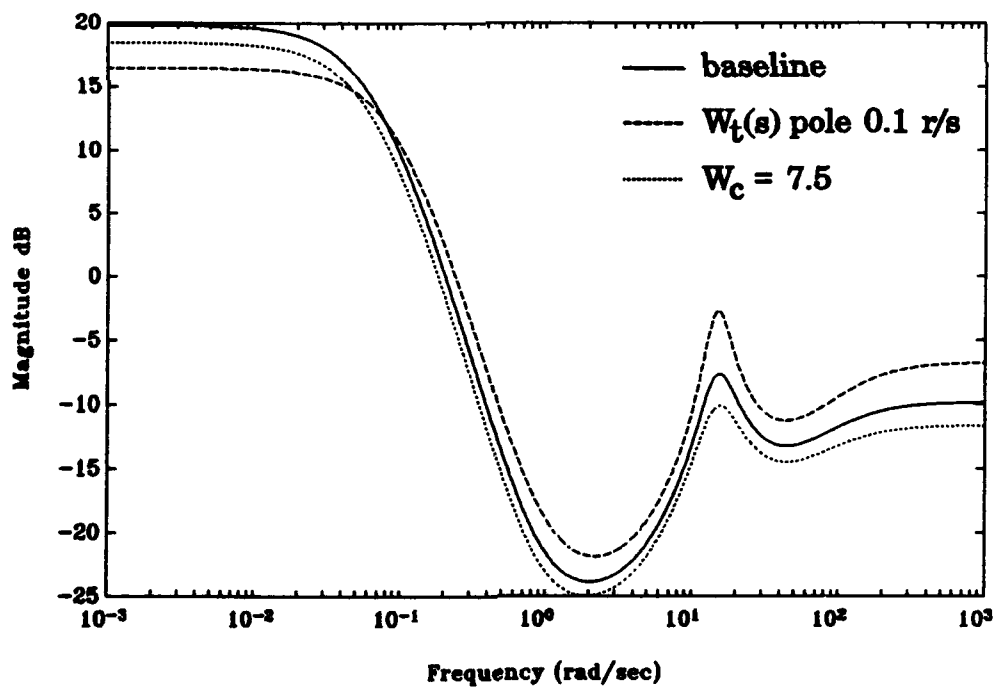


Figure 5-4. Feedback Compensator Magnitude



compensator in Figure 5-4 shows the large spike in notching out the plant complex zero for the  $W_t(s)$  pole at 0.1 rad/sec. Both compensators show the baseline with the highest gain at low frequencies, and  $W_t(s)$  with the pole at 0.1 rad/sec will pass the most high frequency noise through. Note that because of the "D" term in the state space of  $K(s)$ , the compensator magnitudes do not roll off.

Figure 5-5 is the magnitude of the open-loop transfer function. All three cases exhibit very high gain at low frequency. Moving the pole of  $W_t(s)$  right shifts the loop shape right (to a higher frequency), but lowers the low frequency gain slightly. Raising  $W_c$  appears to shift the whole magnitude curve down.

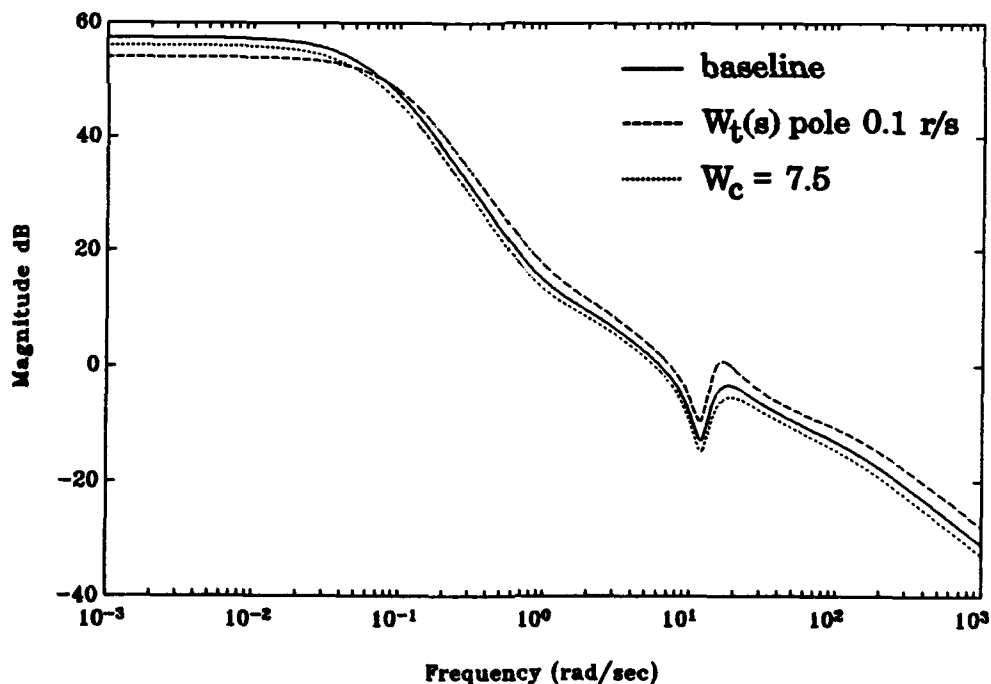


Figure 5-5. Magnitude of  $G(s)K_b(s)$ , LO

The magnitude of the sensitivity transfer function is Figure 5-6. As expected from the loop shape plot, the low frequency gain of  $S(s)$  is very low. The small magnitudes at low frequencies are from the combination of the  $W_t(s)$  and  $W_\Delta(s)$  weights, and the use of the  $\infty$ -norm on  $T_{cd}$ . The typical double peak of  $S(s)$  is seen here, with the baseline case being the most favorable for the complex margins (at least the part of the complex margins that depend on the sensitivity magnitude). Notice that the "waterbed effect" and area rule are the likely reason for the low frequency magnitude of the  $W_t(s)$  pole at 0.1 rad/sec case rising.

Figure 5-7 is the magnitude plot for the complimentary sensitivity. The high frequency trend is expected here since it closely resembles the high

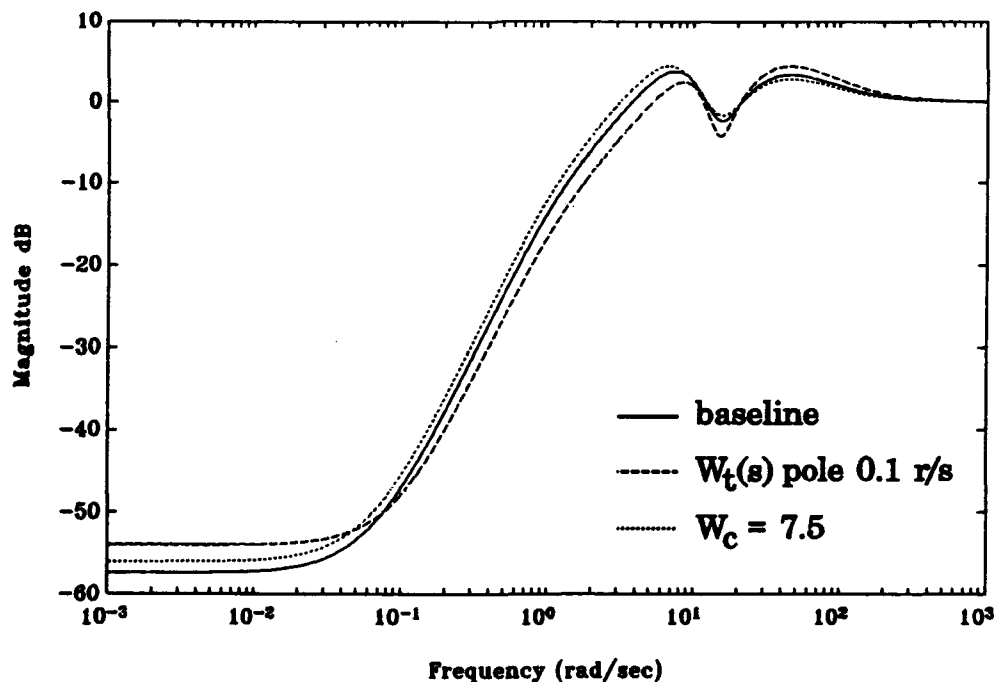


Figure 5-6. Sensitivity Magnitude, LO

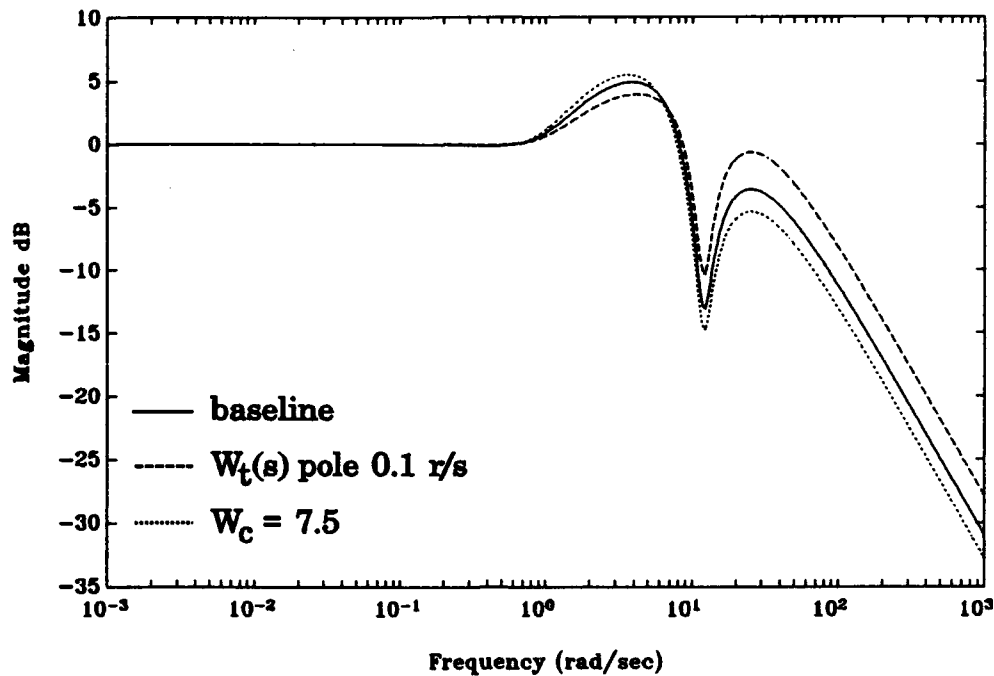


Figure 5-7. Complimentary Sensitivity Magnitude, LO

frequency magnitude of the loop shape, Figure 5-5. A tradeoff is apparent in that the case with the best margin (peak of dashed curve is the lowest) will attenuate the least amount of measurement noise, if the noise were included in simulations. The highest peak of  $T(s)$  is in the  $W_c = 7.5$  case, and this would have the least high frequency noise feedthrough from the sensor.

The closed-loop transfer function magnitude in Figure 5-8 clearly shows that the dashed curve ( $W_t(s)$  pole at 0.1 rad/sec) will be the fastest in time responses, and the dotted line ( $W_c = 7.5$ ) will have the longest rise times. Also note that the low frequency gain of the closed-loop transfer function is slightly below 0 dB. This has been shown before and comes from the tracking

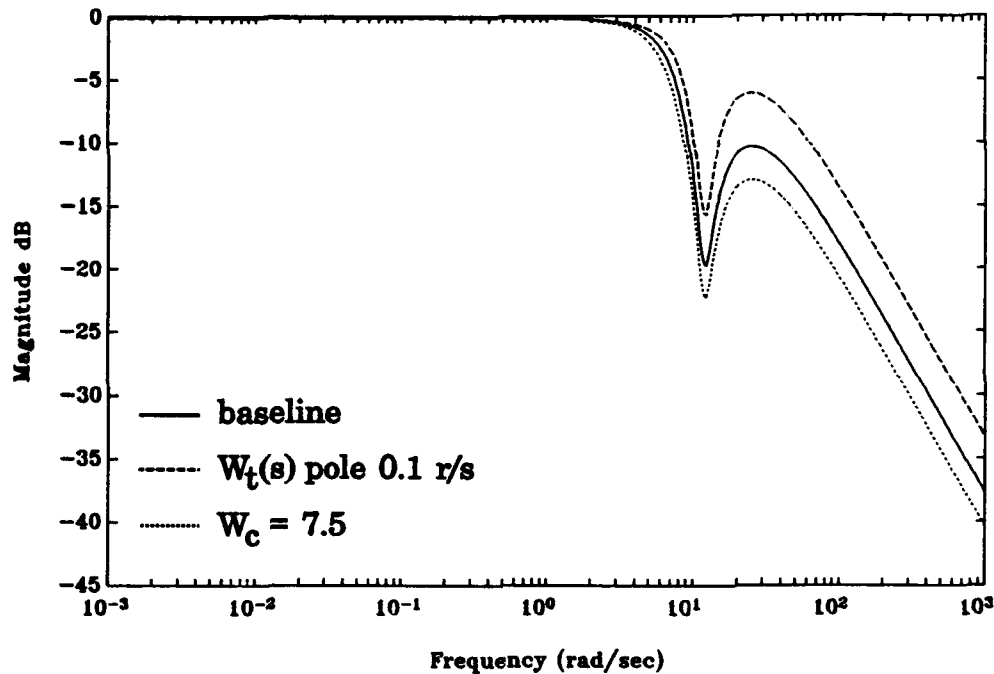


Figure 5-8. Closed-Loop Transfer Function Magnitude, LO

weight not having large enough gain at low frequency. The problem with correcting this in the design is that in theory an infinite dc gain of  $W_i(s)$  would need to be employed to penalize this low frequency error enough to get the magnitude of  $S(s)G(s)K_f(s)$  to be 0 dB (or magnitude 1), at low frequency. An easy solution would be to increase the dc gain of  $K_f(s)$  after the design process. The case with the  $W_i(s)$  pole at 0.1 rad/sec will pass the largest amount of command signal noise to the plant output. As mentioned in the compensator magnitude plots, the differences in  $K_f(s)$  and  $K_b(s)$  should be where the magnitude of  $T(s)$  starts to rise above 0 dB, and the closed-loop transfer function magnitude cannot follow this rise. Thus, the 2 DOF design

again gets away from using an unfavorable  $T(s)$  as the closed-loop tracking transfer function. The peak magnitude of  $T(s)$  could actually double an input if it were in the frequency range of 3 to 5 rad/sec.

The magnitude of  $K_b(s)S(s)$  is shown in Figure 5-9. This is the transfer function that is weighted in  $T_{ed}(2,2)$ , and represents the allowable plant additive uncertainty (inverted that is). The combined  $W_c W_\Delta(s)$  weight on  $K_b(s)S(s)$  weights the high frequency gain since the low frequency magnitude is following the inverse of the design plant. The case with the  $W_t(s)$  pole at 0.1 rad/sec represents the least allowable additive uncertainty at high frequencies, and the  $W_c = 7.5$  case yields the most. Also note that the noise corruption for control usage is worse in the case with the least allowable

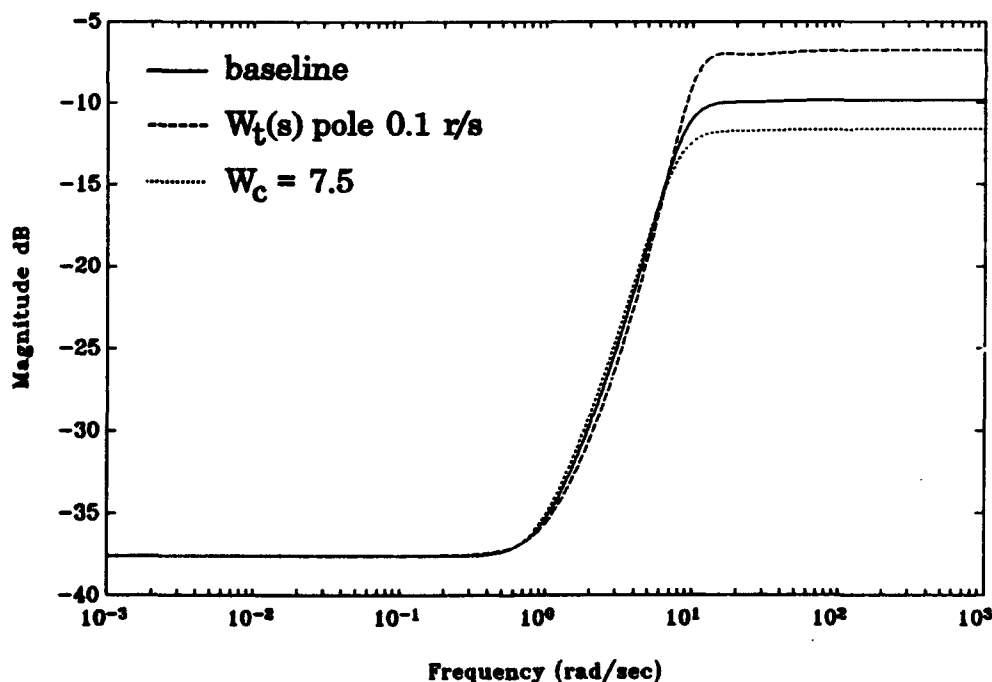


Figure 5-9. Magnitude of  $K_b(s)S(s)$ , LO

additive uncertainty. The concentration of this plot in the  $H_2$  chapter was in the fact that it is also showing the feedthrough of the disturbance and measurement noise to control usage. It is seen that all three cases fail the robustness test when the difference in the lower order and higher order models is lumped into only additive uncertainty, because the peak of the additive  $\Delta(s)$  magnitude is near 50 dB at 0.07 rad/sec (well above the 37.5 dB allowable at that frequency). Refer back to Figure 3-3 for the plot of additive plant uncertainty between the lower and higher order models. Failing this robustness test **does not** imply that the higher order closed-loop system is unstable since this robustness test is conservative, and the higher order system in all runs is in fact stable. Another note is that the phugoid comes into play at 0.07 rad/sec where all magnitudes fall on top of each other (because of the high compensator gains at low frequencies), and the high frequency area where the allowable additive  $\Delta(s)$  is changing is not very critical in **this design** for stabilizing the higher order model. The stress is placed on **this particular design** because in many other cases the uncertainty could easily be at high frequencies, and this is commonly the way it is modelled.

Figure 5-10 is the step response for an  $N_z$  command that shows the overshoot and steady state error. The overshoot is typical in that the fastest response has the largest amount. The steady state error goes back to the closed-loop transfer function magnitude not being exactly 0 dB at low frequencies, which would be the only advantage of using  $T(s)$  as the

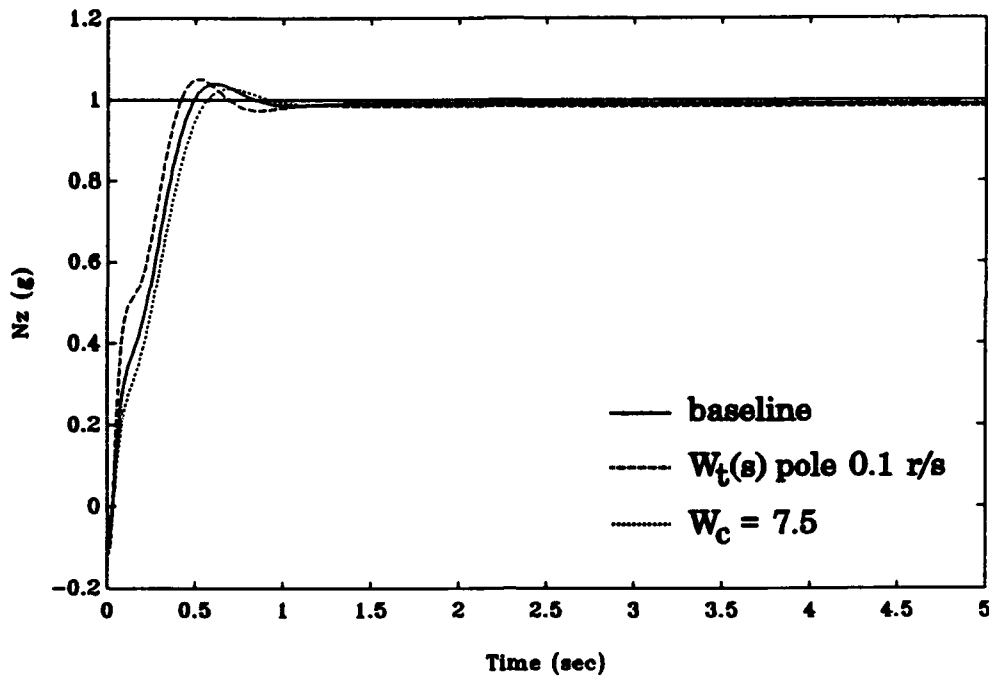


Figure 5-10.  $N_z$  for  $N_z$  Command Step, LO

closed-loop transfer function; that is without a post-design modification to  $K_f(s)$ . A steady state error is not obvious in the  $H_2$  responses since the large amount of simulation noise tends to cover it up. The baseline case reaches 1 G in 0.5 seconds, and as expected the  $W_c = 7.5$  case is the slowest of the three.

Regulation of the initial  $\alpha(0) = 5$  degrees appears to be very good for all three cases in Figure 5-11. The solid line ( $W_t(s)$  pole at 0.05 rad/sec,  $W_c = 5.0$ ) is somewhat of a compromise of the other two responses, and all three regulate the initial  $\alpha$  back to zero in about 1.5 seconds. The responses of these three cases are similar to the baseline case from the previous  $H_2$

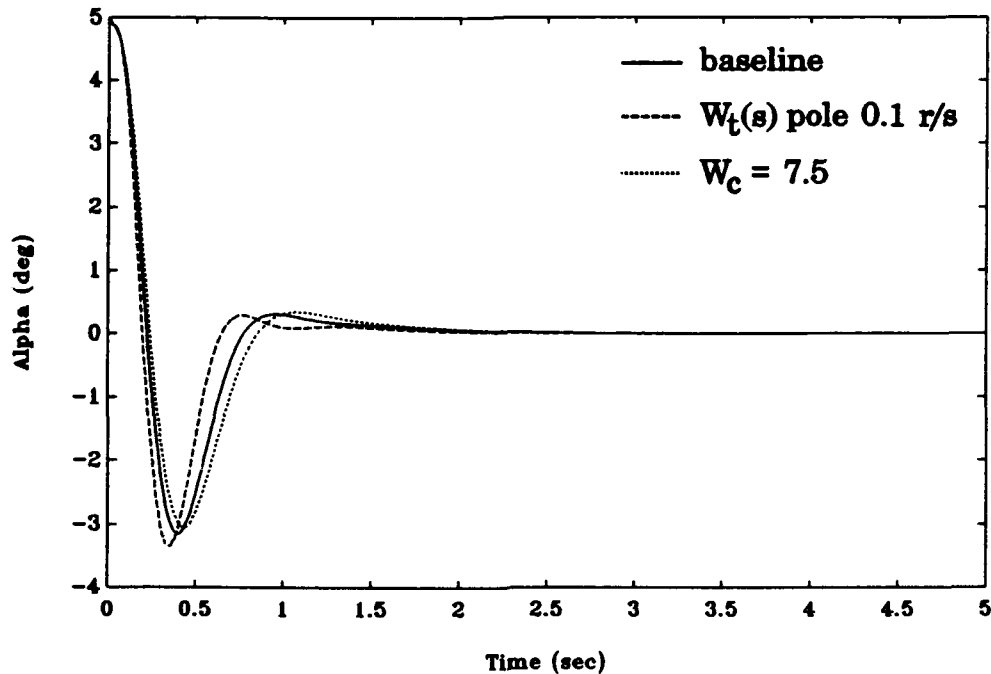


Figure 5-11.  $\alpha$  from  $\alpha(0) = 5$  deg, LO

tracking design. In a comparison, the  $H_\infty$  responses appear to be slightly better than the  $H_2$  ones, but the  $H_\infty$  cases do not have simulated noises.

Elevator deflection for the initial  $\alpha(0) = 5$  degrees is Figure 5-12. The most important feature is that the fastest case ( $W_t(s)$  pole at 0.1 rad/sec) breaks the 25 degree elevator limit. This is for a 5 degree  $\alpha$  though, which is fairly large. The response here parallels the other plots in that the faster regulator uses larger deflections, and similarly the slower regulator uses the least elevator deflection. Elevator deflection, not control usage, is plotted since the point is not to show noise effects in this design.



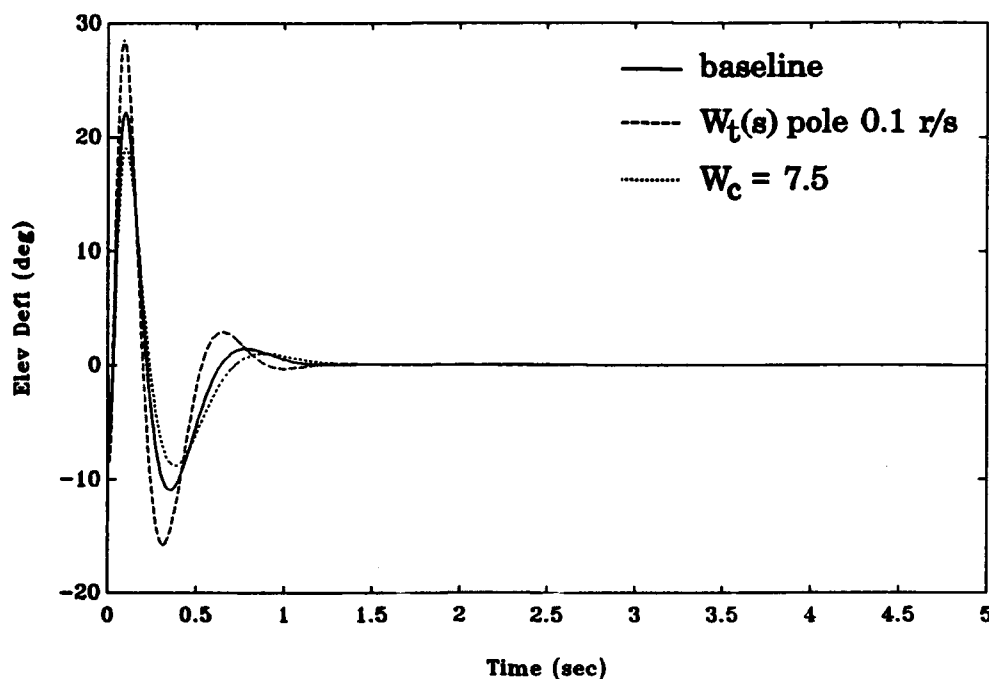


Figure 5-12. Elevator Deflection from  $\alpha(0) = 5$  deg, LO

The overall results of this section can be summarized as:

- i). All cases (out of about forty) stabilize the higher order model with the dc gain of  $W_A(s)$  as 20 dB.
- ii). All three cases in the response plots appear to be very good trackers and regulators, but the critical key is that this is without the noise corruption. The plot of  $K_b(s)S(s)$  shows that the noise will severely corrupt control usage, and more in the fastest response case. The magnitude of  $T(s)$  also shows unfavorable characteristics for noise attenuation.
- iii). The sensitivity transfer function magnitudes are extremely low at low frequencies, especially at the phugoid frequency.

iv). The robustness test on the additive uncertainty  $K_b(s)S(s)$  does not give any useful information since it is not passed, and the  $\infty$ -norm test on  $\|T_{cd}\Delta(s)\|$  being less than one is not applicable since  $\Delta(s)$  does not overbound the expected uncertainty. Thus, the recourse is to close the loop and check the higher order model's poles.

v). For increasing the break frequency of the  $W_i(s)$  pole, the complex phase and upper gain margins went to a peak for the pole located at 0.05 rad/sec, whereas the lower complex gain margin continually increased. With changing the value of  $W_c$  for a fixed  $W_i(s)$  pole location, the complex phase and lower gain margin decreased as  $W_c$  was raised.

vi). Raising  $W_c$  lowered the compensator magnitudes at high frequency and appeared to let the compensator cancel the zero pair in the plant to a lesser extent. Going to the higher frequency pole in  $W_i(s)$  increased the high frequency compensator magnitude and cancelled the complex zero pair better.

vii). Varying  $W_c$  shifted the whole loop shape curve up and down. Raising  $W_c$  lowered the magnitude of the curve at all frequencies.

viii). Increasing the frequency of the  $W_i(s)$  pole gives more high frequency noise passage to the plant output (from  $|T(j\omega)|$ ) and raising  $W_c$  gives less. At high frequency, the faster  $W_i(s)$  pole design yields less allowable multiplicative uncertainty and the increased control weighting case gives the most.

ix). For the magnitude of  $K_b(s)S(s)$ , moving the  $W_i(s)$  pole to higher

frequency gives less allowable plant additive uncertainty at high frequency. The allowable plant additive uncertainty is increased at high frequencies for raising  $W_c$ .

x). Using the faster pole in  $W_t(s)$  gives lower rise times and slightly more overshoot in the  $N_z$  step response. The higher value of  $W_c$  gives longer rise times and less overshoot of 1 G.

xi). The elevator deflection increased as the  $W_t(s)$  pole was moved to a higher frequency, and for the pole located at 0.1 rad/sec the deflection went past the 25 degree limit for the F-16. An increase in  $W_c$  gave less elevator deflection.

xii). The baseline  $H_\infty$  responses appear similar to the baseline case from the  $H_2$  tracking design, although the compensator magnitudes and loop shape are noticeably different.

This section has shown an  $H_\infty$  optimal design set up as a robust tracker. The resulting cases are all stabilizing for the higher order model, but the optimal  $H_\infty$  compensators have a "D" term in their state space. With concern over noise corruption since the compensators do not roll off, the next section is devoted to a suboptimal  $H_\infty$  compensator design using the baseline case from this section.

## **5.2 $H_\infty$ Sub-Optimal Examination (Central)**

The intent of this section is to augment the previous  $H_\infty$  comparison by examining an  $H_\infty$  suboptimal (central) controller. Reasons for using a suboptimal controller are typically grouped into two categories: numerical difficulties in computing the exact optimal  $\gamma$ , and undesirable characteristics of the  $H_\infty$  optimal compensator. The details of these problems for optimal  $H_\infty$  compensators will now be examined.

Computing the value of  $\gamma$  away from  $\gamma_0$  (with the central controller) is seldom difficult. Problems normally arise as  $\gamma_0$  is approached, and the specific difficulty depends on which of the suboptimal conditions below fails at optimal.

- i)  $H_x \in \text{dom}(\text{Ric})$  with  $X_\infty = \text{Ric}(H_x) \geq 0$
- ii)  $H_y \in \text{dom}(\text{Ric})$  with  $Y_\infty = \text{Ric}(H_y) \geq 0$
- iii)  $\rho(Y_\infty X_\infty) < \gamma^2$  (spectral radius condition)

These suboptimal requirements are explained in Chapter II and in [Li92]. The value of  $\gamma_0$  is the minimum  $\gamma$  such that one of the above conditions fails.

Usually the spectral radius condition, the third one, is equal to  $\gamma_0^2$  when  $\gamma = \gamma_0$ . The immediate problem created by this is in the second part of the equation for  $K_c$ , as it appears in Chapter II and repeated here:

$$K_c = (B_u^T X_\infty + D_{cu}^T C_c) (I - \gamma^2 Y_\infty X_\infty)^{-1}.$$

As an aside, recall that this comparison is for the central controller only, so the other problem created by the spectral radius constraint in the  $K_{cl}$  equation is insignificant. The point is that with  $\rho[Y_{\infty}(\gamma_0)X_{\infty}(\gamma_0)] = \gamma_0^2$ , the second part of  $K_c$  is now non-invertible. The "descriptor" method is used to circumvent this problem, and leads to a compensator of order one less than the plant [GLDKS91]. In this case, the optimal compensator typically has a nonzero "D" term in its state space description that gives  $K(s)$  nonzero gain at high frequency, and the resulting  $\bar{\sigma}(T_{\infty})$  looks like an all-pass filter with dc gain equal to  $\gamma_0$ . Not to ignore the first two conditions; these are not very common in determining  $\gamma_0$  but can lead to optimal compensators the same order as the plant. This can happen if  $X_{\infty}$  and  $Y_{\infty}$  are not positive semidefinite, but the spectral radius condition is satisfied. In all  $H_{\infty}$  cases that were run, none fell into this situation; i.e. all compensators dropped at  $\gamma_0$  to a rank one below the plant.

The undesirable characteristics of the true optimal compensator can be somewhat alleviated if  $\gamma$  is backed slightly away from  $\gamma_0$  therefore zeroing out the compensator's "D" term. The importance of this "D" term will be shown in magnitude and time response plots, and is linked to two important factors that are evident even before examining any plots. The first is the fact that a nonzero "D" term in the state space of  $K(s)$  is a direct feedthrough for any high frequency noise that could be attenuated with a strictly proper compensator, and the second comes from the difficulty in implementing a

controller with such large power requirements at high frequencies. Both of these problems can be relieved by backing off of  $\gamma_0$  and causing the  $H_\infty$  suboptimal compensator to start approaching the  $H_2$  optimal one (for  $Q(s) = 0$  only) [Rid91].

Now that some of the structure has been reviewed, a look at the robustness test and properties for  $H_\infty$  optimal versus suboptimal controllers is made. In the previous  $H_\infty$  design, a combination of the submultiplicative property for the  $\infty$ -norm and the SGT are shown to exploit the maximum robustness for the  $H_\infty$  optimal controller. What of this is lost as  $\gamma$  is backed away from  $\gamma_0$  though? The SGT holds no matter what norm is involved in finding a compensator since it involves only the  $\infty$ -norm of  $T_{cd}$  as  $\Delta(s)$  is wrapped around it. This is independent of how the compensator, that is inside of  $T_{cd}$ , is found. Yet the SGT still uses the  $\infty$ -norm of  $T_{cd}(s)\Delta(s)$  to prove stability of the closed-loop system to an allowable  $\|\Delta\|_\infty$ . The submultiplicative property also holds in the suboptimal case, but with a word of caution. In the  $H_\infty$  optimal designs, the value of  $\gamma$  is also  $\|T_{cd}\|_\infty$ . In the suboptimal case this is not necessarily true, but usually holds for values of  $\gamma$  near  $\gamma_0$ . In actuality,  $\|T_{cd}\|_\infty$  could be much less than  $\gamma$ . Even with this,  $\|T_{cd}\|_\infty$  can still be found and the SGT used.

The specific comparison used for magnitude and time response plots (for the lower order model) is the baseline case from the previous  $H_\infty$  optimal section with  $\gamma_0 = 1.7753$ , and a 10% suboptimal case with  $\gamma = 1.9528$ . The

use of the optimal  $K(s)$  is denoted by the solid lines in Figures 5-13 through 5-19, whereas the dashed line represents the 10% suboptimal case. The increase of  $\gamma$  by 10% is an exaggeration to allow easier explanation of the effects of raising  $\gamma$  in the plots. An increase in the 1 - 5% range seems more practical, but depends on the example and design specifications.

The values for  $\gamma$  and the margins in four cases are presented in Table 5-2. The boldface rows are the two cases that are shown in magnitude and time response plots. These cases are the baseline design of the previous section, where  $W_c = 5$ ,  $W_\Delta(s)$  has a dc gain of 20 dB with its zero at 1 rad/sec and pole at 0.1 rad/sec, and  $W_\ell(s)$  has dc gain of 40 dB and its pole at 0.05 rad/sec. The important point that Table 5-2 makes is that in every case of raising  $\gamma$ , the margins (both Bode and complex) decrease. Other than this

Table 5-2.  $H_\infty$  Suboptimal Examination Results, LO

$\gamma$	Bode Gain Margin (dB)	Bode Phase Margin (deg)	Complex Gain Margin (dB)	Complex Phase Margin (deg)
<b>1.7753 (opt)</b>	<b>-9.3, 10.8</b>	<b><math>\pm 39</math></b>	<b>-7.3, 9.0</b>	<b><math>\pm 38</math></b>
1.8108 (2%)	-9.1, 10.3	$\pm 38$	-7.2, 8.6	$\pm 37$
<b>1.9528 (10%)</b>	<b>-8.7, 10.0</b>	<b><math>\pm 35</math></b>	<b>-6.7, 7.5</b>	<b><math>\pm 34</math></b>
100.0	-6.7, 8.6	$\pm 24$	-4.6, 4.2	$\pm 24$

observation is the amount that they decrease, which is not very much for the lower percentages of increased  $\gamma$ . In going to the 2% suboptimal case, the margins are just below the optimal ones.

Turning to magnitude and time response plots, Figure 5-13 is the singular value plot of  $T_{ed}$ . This pictorially explains the "all-pass" feature of  $\bar{\sigma}(T_{ed})$  at optimal, where  $\bar{\sigma}(T_{ed}) = \gamma_o = \|T_{ed}\|_{\infty}$ . The 10% suboptimal case has  $\|T_{ed}\|_{\infty} = 1.9529$ , which is the value of  $\gamma$  for this suboptimal case. Again this does not have to be true. It is also seen in this figure that  $\|T_{ed}\|_{\infty}$  is not being minimized in the suboptimal case, so the allowable robustness (value of  $\|\Delta\|_{\infty}$ ) is not being maximized. Clearly the suboptimal case will have a finite 2-norm value for  $T_{ed}$ , whereas for the optimal case  $\|T_{ed}\|_2 = \infty$ . The

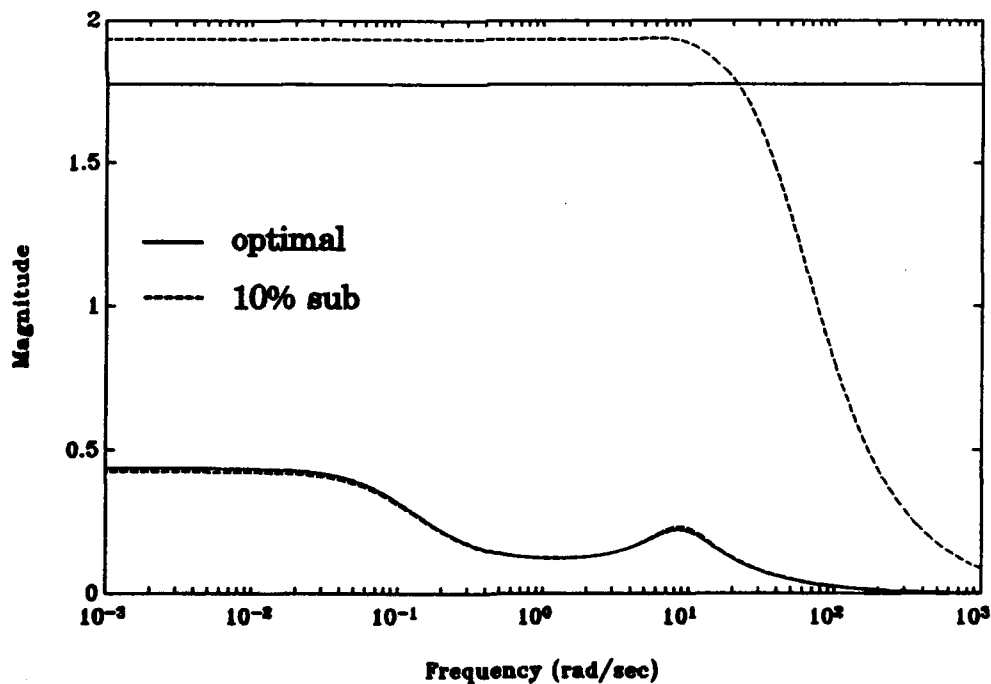


Figure 5-13. Singular Values of  $T_{ed}$ , LO



$H_\infty$  suboptimal solution shows a noticeable trend in approaching an  $H_2$  optimal solution with the decreasing magnitude at high frequency, where the integral calculation for the 2-norm is dominant.

The "D" term for the  $H_\infty$  optimal controller is the key to Figure 5-14. As mentioned previously, in all the  $H_\infty$  optimal cases examined the compensator drops rank to one below that of the plant and picks up the nonzero "D" term. The dashed line of the suboptimal compensator magnitude demonstrates the change to a full order compensator, with no direct energy feedthrough because of the roll off. The suboptimal case will attenuate more high frequency noise than the optimal case, with little difference in the low frequency magnitude.

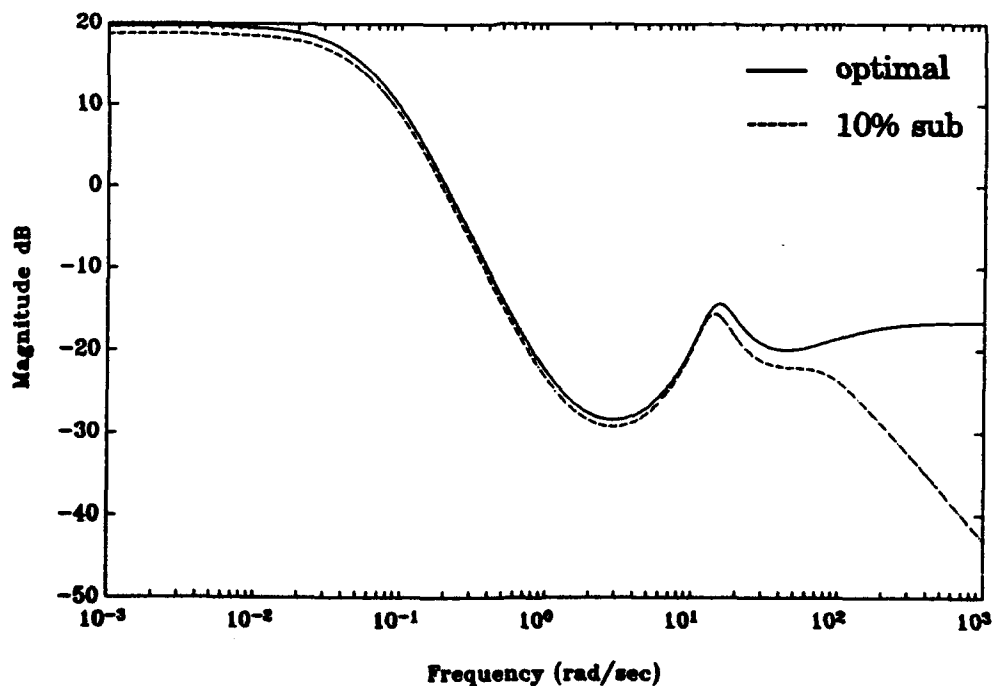


Figure 5-14. Feedback Compensator Magnitude

The loop shape is Figure 5-15 and again demonstrates a more favorable roll off for the suboptimal case. The suboptimal case has nearly the same high gain at low frequencies as the optimal case, and is very close to the magnitude of the optimal case at the frequency where the plant's complex zero is being countered.

The overall shape of the sensitivity magnitudes appear to be very close in Figure 5-16. The suboptimal case does show that the complex margins (that depend on the sensitivity transfer function magnitude) will be slightly decreased because of its higher magnitude peak, which correlates with the results of Table 5-2. Attenuation of low frequency noise will be basically the same for both cases.

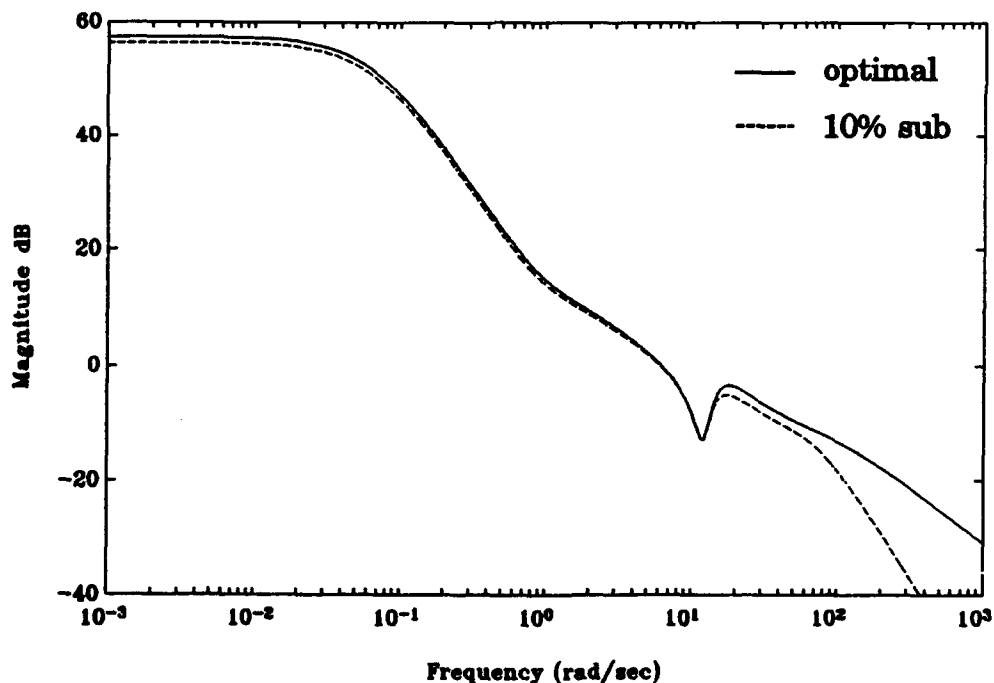


Figure 5-15. Magnitude of  $G(s)K_s(s)$ , LO

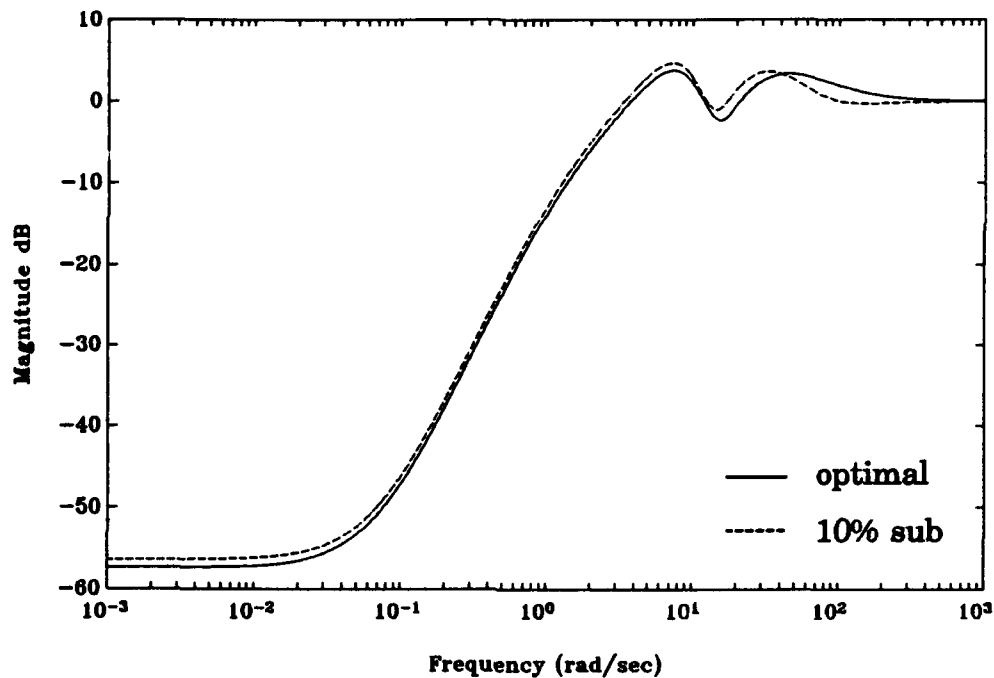


Figure 5-16. Sensitivity Magnitude, LO

A key magnitude plot in this comparison is the complimentary sensitivity, Figure 5-17. Not because of the slightly lower complex margins that will occur with the suboptimal case, but for the reason that the high frequency measurement noise will be attenuated much better by choosing  $\gamma$  larger than  $\gamma_0$ . The magnitude of  $T(s)$  also shows larger allowable multiplicative uncertainty at high frequencies in the suboptimal case.

The closed-loop transfer function in Figure 5-18 shows a preferable roll off. This would be a benefit if any high frequency noise came into the system with the commanded input, since the suboptimal case would attenuate this noise much better. The low frequency magnitudes appear to be identical.

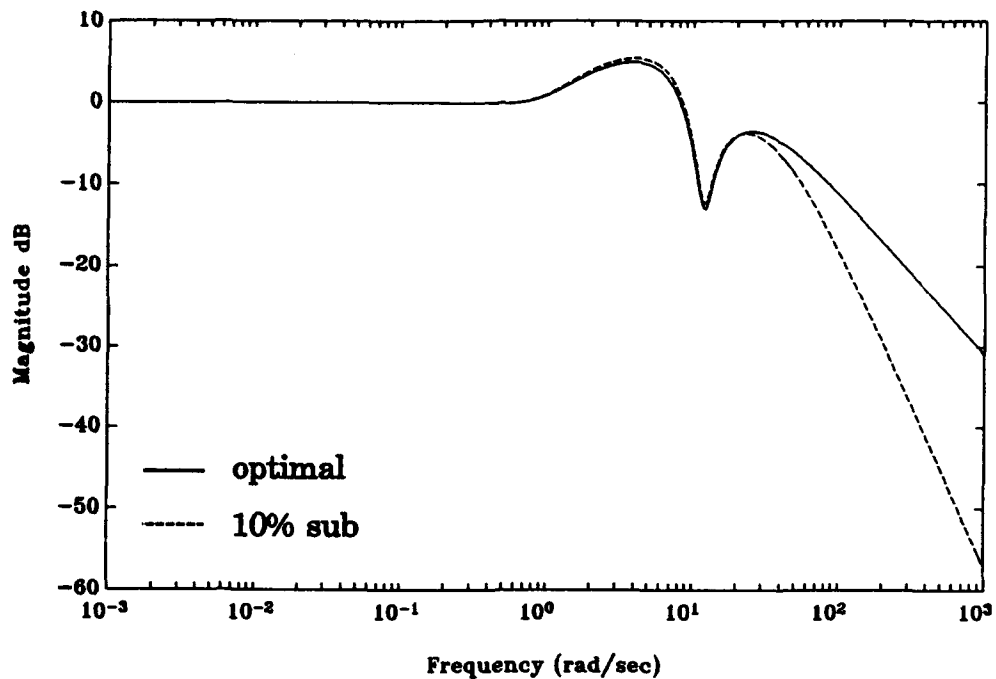


Figure 5-17. Complimentary Sensitivity Magnitude, LO

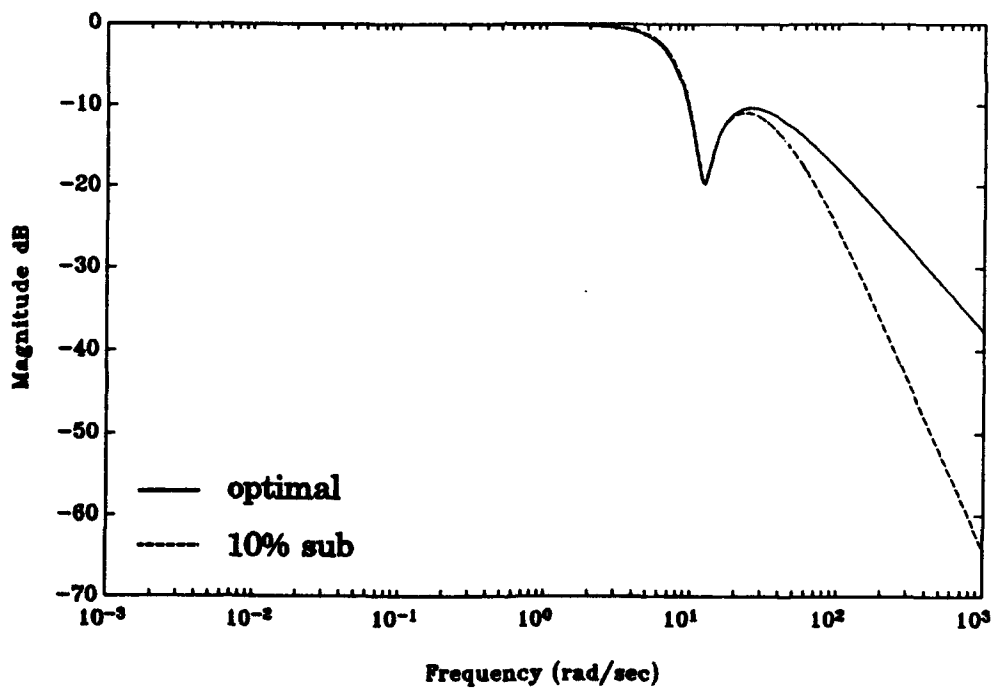


Figure 5-18. Closed-Loop Transfer Function Magnitude, LO

Figure 5-19 is the magnitude plot of  $K_b(s)S(s)$ . The first interesting fact to note is that the high frequency noise input to control usage is attenuated much more in the suboptimal case (from  $K_b(s)S(s)$  roll off). Another observation is that the allowable additive  $\|\Delta\|_\infty$  goes down barely in the suboptimal case (peak of  $K_b(s)S(s)$  is slightly larger in the suboptimal case), since  $\|T_{ed}\|_\infty$  is not being minimized here and is higher. In contrast, the allowable plant additive uncertainty increases at high frequencies for the suboptimal case, which is a direct result of the compensator roll off since the magnitude of  $S(s)$  will approach 0 dB at high frequency.

The step response for the lower order model at  $\gamma_0$  is Figure 5-20. Simulation noises are included as in the  $H_2$  chapter. The low frequency

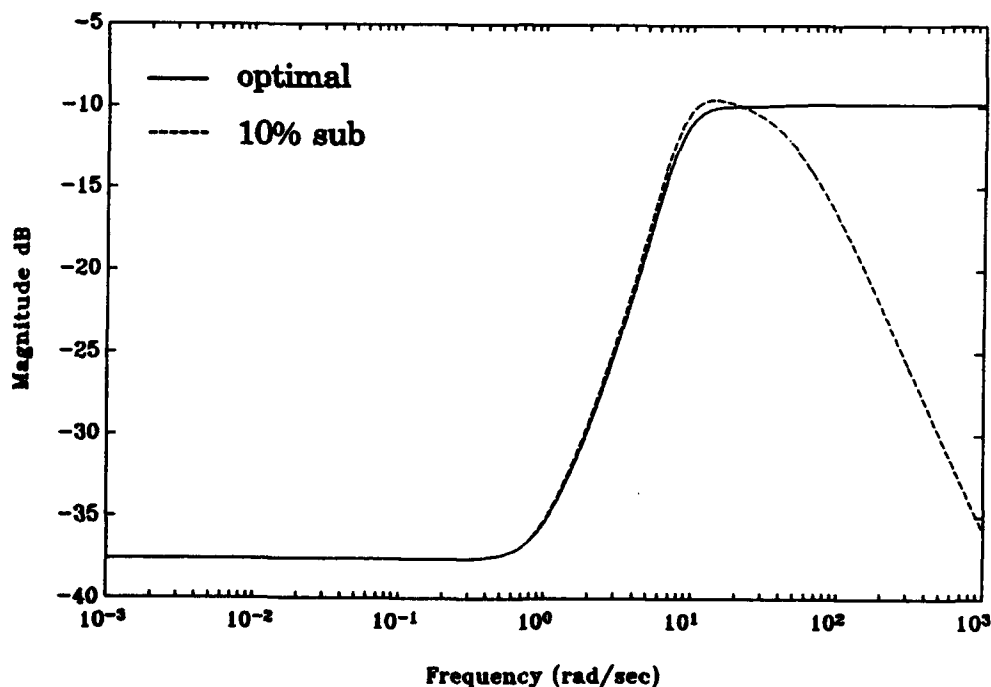


Figure 5-19. Magnitude of  $K_b(s)S(s)$ , LO

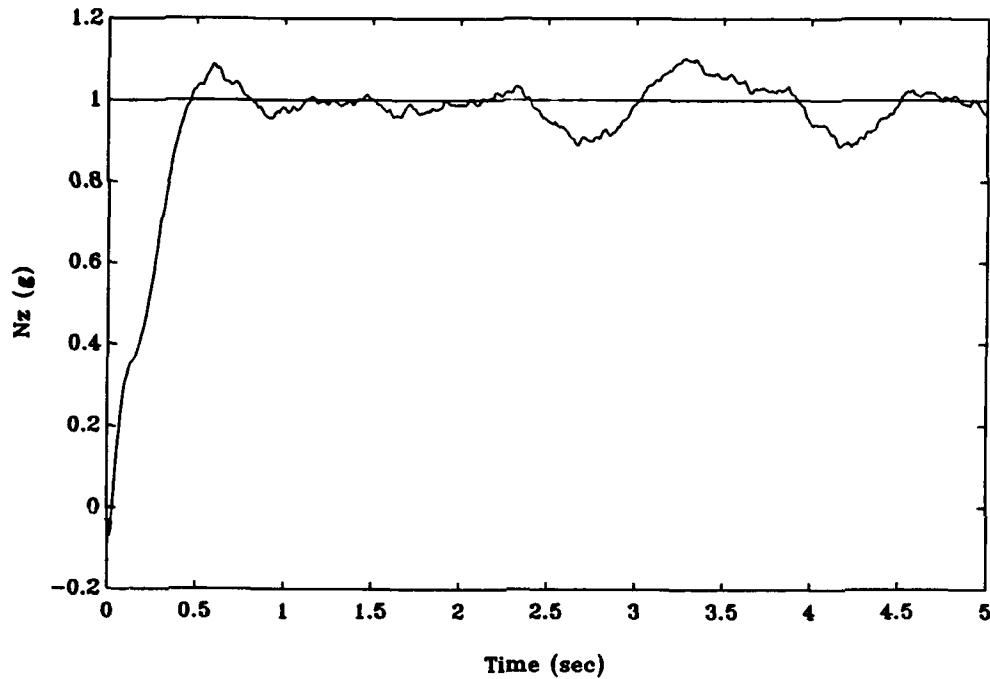


Figure 5-20.  $N_z$  from  $N_z$  Command Step, LO, Optimal

disturbance is from the combination of noises  $w_1$  and  $w_2$  that are not attenuated well by  $S(s)$  and  $T(s)$ , respectively, as in Equation (5.7).

$$y_g(s) = S(s)G(s)K_f(s)r(s) + S(s)G_{Td}w_1 + T(s)W_n w_2 \quad (5.7)$$

The high frequency noise is strictly due to  $w_2$  (see solid line in Figure 5-17).

The suboptimal comparison for the  $N_z$  step response is Figure 5-21. A large amount of the high frequency noise from the optimal case is attenuated by raising  $\gamma$ . This is from the steep roll off of  $T(s)$ ; see the dashed line in Figure 5-17. Overall, the step responses look very similar for the optimal and suboptimal cases, except for the smaller high frequency measurement noise content in the suboptimal case.

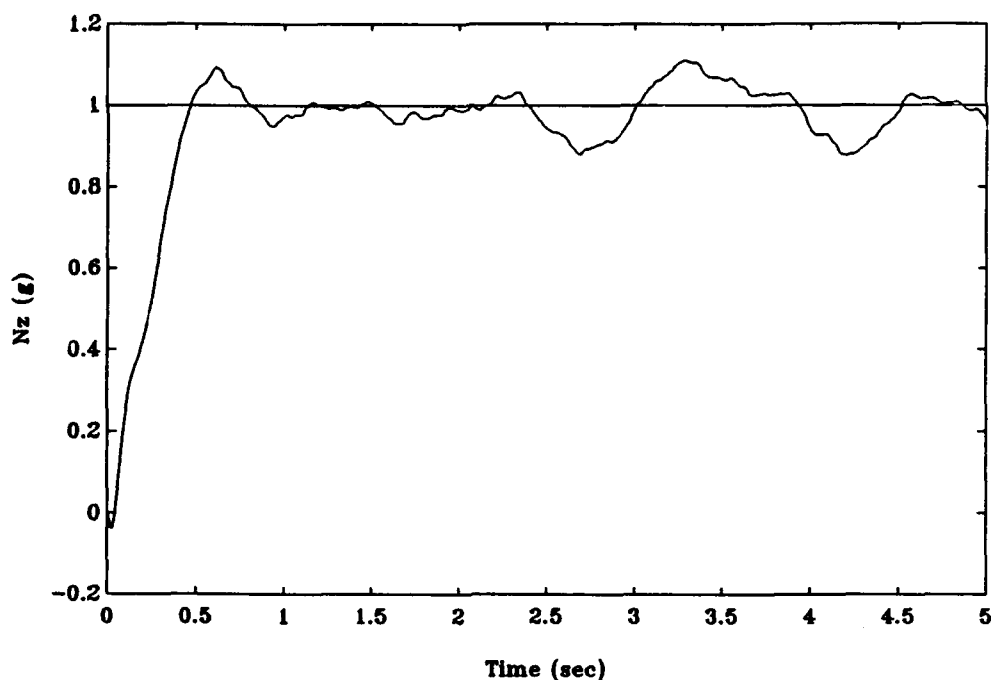


Figure 5-21.  $N_z$  for  $N_z$  Command Step, LO, 10% Suboptimal

Figure 5-22 is the control usage response for the step  $N_z$  command in the optimal case. Large amounts of mid to high frequency noise corrupt the system, as foreshadowed by the magnitude plot of  $K_b(s)S(s)$ , Figure 5-19.  $K_b(s)S(s)$  not rolling off (holds at -10 dB above 10 rad/sec) passes the mid to high range frequency noise directly to the control usage response.

In contrast, Figure 5-23 has obviously much less high frequency measurement noise than the optimal case. This is due to the roll off of  $K_b(s)S(s)$  above around 20 rad/sec in Figure 5-19. The noise that does get passed to control usage is the midrange band of  $K_b(s)S(s)$ , from around 10 to 20 rad/sec.

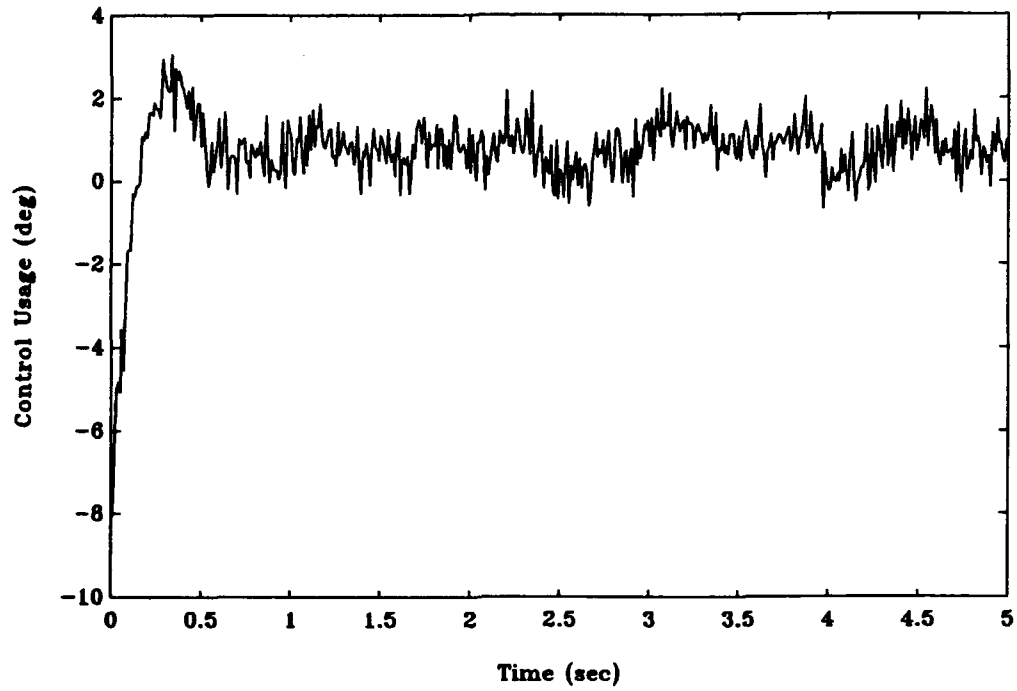


Figure 5-22. Control Usage (u) from  $N_2$  Command Step, LO, Optimal

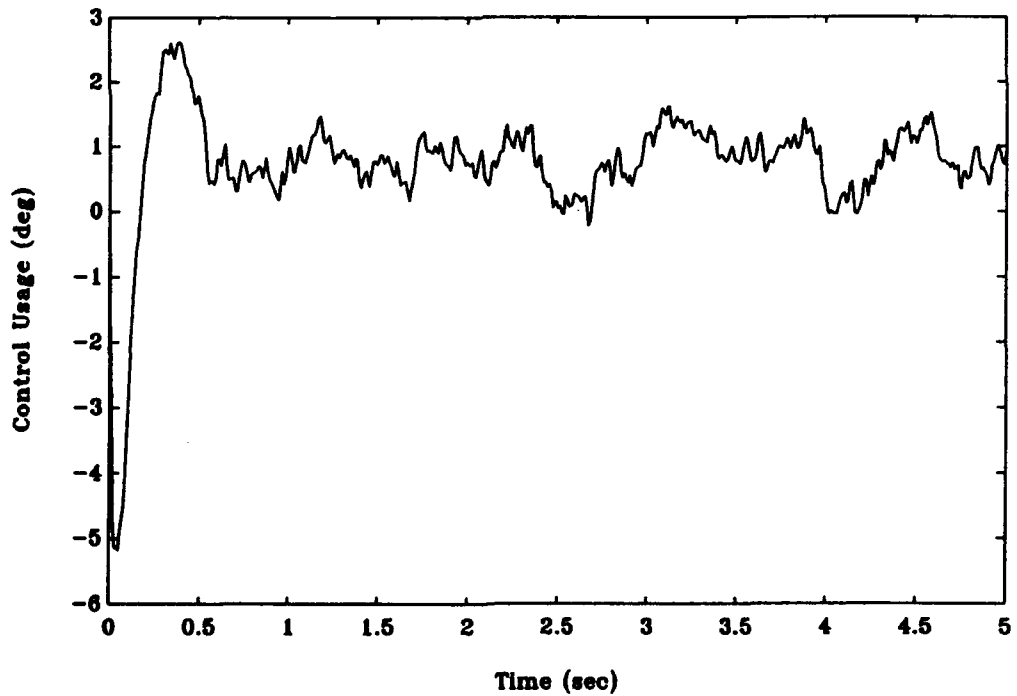


Figure 5-23. Control Usage (u) from  $N_2$  Step, LO, 10% Suboptimal



The conclusions of this look at a suboptimal  $H_\infty$  controller can be summarized as:

- i). The suboptimal controller is typically easier to compute.
- ii). The optimal compensator has a "D" term and is order one less than the plant (it is possible to not obey this, but not in any cases examined here), whereas the suboptimal case has no "D" term and is full order.
- iii). The "D" term in the  $H_\infty$  optimal compensator causes high frequency noise corruption of the plant output and control usage.
- iv).  $\|T_{ed}\|_\infty$  will rise with  $\gamma$  to a certain point, then  $\|T_{ed}\|_\infty$  will stay basically constant. In the  $\gamma = 100$  case,  $\|T_{ed}\|_\infty$  is around 2.9, whereas for the other three cases in Table 5-2,  $\|T_{ed}\|_\infty \approx \gamma$ .
- v). The allowable  $\|\Delta\|_\infty$  decreases as  $\gamma$  is raised above  $\gamma_0$ , but the allowable additive plant uncertainty is larger in the suboptimal case at high frequencies. The allowable multiplicative uncertainty is also larger at high frequencies for the suboptimal case.
- vi). Every margin decreases as  $\gamma$  increases, but a small change in moving  $\gamma$  away from  $\gamma_0$  does not change the margins very much. For this small change in  $\gamma$ , the noise corruption to the plant output and control usage can be cut down measurably.
- vii). All three of the suboptimal cases stabilize the higher order model.
- viii). If the measurement noise is taken as high frequency only, then backing off of  $\gamma_0$  will limit this high frequency noise and the low frequency

wind disturbance in this design, yet retain basically good tracking and regulation properties. The tradeoff is in the lowering of the allowable  $\|\Delta\|_\infty$  and margins.

As a summary of this chapter on  $H_\infty$  designs, it is first seen that all  $H_\infty$  compensators stabilize the higher order system. Also, the baseline optimal  $H_\infty$  case is both a good tracker and regulator, and a slightly better regulator than the  $H_2$  baseline tracking design. Furthermore, the optimal  $H_\infty$  baseline has larger complex phase and upper gain margins over the  $H_2$  baseline tracker. It is also evident that the  $\infty$ -norm robustness test fails in all  $H_\infty$  cases, yet the higher order system is stabilized. With a seemingly good design, the ignored topic of noise rejection is then addressed with the section on suboptimal  $H_\infty$  designs. A 2% suboptimal choice would clearly be an improvement over the optimal design because of sensor noise rejection. The reason for this improvement in noise rejection is due to the lack of a "D" term in the suboptimal compensator, and it is explained that a slight lowering of margins is the small disadvantage of the suboptimal case. With acceptable baseline  $H_2$  and  $H_\infty$  designs, the focus now turns to a method that gives a visible tradeoff of  $H_2$  and  $H_\infty$  objectives.

## VI. Mixed $H_2/H_\infty$ Design

### 6.1 $H_\infty$ Sensitivity and $H_2$ Tracker

The purpose of this chapter is to demonstrate a design procedure that gives a clear tradeoff between  $H_2$  and  $H_\infty$  design objectives. This nonconservative process, developed by Dr Brett Ridgely [Rid91], is the general mixed  $H_2/H_\infty$  methodology. With this approach, an  $H_2$  design on a selected transfer function  $T_{zw}$  competes with an  $H_\infty$  design on another transfer function  $T_{ed}$ . Of the two closed-loop norms,  $\|T_{ed}\|_\infty$  is designer fixed while  $\|T_{zw}\|_2$  is allowed to be reduced (mainly by a nonzero  $Q(s)$ ). For a mixed solution,  $\|T_{ed}\|_\infty$  must be above  $\gamma_0$  and  $\|T_{zw}\|_2$  greater than or equal to  $\alpha_0$ . The  $H_2$  part of the mixed setup will be the "performance" objective, including both tracking and noise rejection. Robustness will be the main feature of the  $H_\infty$  part, although tracking is not completely abandoned. From Chapter II, the general mixed solution is an admissible compensator  $K(s)$  that achieves:

$$\inf_{K \text{ adm}} \|T_{zw}\|_2, \text{ subject to the constraint } \|T_{ed}\|_\infty \leq \gamma$$

This methodology is different from the previous chapter that described "backing off" of  $\gamma_0$  to reach an  $H_\infty$  suboptimal central solution, which is the optimal  $H_2$  compensator at very large values of  $\gamma$ . The point is that at large  $\gamma$ 's the central  $H_\infty$  compensator is  $H_2$ -optimal for  $T_{ed}$ , not  $T_{zw}$ . With the mixed

The diagram illustrates a control system for a two-link manipulator. The reference input  $y_r$  is processed by a feedforward block  $K_f$  and a feedback block  $K_b$ . The system includes several disturbance inputs:  $w_1$  and  $d_1$  at the input, and  $d_2$  at the output. The control signal  $u$  is generated by the feedforward path and the feedback path. The system dynamics are represented by blocks  $B_g$ ,  $1/s$ ,  $A_g$ , and  $C_g$ . The output  $y_s$  is compared with the reference  $y_r$  to produce the error  $e_1$ . The error  $e_1$  is used to generate the control signal  $u$  through the feedforward path. The system also includes blocks  $W_{c2}$ ,  $W_{c\infty}$ ,  $W_d$ ,  $W_\Delta$ ,  $W_x$ ,  $W_n$ ,  $W_{t\infty}$ , and  $W_{t2}$ .

6-2

central  $H_\infty$  compensator plus two states. The setup for the mixed case is chosen as the combination of the  $H_2$  tracking design from Chapter IV and the  $H_\infty$  one from the previous chapter. The complete diagram for the mixed case is Figure 6-1. Common weight locations for the different parts have an additional subscript (2 or  $\infty$ ) to denote the differences. The design plant now consists of sixteen pieces, not nine as in the separate  $H_2$  and  $H_\infty$  designs. As a reference, the nine individual state space matrices of  $P(s)$  are Equations (4.15) through (4.17) for the  $H_2$  part, and Equations (5.2) through (5.4) for the  $H_\infty$  part. The individual state space matrices for the mixed  $P(s)$  are given in Equation (6.1).

$$P(s) = \left[ \begin{array}{c|ccc} A & B_d & B_w & B_u \\ \hline C_e & D_{ed} & D_{ew} & D_{eu} \\ C_z & D_{zd} & D_{zw} & D_{zu} \\ C_y & D_{yd} & D_{yw} & D_{yu} \end{array} \right] \quad (6.1)$$

$D_{ed}$ ,  $D_{zw}$ , and  $D_{yu}$  are assumed to be zero, while  $D_{zd}$  and  $D_{ew}$  are not used in problem formulation. Only the design plant's "A" matrix is examined here (not all sixteen pieces) since the complete description is very large and is the trivial combination of the equations mentioned previously. The mixed case design "A" matrix, Equation (6.2), shows the two additional weights on the  $H_2$  part that create the larger compensator. These are the  $A_d$  and  $A_\infty$  matrices

from the state space of the  $H_2$  tracking weight and the  $H_2$  wind disturbance weight, respectively. This creates the order difference between the  $H_2$  and  $H_\infty$  designs shown previously and the mixed case. Additional insight into this order difference is covered in Section 6.4. Now that the design setup is established, weight choices can be examined.

$$A_{\text{mix}} = \begin{bmatrix} A_g & \Gamma & 0 & 0 & 0 \\ 0 & A_d & 0 & 0 & 0 \\ B_{t2}C_g & 0 & A_{t2} & 0 & 0 \\ 0 & 0 & 0 & A_\Delta & 0 \\ B_{tm}C_g & 0 & 0 & B_{tm}C_\Delta & A_{tm} \end{bmatrix} \quad (6.2)$$

## **6.2 $H_2/H_\infty$ Weight Selection**

Again, the weight locations and types (dynamic versus scalar) are identical to the individual  $H_2$  tracking and  $H_\infty$  designs. The  $H_2$  choices are taken to be the "baseline" case described in the tracking design. To repeat, this is where the tracking weight has a dc gain of 50 dB and a pole at 0.1 rad/sec. The wind disturbance model is the same as described in Chapter III, and the values of  $W_{e2}$  and  $W_z$  are 20 and 1, respectively. The tracking necessity, along with noise rejection, is the basis for the  $H_2$  part. The  $H_\infty$  setup in this application is created as a type of robustness constraint on the sensitivity transfer function magnitude and the plant additive uncertainty. The sensitivity magnitude is

weighted to have small gain at low frequencies, and a minimal infinity norm. Small gain at low frequencies is to help reject possible disturbances at the plant output, whereas a small  $\|S\|_{\infty}$  is to maximize the complex margins that depend on the sensitivity magnitude peak. The tracking weight is chosen with a dc gain of 12 dB, a zero at 3 rad/sec, and poles at 0.1 rad/sec and 1000 rad/sec. A dc gain of 41.9 dB is used for the  $W_{\Delta}(s)$  weight, with a zero at 3 rad/sec and a pole at 0.1 rad/sec. The constant 0.6024 is chosen for  $W_{c\infty}$ . These seemingly strange choices can be explained upon examining the transfer function matrix  $T_{ed}$ , repeated here for convenience.

$$T_{ed} = \begin{bmatrix} W_{t\infty}(s)(S(s)G(s)K_f(s)-1) & W_{t\infty}(s)S(s)W_{\Delta}(s) \\ W_{c\infty}K_f(s)S(s) & W_{c\infty}K_b(s)S(s)W_{\Delta}(s) \end{bmatrix}$$

The objective is to weight the right column of  $T_{ed}$  as a robustness measure, but the left column also depends on these weights. A minor inconvenience in selecting weights is the necessity for  $W_{\Delta}(s)$  to have a "D" term, and  $W_{t\infty}$  to roll off. The double pole/zero combination on the sensitivity transfer function in  $T_{ed}(1,2)$  is based on the sensitivity plots from previous designs. This double pole/zero combination has to be chosen if the sensitivity magnitude needs to be small at low frequencies and  $\|S\|_{\infty}$  is to be minimized. The pole/zero combination is split between the two dynamic  $H_{\infty}$  weights because  $W_{\Delta}(s)$  also weights the plant additive uncertainty in  $T_{ed}(2,2)$ .  $W_{c\infty}$  is taken to be the scalar 0.6024 since it is combined with the  $W_{\Delta}(s)$  weight, effectively

giving a high frequency weight of 8 dB. Remember the low frequency plant additive uncertainty will approach the inverse of the low frequency plant magnitude (i.e. -37.5 dB) for large compensator gains in this region. So even though the low frequency weight on  $K_b(s)S(s)$  is not 8 dB, as long as the combined weight of  $W_\Delta(s)$  and  $W_\infty$  does not reach the 37.5 dB value, this will not interfere with the sensitivity constraint.

As an aside, the proper way to weight robustness would be with a design on the feedback compensator only, unlike what is done here. The reason to use the feedback compensator is that robustness, and stability, depend only on  $K_b(s)$ . The problem with this setup is that the necessity of  $D_{yd}D_{yd}^T$  being full rank is not met in the mixed case, with the 1 DOF controller. This condition in the mixed case is explained in Chapter II. In subsequent discussions with Ridgely, this problem has been explained as not creating conflicts in the solution to the mixed problem. As a result, an ongoing investigation into setting up the  $H_\infty$  part of the mixed case as a 1 DOF constraint on robustness is being done by the author. The difficulty in this is that solutions to this mixed case can easily take over a week to find (for full order cases). This leads to the need for an explanation of the actual solution to the mixed  $H_2/H_\infty$  problem.

### **6.3 Mixed $H_2/H_\infty$ Solution**

This section is an overview from [Fox71], [RMV92], and



[Rid91,124-129]. It is not intended to fully describe all the details of the numerical solution used in this mixed  $H_2/H_\infty$  process. The solution used in this general mixed  $H_2/H_\infty$  problem is that utilized by Ridgely, and is called the Davidon-Fletcher-Powell (DFP) algorithm, a numerical search routine. The actual DFP process is explained in [Fox71,75,104-109], and as it pertains to the mixed problem in the other two stated references. First, the background of the algorithm is discussed, followed by an explanation of its use in the mixed  $H_2/H_\infty$  problem.

The DFP numerical solution is necessary to solve the mixed problem since a closed-form solution is not available; recall the discussion on the seven nonlinear coupled necessary conditions. A key advantage of using DFP is that it is a quadratically convergent first order method that does not require calculation of the second partials of the function being minimized. The second partials for the mixed problem turn out to be fourth order tensors that require very large amounts of computer memory and therefore slow down execution times [Rid91]. DFP does not calculate these second partials, only an estimate of these that gets improved with each iteration. The function being minimized in the mixed  $H_2/H_\infty$  problem is

$$J_\mu(A_c, B_c, C_c) = (1-\mu) \text{tr}[Q_2 \tilde{C}_2^T \tilde{C}_2] + \mu \text{tr}[Q_\infty \tilde{C}_\infty^T \tilde{C}_\infty] \quad (6.3)$$

subject to

$$\tilde{A} Q_2 + Q_2 \tilde{A}^T + \tilde{B}_\infty \tilde{B}_\infty^T = 0$$

and

$$\bar{A}Q_{\infty} + Q_{\infty}\bar{A}^T + \gamma^{-2}Q_{\infty}\bar{C}_c^T\bar{C}_cQ_{\infty} + \bar{B}_d\bar{B}_d^T = 0$$

The DFP flow chart, Figure 6-2, will have  $F = J_{\mu}$  for the mixed solution performance index.

The initial  $X_0$  in Figure 6-2 is a column vector of unknown variables. This column vector represents the  $A_c$ ,  $B_c$ , and  $C_c$  matrices for the mixed problem. The  $S$  matrix is the direction that the current guess for  $X$  should

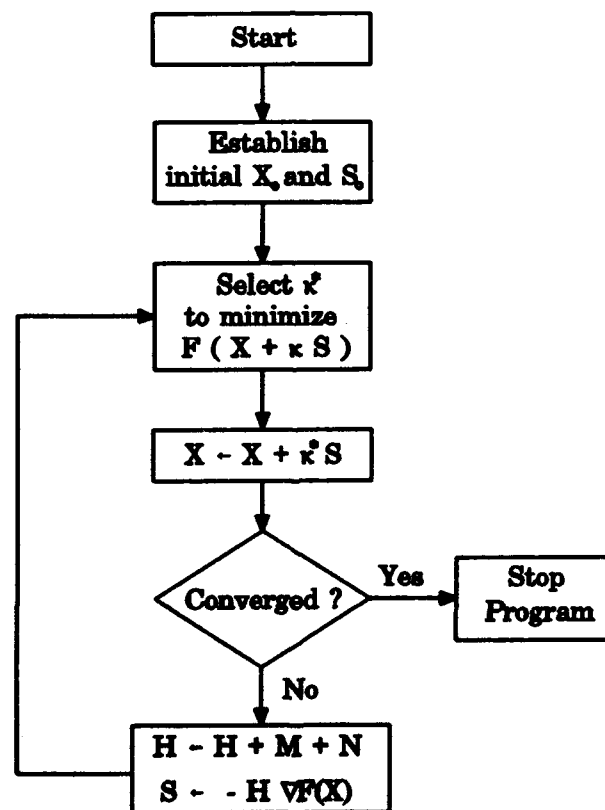


Figure 6-2. Flow Chart for DFP

take to minimize  $F(X)$ ; the initial  $S_0$  does not have to be given to the program but is calculated internally.  $\nabla F(X)$  is the column vector of partial derivatives of the Lagrangian  $\mathcal{L}_\mu$ , as given in [Rid91,114-117]. These partials are with respect to the  $A_c$ ,  $B_c$ , and  $C_c$  matrices for the mixed  $H_2/H_\infty$  problem. Again, DFP differs from a second order method in that the inverse of the second derivative matrix ( $J^{-1}$ ) is replaced by an estimate. This estimate is denoted by  $H$ , and will be a symmetric positive definite matrix. A typical second order method's  $S$ ,  $S = -J^{-1} \nabla F(X)$ , is now represented by  $S = -H \nabla F(X)$  in DFP. Returning to Figure 6-2,  $\kappa$  is the length of the step in the  $S$  direction. Note that  $\kappa$  is used here instead of  $\alpha$ , as in [Fox71], to not conflict with previously defined  $\alpha$  variables in this thesis. The remaining terms in Figure 6-2 are explained in the DFP procedure.

The DFP iteration method follows these steps:

- 1)  $X_0$  is given to the algorithm as compensator matrices  $A_c$ ,  $B_c$ , and  $C_c$ . The gradient,  $\nabla F(X)$ , is then found from this input compensator. Note that the input compensator must satisfy the  $\infty$ -norm constraint on  $T_{\infty}$ , and be stabilizing. The initial guess for  $H$  is the identity matrix; therefore,  $S_0$  is the negative of the gradient when  $X_0$  is used.
- 2) Following this start for DFP, the  $\kappa_q^*$  value that minimizes  $F(X_q + \kappa_q S_q)$  is found through a one-dimensional search, as explained in [Rid91,127]. Next, a new  $X$  is given by  $X_{q+1} = X_q + \kappa_q^* S_q$ , and convergence is checked. The program follows to Step 3 if convergence is not found.

3) A new H is computed from  $H_{q+1} = H_q + M_q + N_q$ , where [Fox71,105] gives

$$M_q = \kappa_q \frac{S_q S_q^T}{S_q^T Y_q}$$

$$N_q = - \frac{(H_q Y_q)(H_q Y_q)^T}{Y_q^T H_q Y_q}$$

$$Y_q \equiv \nabla F(X_{q+1}) - \nabla F(X_q)$$

4) Next a new S is found through  $S_{q+1} = -H_{q+1} \nabla F(X_{q+1})$  and the program returns to Step 2. This updated S and X give a new  $\kappa^*$  value, and the process continues until convergence. The stop criterion depends on the user-specified value of  $\epsilon$  in

$$\frac{\nabla F_q^T H_q \nabla F_q}{|F(X_q)|} < \epsilon$$

This  $\epsilon$  value is set to  $10^{-6}$  in all mixed runs.

Possible problems in the DFP solution that pertain to the mixed application are covered in [Rid91,128-129]. The actual approach to obtain the mixed compensator begins with the designer choosing a value of  $\gamma$  between  $\gamma_0$  and  $\gamma_2$ . To repeat, the  $\gamma_0$  value is the optimal  $\|T_{cd}\|_\infty$ , and  $\gamma_2$  is the value of  $\|T_{cd}\|_\infty$  when using the optimal  $H_2$  compensator for  $T_{zw}$ . The  $H_\infty$  central controller is then found at this value of  $\gamma$ , so that it can be used for the initial

guess  $X_0$  in DFP. The problem of size difference with the initial compensator will be addressed in the next section. A  $\gamma$  close to  $\gamma_0$  is preferred since this would serve as an initial guess for higher values of  $\gamma$ , but not lower values. The variable  $\mu$ , shown earlier in the performance index Equation (6.3), is now decreased until  $\|T_{zw}\|_2$  stops changing. The range of  $\mu$  is from near one to around zero; actually, in this work  $\mu$  is not taken below the 0.0001 value. Other convergence checks for the mixed solution are discussed in [Wel91,5-5]. This iteration technique of raising  $\gamma$ , then driving  $\mu$  down towards zero, can be continued up to  $\gamma_2$ . At  $\gamma_2$  and above, the mixed compensator is equivalent to the  $H_2$  optimal compensator for  $T_{zw}$ .

#### **6.4 DFP Start Compensator**

The  $X_0$  that is discussed in the previous section, and shown in Figure 6-2, is again the initial compensator guess ( $A_c$ ,  $B_c$ , and  $C_c$ ) needed to start DFP. The problem associated with using this central  $H_\infty$  compensator as the initial guess is that it is full order for the  $H_\infty$  design, not the mixed design. An  $X_0$  of the central  $H_\infty$  compensator would be the exact solution for the suboptimal mixed problem at  $\mu = 1$  with scalar weights in the design. As shown in the dynamically weighted "A" design matrix, Equation (6.2), the full order "A" matrix for the  $H_\infty$  separate design is not compatible with this initial guess. For the weights explained earlier, this central  $H_\infty$  compensator is two states less than the nine states required for the full order mixed guess. So the

seemingly easy task of using the central  $H_\infty$  controller as the initial guess turns out to create a somewhat difficult problem.

The approach taken to increase the size of the initial guess compensator is credited to Wells [Wel91]. This follows the (J,Q)-parameterization of  $K(s)$  that is discussed in Chapter II. Looking at Figure 6-3, the transfer function matrix  $J(s)$  (not to be confused with a performance index) is completely known for the  $H_\infty$  suboptimal compensator.

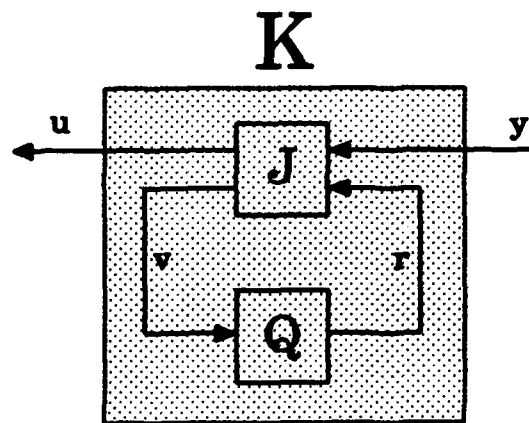


Figure 6-3. (J,Q)-Parameterization

The task then turns to finding a  $Q(s)$  that is admissible and gives the higher order  $K(s)$ . Only a two state increase is necessary for the initial guess, so the objective is to find a second order admissible  $Q(s)$  (assuming no pole/zero cancellations). The admissibility of  $Q(s)$  is that it must satisfy the  $\gamma$  constraint, i.e.  $\|Q\|_\infty \leq \gamma$ , and that it is proper and stable.

The actual  $Q(s)$  can be "backed out" of  $K(s)$  since  $J(s)$  is completely known. Note that if  $Q(s)$  is found from  $J(s)$  and  $K(s)$  for a central  $H_\infty$  suboptimal  $\gamma$  value, it will be identically zero and  $K(s)$  will be equal to  $J_{uy}(s)$ . The development in [Rid91,151-154] is the basis for finding  $Q(s)$  in this manner, so that it could then be combined with  $J(s)$  (on Pro-Matlab™) to yield the higher order start compensator. The question that now arises is how to get a nonzero  $Q(s)$  from the central suboptimal  $H_\infty$ 's  $J(s)$  and  $K(s)$ . The straightforward method used is the same as that of [Wel91] and involves modifying  $K(s)$  slightly to give this  $Q(s)$ . In this study, the central  $H_\infty$  compensator was modified typically in the fourth decimal place of the first term in " $C_c$ ". In almost every case the resulting  $Q(s)$  had order well above the two states necessary. Now  $Q(s)$  can be reduced to second order and wrapped around  $J(s)$  to give the needed  $K(s)$ . Stability and the  $\gamma$  constraint on  $Q(s)$  need to be checked in the process. A program using a Schur model reduction method, similar to the Pro-Matlab™ one used by [Wel91], is utilized to reduce  $Q(s)$ . The resulting  $K(s)$  is in essence just the central  $H_\infty$  compensator from before, but a nearly nonminimal realization.

In summary, the ease of being able to just use a reduced order guess ( $H_\infty$  suboptimal central compensator) for the mixed case was not possible for this dynamically weighted example. The somewhat lengthy process of creating the higher order compensator by changing  $K(s)$  appears to be the only process that worked regularly for [Wel91], and also worked in this study.

## 6.5 Mixed $H_2/H_\infty$ Results

Values for  $\|T_{ed}\|_\infty$  and  $\|T_{zw}\|_2$  are shown in Table 6-1 for six cases.

These six rows begin with the optimal value of  $\gamma_o = 1.064$  for the  $H_\infty$  part of the mixed case. The bottom row's  $\gamma$ ,  $\gamma_2 = 10.782$ , is the  $\|T_{ed}\|_\infty$  that results from using the optimal  $H_2$  compensator ( $K_{2opt}$ ). As defined earlier, the

Table 6-1. Mixed  $H_2/H_\infty$  Results, LO

$\ T_{ed}\ _\infty$ Weighted ( $\gamma$ )	$\ T_{zw}\ _2$ Weighted	Bode Gain Margin (dB)	Bode Phase Margin (deg)	Complex Gain Margin (dB)	Complex Phase Margin (deg)
1.064	$\infty$	-8.1, 12.0	$\pm 42$	-6.8, 10.5	$\pm 41$
1.1	15.6686	-7.9, 11.9	$\pm 41$	-6.6, 10.0	$\pm 40$
1.25	15.6288	-9.0, 9.4	$\pm 37$	-7.1, 8.2	$\pm 36$
1.35	15.6250	-9.5, 9.9	$\pm 35$	-7.2, 7.5	$\pm 34$
5.0	15.6159	-11.3, 9.4	$\pm 36$	-8.2, 6.9	$\pm 36$
10.782	15.6141	-11.1, 10.1	$\pm 36$	-8.1, 7.1	$\pm 35$

optimal  $\|T_{zw}\|_2$  is  $\alpha_o$  and has a 15.6141 value. The middle four rows of Table 6-1 represent actual mixed case results using  $\gamma$  values of 1.1, 1.25, 1.35, and 5. The second column is the value of  $\|T_{zw}\|_2$  that results from using the same compensator that gives the corresponding  $\gamma$  values on the left. The top row, representing the  $H_\infty$  optimal solution, yields a theoretical  $\|T_{zw}\|_2$



of infinity because of the "D" term in its compensator. On the bottom row is the optimal  $\|T_{zw}\|_2$  for the  $H_2$  part of the mixed case, and yields the smallest value that  $\|T_{zw}\|_2$  can possibly have,  $\alpha_0$ . Between these two optimal solutions for the separate parts are the four mixed cases that show the decreasing value of  $\|T_{zw}\|_2$  as  $\gamma$  increases from  $\gamma_0$  to  $\gamma_2$ . This  $\|T_{zw}\|_2$  versus  $\gamma$  curve monotonically decreases as  $\gamma$  increases [Rid91,123]. The values of  $\gamma_0$ ,  $\gamma_2$ , and  $\alpha_0$  represent performance limits for the mixed case solution, and will be shown in the upcoming Figure 6-4. The  $\|T_{cd}\|_\infty$  and  $\|T_{zw}\|_2$  cannot be lower than  $\gamma_0$  or  $\alpha_0$ , respectively. Raising  $\gamma$  above  $\gamma_2$  yields no beneficial compensators since the mixed solution is already converged to the  $H_2$  compensator at  $\gamma_2$ . Complex margins in Table 6-1 show the large upper gain and phase margins for the  $\gamma_0$  case. These are a direct result of the  $H_\infty$  weight on the sensitivity transfer function. As  $\gamma$  is raised, the complex phase follows a predictable trend to a value of 34 degrees at  $\gamma = 1.35$  for the first four rows. The change in the last two rows is from the dependency of the complex phase margin shifting to the peak of  $T(s)$ , whereas the first four rows depend on the peak of  $S(s)$ . The upper complex gain margin follows a similar decreasing trend, although there is a slight change from  $\gamma = 5$  to  $\gamma_2$ . The author is not satisfied that the  $\gamma = 5$  case fully converged to the mixed solution as in the  $\gamma = 1.1, 1.25$ , and  $1.35$  cases. This opinion is based on the plot of  $T_{cd}$  versus frequency that did not have a flat low frequency magnitude like the others. Returning to Table 6-1, the lower complex gain margin generally

increases as  $\gamma$  rises, although it is not specifically weighted in the  $H_\infty$  or  $H_2$  design parts.

Magnitude and time response plots for this mixed design will show the optimal  $H_\infty$  results represented by a solid line, and the optimal  $H_2$  results with a dot-dash line. The other two lines will be the mixed compensator results for  $\gamma = 1.1$  and 1.25, denoted with a dashed and dotted line, respectively. These two mixed cases are the  $\gamma$  values closest to  $\gamma_0$ ; the two asterisks furthest left in Figure 6-4. The "best" area for a compromise of the competing  $H_2$  and  $H_\infty$  objectives, i.e. both  $\|T_{zw}\|_2$  and  $\|T_{ed}\|_\infty$  small, is in the bottom left corner of Figure 6-4 (within the dashed lines of the optimal constraints).

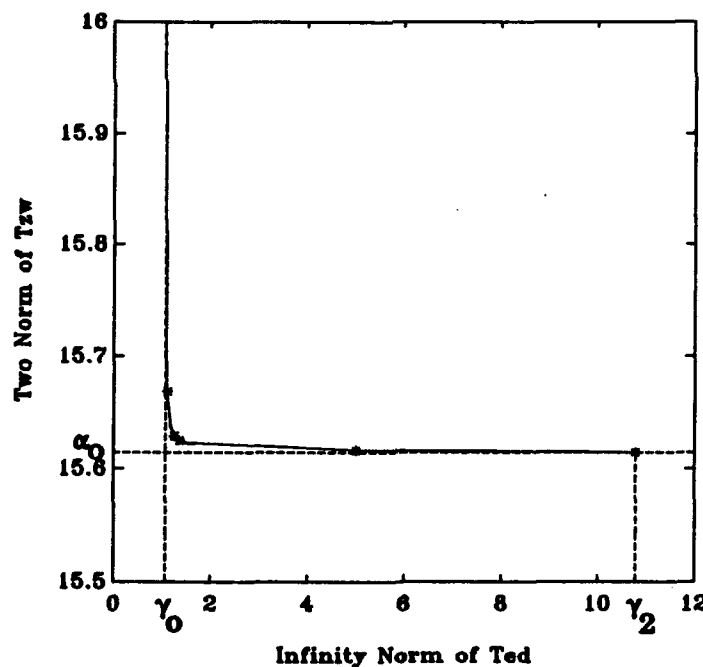


Figure 6-4.  $\|T_{zw}\|_2$  Versus  $\|T_{ed}\|_\infty$  for Mixed Case

The first magnitude plot is Figure 6-5 which represents the maximum singular value of  $T_{ed}$  for the four  $\gamma$  values. The minimum singular value (there are two singular values since  $T_{ed}$  is a  $2 \times 2$  transfer function matrix) is not included since it is not being constrained and only complicates the plot. The value of  $\gamma$  can be seen on the magnitude scale as it rises from  $\gamma_0$  to  $\gamma_2$ . The line for  $\gamma = 1.25$  clearly starts conforming to the  $\gamma_2$  line. In essence, the lines will converge to the  $\gamma_2$  one as  $\gamma$  is increased, although in this example there is no reason to increase  $\gamma$  above around a 1.35 value. After this  $\gamma$  value is reached, only  $\|T_{ed}\|_{\infty}$  really rises and  $\|T_{zw}\|_2$  barely falls anymore.

The maximum singular value plot for  $T_{zw}$  is shown as Figure 6-6. The solid line for  $\gamma_0$ , or optimal  $\|T_{ed}\|_{\infty}$ , definitely shows that more noise (from

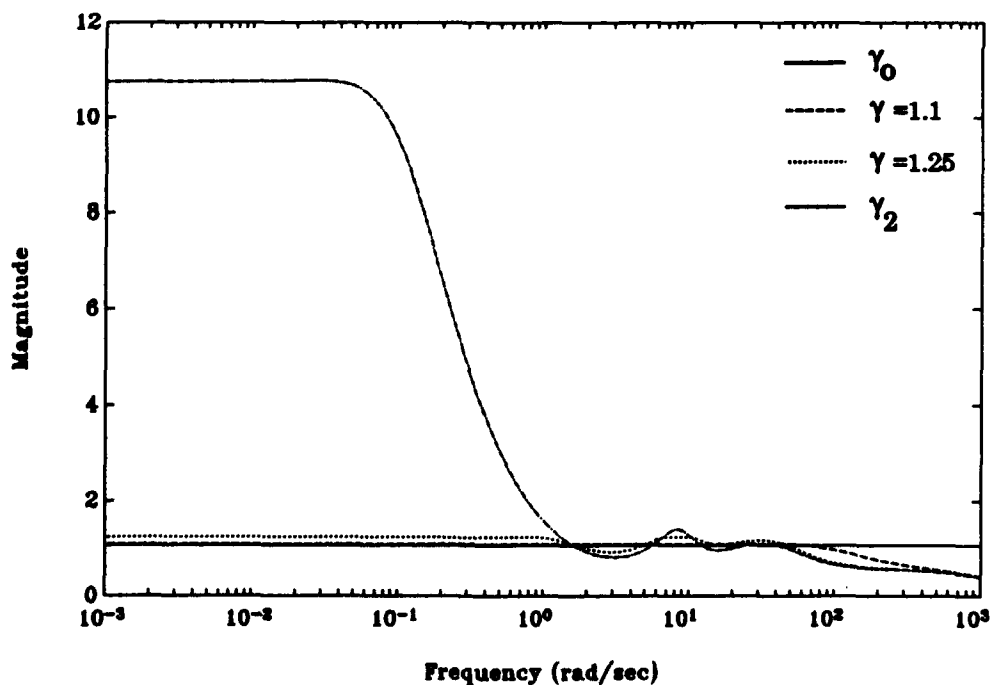


Figure 6-5. Maximum Singular Values of  $T_{ed}$ , LO

w) will pass through to the chosen outputs (z) in the design; remember this includes weights. Also evident is the magnitude for the  $\gamma_0$  curve in the high frequency area; this creates the infinite  $\|T_{zw}\|_2$ , since it does not roll off. Raising  $\gamma$  slightly above  $\gamma_0$  shows the  $\gamma = 1.1$  and  $\gamma = 1.25$  lines converge almost exactly to the  $\gamma_2$  (or  $H_2$  optimal) curve's maximum singular value. The high frequency lines for these three  $\gamma$  cases are literally matched where the frequency integral will have the most importance. This graphically gives insight into why the values of  $\|T_{zw}\|_2$  are so close for the  $\gamma = 1.1, 1.25$ , and  $\gamma_2$  cases; although  $\|T_{zw}\|_2$  also depends on the other two singular values. The other singular values of  $T_{zw}$  ( $T_{zw}$  is a 3 x 3 transfer function matrix) are not shown because of plot complexity. The low frequency difference

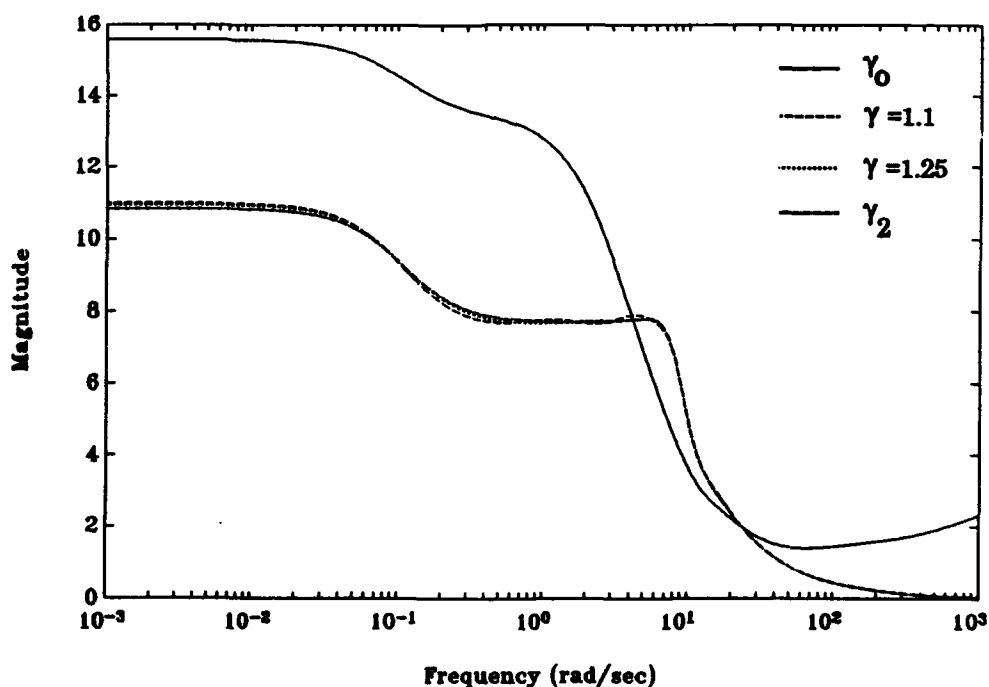


Figure 6-6. Maximum Singular Values of  $T_{zw}$ , LO

will not have as much of an impact since the integral over this frequency range is not very significant to the overall  $\|T_{zw}\|_2$  value.

Compensator magnitude plots are Figures 6-7 and 6-8 for the feedforward and feedback compensators, respectively. One observation with these is that the magnitude plots are not as similar as in the past 2 DOF designs. Backing off of  $\gamma_0$  creates significant changes in the magnitudes above 1 rad/sec. Remember that  $Q(s)$  is nonzero now, and that the feedback compensator is heavily weighted by the  $H_\infty$  part of the problem. Low frequency magnitudes can be seen to drop as  $\gamma$  approaches  $\gamma_2$ . The point here is that tracking actually is better as the low frequency magnitude falls, but recall that the closed-loop transfer function for the 2 DOF setup is  $S(s)G(s)K_f(s)$ .

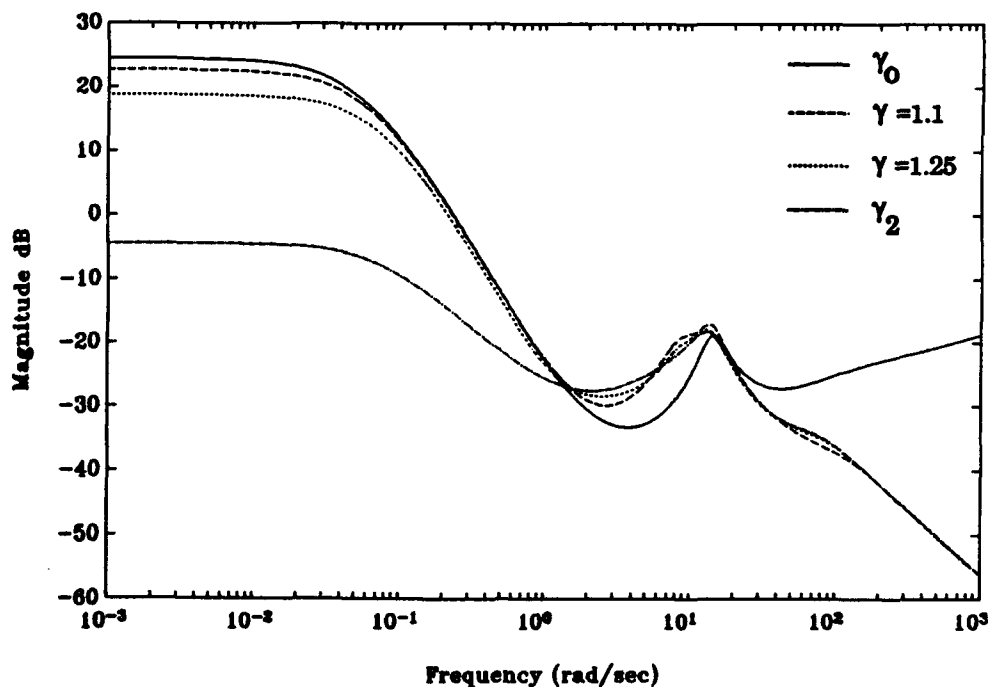


Figure 6-7. Feedforward Compensator Magnitude

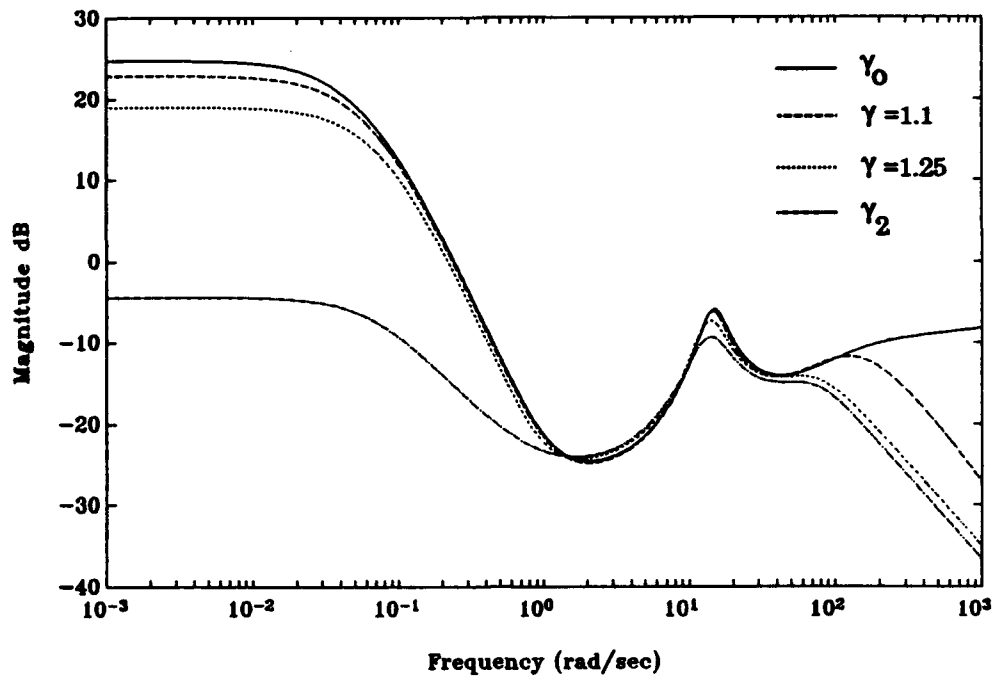


Figure 6-8. Feedback Compensator Magnitude

The classical loop shape is shown in Figure 6-9. High gain at low frequencies is very evident in the  $\gamma_0$  curve, whereas the  $\gamma_2$  curve represents much lower gain here. Backing away from  $\gamma_0$  slightly does give a preferred roll off at high frequency, yet the reduction in lower frequency magnitude is very small. Notice that between 1 and 60 rad/sec, in crossover vicinity, the magnitudes are very close.

A very important plot in this chapter is the sensitivity magnitude of Figure 6-10. This is a key transfer function weighted heavily in the  $H_-$  part of the mixed case. The low frequency magnitude is pushed down by the  $H_-$  design, along with the double peaks. In actuality this is more of a smoothing

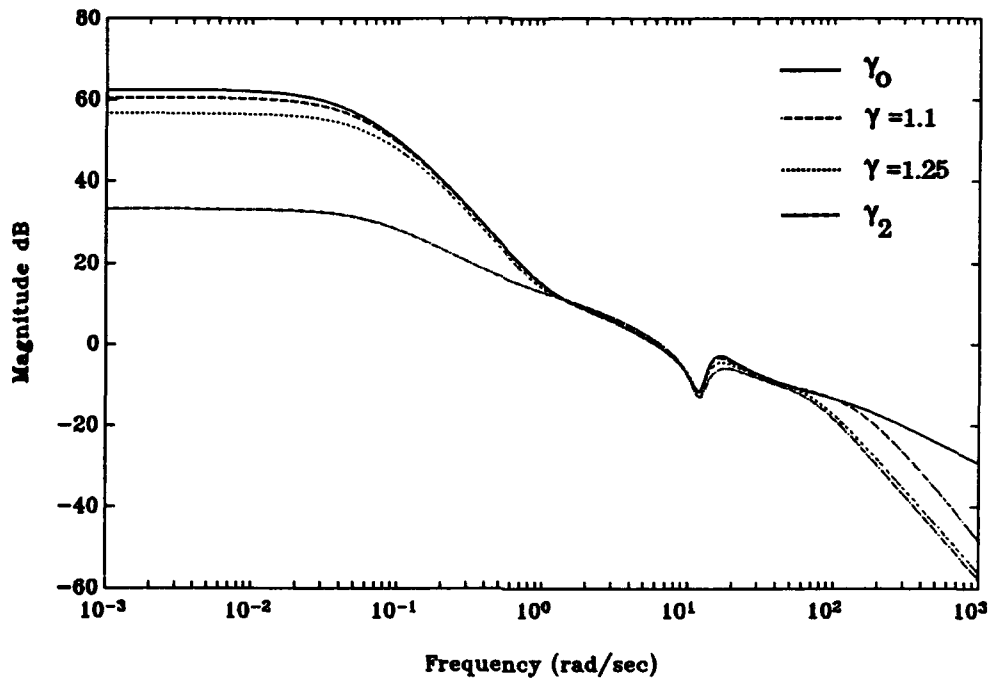


Figure 6-9. Magnitude of  $G(s)K_b(s)$ , LO

effect since the so-called "waterbed effect" holds in this design (notice the  $\gamma_0$  case has higher magnitude around 100 rad/sec). It is evident that the  $\gamma_2$  case gives the lowest complex margins that depend on sensitivity magnitude and is more "sensitive" to disturbances at low frequencies. With  $\gamma = 1.1$ , the sensitivity is very close to the desired  $\gamma_0$  curve. The low frequency magnitude rises slightly, as do the peaks of  $S(s)$  in the  $\gamma = 1.1$  case. Another interesting feature is the sensitivity magnitude for the  $\gamma_2$  case below 7 rad/sec. The plot shows the magnitude of the  $\gamma = 1.25$  case decreasing the wind disturbance, which the pure  $H_\infty$  part did not see before.

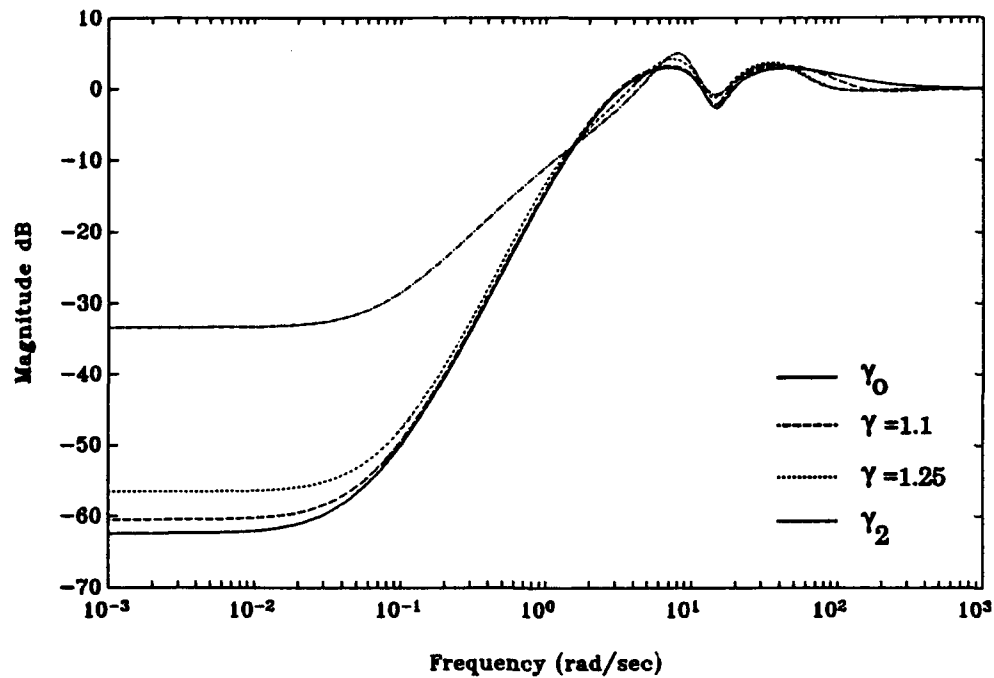


Figure 6-10. Sensitivity Magnitude, LO

Figure 6-11 is the complimentary sensitivity magnitude, and shows the rise above 0 dB appearing to smooth in the  $\gamma_2$  case. This  $\gamma_2$  curve therefore yields the best complex margins that depend on  $T(s)$  and shows that much less high frequency sensor noise will pass through to the plant output because of the low gain. Again the  $H_2$  optimization on  $T_{zw}$  gives this  $\gamma_2$  result. Of interest are the magnitudes of the two mixed cases that also demonstrate much less noise passage at high frequency. The  $\gamma = 1.25$  case is actually very close to the  $H_2$  optimal one at high frequency, although it does have a larger peak.



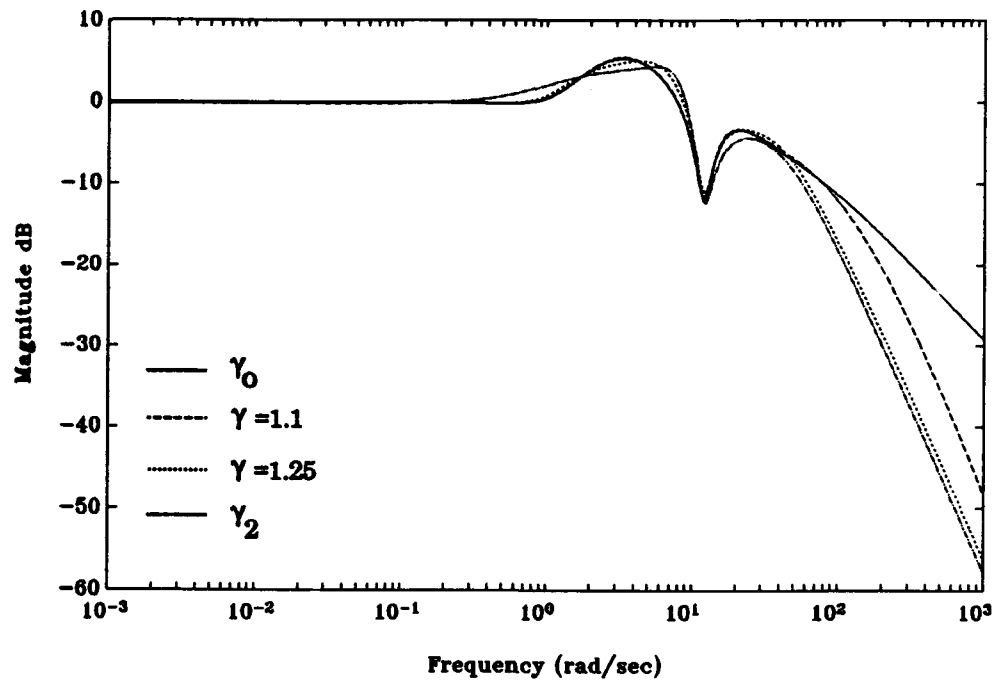


Figure 6-11. Complimentary Sensitivity Magnitude, LO

The closed-loop transfer function magnitude plot is Figure 6-12. This is another key figure that shows important tracking results. The  $H_\infty$  optimal solution on  $T_{cd}$  ( $\gamma_0$  case) clearly will be a poor tracker because of its early drop from 0 dB. This case will also pass more high frequency input noise to the plant output, if high frequency noise comes in with the input signal. The interesting feature is that the  $\gamma = 1.1$ , 1.25, and  $\gamma_2$  curves are almost identical. So going from a  $\gamma = 1.064$  value to  $\gamma = 1.1$  gives a tremendous tracking improvement and brings down  $\|T_{zw}\|_2$  from infinity.

Plant additive uncertainty is shown in Figure 6-13. As before, the low frequency magnitude approaches the inverse of the plant magnitude in this

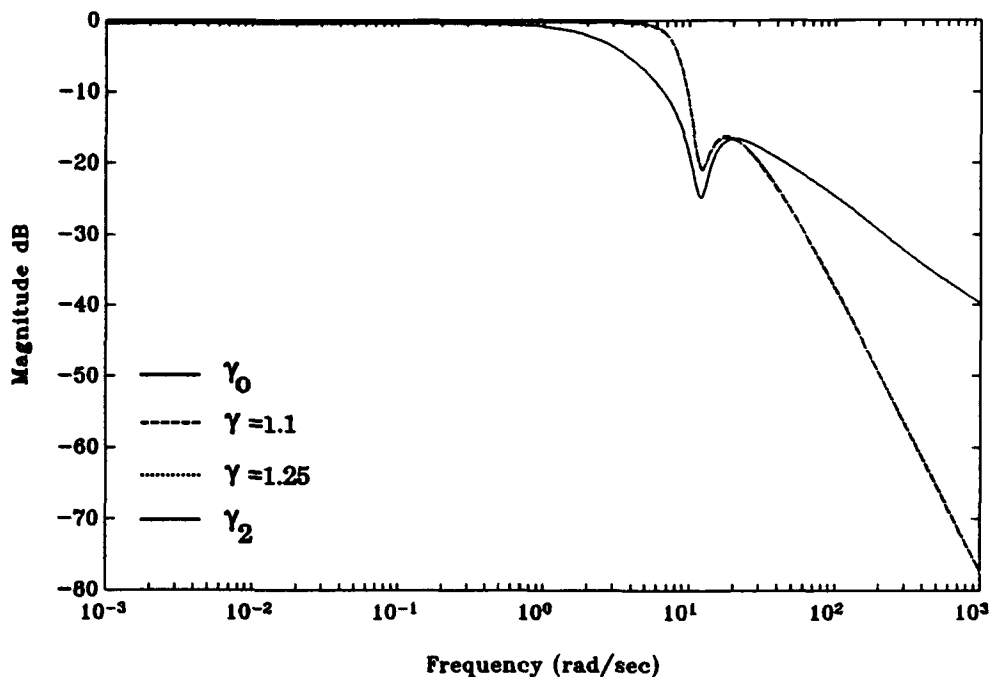


Figure 6-12. Closed-Loop Transfer Function Magnitude, LO

region. The only difference at low frequency is very small and can be seen in the  $\gamma_2$  case, which had the lowest  $K_b(s)$  magnitude in this frequency range. At high frequencies the  $\gamma_2$  case will give the most additive plant uncertainty. From earlier explanations, this plot also gives the noise passage to control usage. The  $\gamma_2$  line clearly minimizes the noise effects at high frequency, with the  $\gamma = 1.25$  case very close.

The  $N_z$  response for a 1 G step input is shown in Figure 6-14. Similar to the  $H_z$  step responses of Chapter V, this plot shows a steady state error for all four cases. Again, this error comes from not having infinite weight on the tracking error, and a solution for this could be to alter  $K_r(s)$  after the design

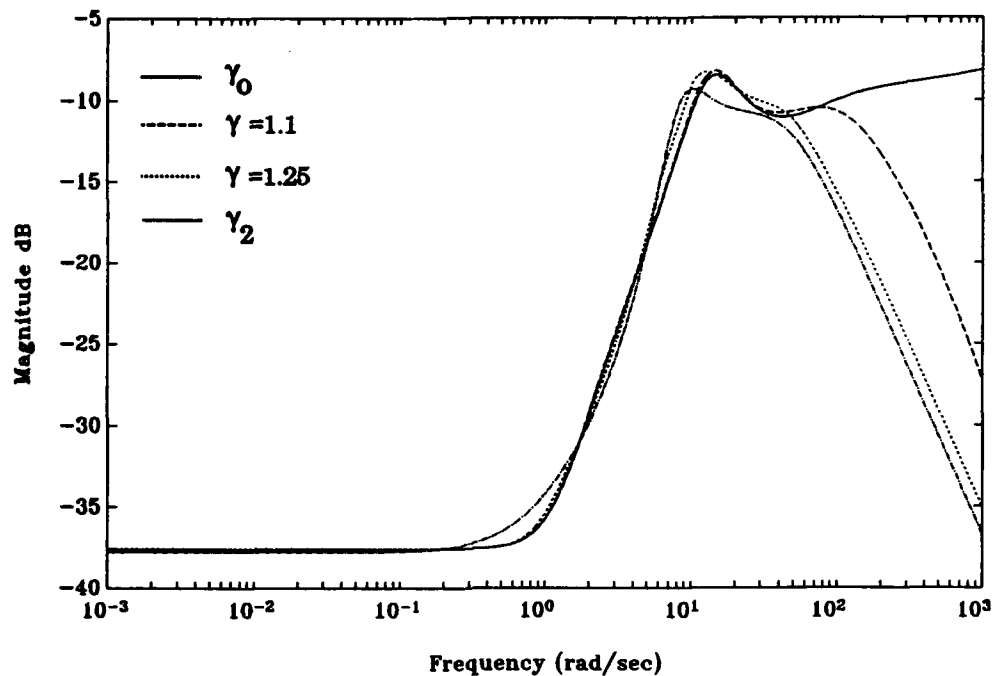


Figure 6-13. Magnitude of  $K_b(s)S(s)$ , LO

process. The three  $\gamma$  cases of 1.1, 1.25, and  $\gamma_2$  all fall almost exactly on top of one another, as foreshadowed by the closed-loop transfer function magnitude. This plot is important in that by raising  $\gamma$  from 1.064 to 1.1, the mixed case gives the desired tracking response. In an examination of the step response with noise inputs included (plot not shown), it was seen that the  $\gamma_0$  case exhibited a large amount of high frequency noise. This was explained in Section 5.2 and again is from the compensator "D" term.

Angle-of-attack response for  $\alpha(0) = 5$  degrees is shown in Figure 6-15. All cases are very similar except for the initial overshoot that is slightly larger for the  $\gamma = 1.25$  and  $\gamma_2$  cases, and the second overshoot for these two cases

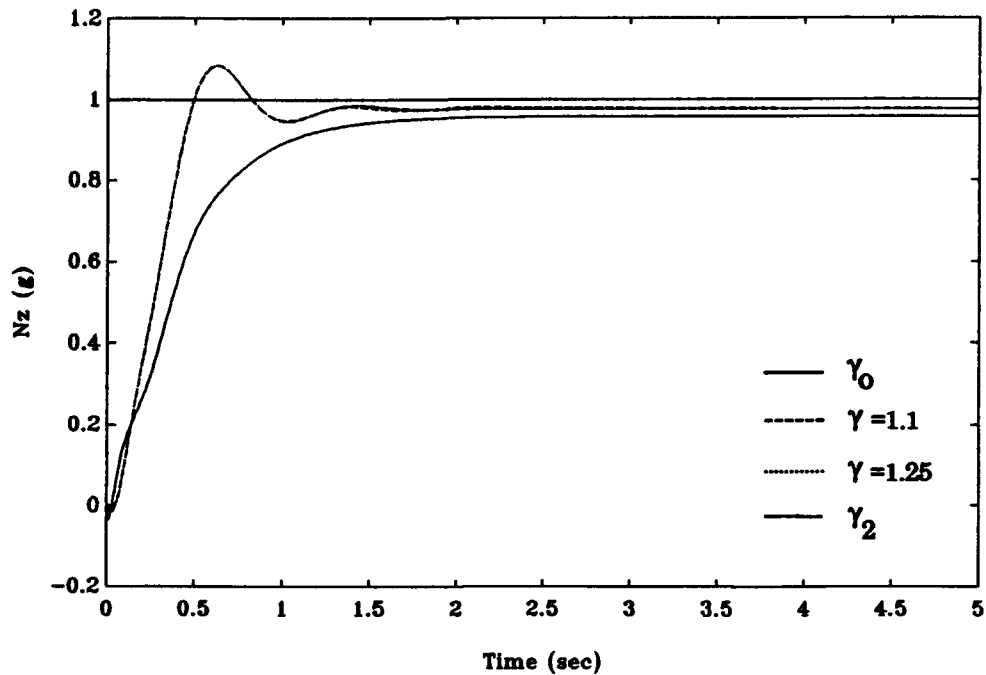


Figure 6-14.  $N_z$  for  $N_z$  Command Step, LO

does not follow the  $\gamma = 1.1$  and  $\gamma_0$  curves. In examining the same plot with noise simulation (plot not shown), there did not appear to be any significant differences in the four cases.

The elevator deflection for the initial  $\alpha(0) = 5$  degrees is Figure 6-16. Note that none of the four cases breaks the 25 degree limit on elevator deflection. As seen in the last plot, the two cases furthest away from  $\gamma_0$  have an overshoot around 0.8 seconds that is not evident in the  $\gamma_0$  and  $\gamma = 1.1$  cases. In a noise examination, the  $\gamma_0$  case was seen to have larger high frequency noise corruption.

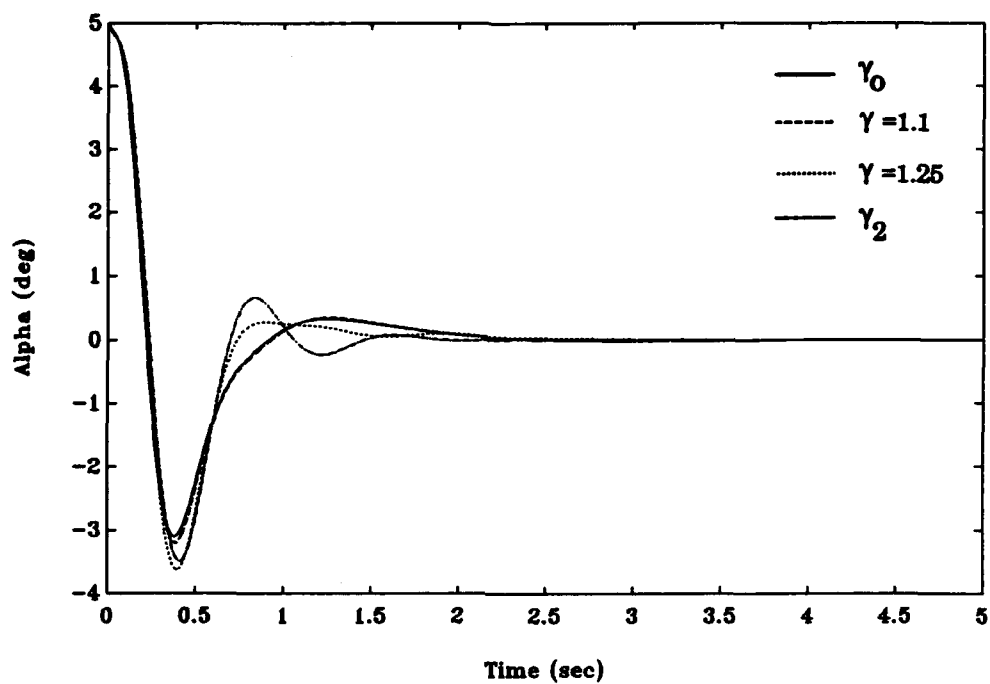


Figure 6-15.  $\alpha$  from  $\alpha(0) = 5$  deg, LO

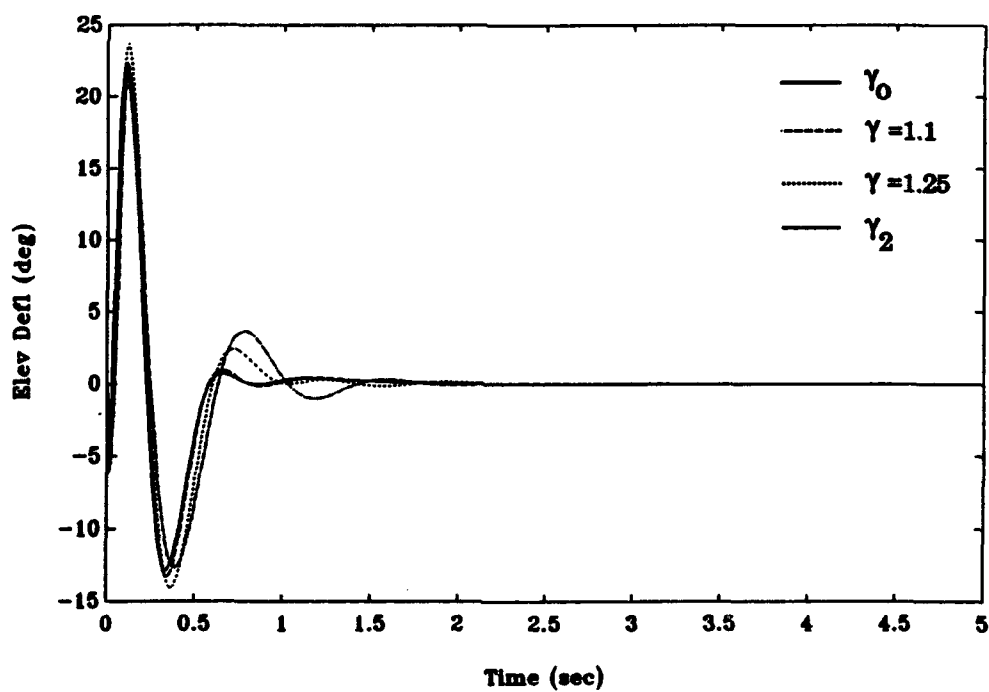


Figure 6-16. Elevator Deflection from  $\alpha(0) = 5$  deg, LO

The responses for the higher order model are all stable and are not shown due to the similarity with the lower order responses. Overall the results of this chapter can be summarized in the following:

i). The mixed case appears to use the nonzero  $Q(s)$  to improve on results seen in the separate  $H_2$  and  $H_\infty$  designs.

ii). Simultaneously good tracking, complex margins from sensitivity, regulation of the  $\alpha$  initial perturbation, and disturbance rejection appear better than in previous designs. At least the tradeoff is apparent now by selecting a  $\gamma$  level.

iii). Feedforward and feedback compensator magnitudes show more of a difference above 1 rad/sec than previous 2 DOF designs. Both compensator magnitudes decrease at high and low frequencies as  $\gamma$  is raised.

iv). The loop shape also decreases at high and low frequencies as the value of  $\gamma$  is increased.

v). The low frequency magnitude of  $S(s)$  increases as  $\gamma$  is raised, and the two magnitude peaks of  $S(s)$  are no longer balanced.

vi). Magnitude at high frequency in  $T(s)$  fell as  $\gamma$  was increased, therefore more multiplicative uncertainty is allowed at high frequencies for the larger  $\gamma$  values.

vii).  $K_p(s)S(s)$  has a high frequency roll off when  $\gamma$  is raised above  $\gamma_0$ . This gives increased allowable plant additive uncertainty at high frequencies.

As a chapter summary, the mixed setup is designed by combining the  $H_2$

tracking baseline case and a modified  $H_\infty$  tracking design. The same  $H_\infty$  diagram and  $T_{ed}$  as in Chapter V is used, but with a much reduced weight on tracking and a greater weight on sensitivity. This combination therefore results in the  $\gamma_0$  case having excellent complex phase and upper gain margins, and low sensitivity magnitude at low frequencies. As  $\gamma$  increases, the poor tracking for the  $\gamma_0$  case rapidly jumps to the good tracking for the  $H_2$  optimal case. The tradeoff with these is very apparent in Figure 6-4, which shows the absolute performance boundaries for the design setup. Also discussed in this chapter were the DFP numerical algorithm for solving the mixed problem and the process used in this work to obtain an initial guess compensator. With the coverage of this final design type and methodology, the overall summary and conclusions of this thesis are presented.

## **VII. Conclusions and Recommendations**

### **7.1 Summary and Conclusions**

The main objective of this thesis was to investigate weight locations and shapes for an F-16  $N_z$  command following system. Three optimal control methodologies were tested during this design weight examination. Successful strategies for obtaining measures of performance and robustness were presented in most designs, with the only exception being the  $H_2$ /LQG design. Separate  $H_2$ ,  $H_\infty$ , and mixed  $H_2/H_\infty$  optimal designs all yielded practical controllers, with different performance and robustness features amongst the designs.

The initial chapter gave a limited design history that presented the motivation for realistic applications of optimal design methods. Choices of design weights, and on which transfer function they might appear, were described as the tools to a successful compensator design. Three optimal methods used in this work were then introduced, and some advantages and disadvantages of each were explained.

Before the design process began, developmental background on the three methodologies and a brief review of related design examples was discussed in Chapter II. Manipulation of the design plant  $P$ , that includes weights, was



seen to be the key to a successful design. Furthermore, in the inspection of related design examples, several weight shapes were given for the mixed-sensitivity transfer functions.

Chapter III presented the F-16 short period approximation (plus first order servo and Padé approximation) as the basic design model, with a higher order model that included the phugoid mode and increased orders of the servo and approximated time delay. Evaluation systems used in Simulink™ were then described, along with possible design difficulties due to an unstable nonminimum phase plant. Thus, Chapters II and III gave the needed development before the first design investigation could begin.

The initial design was the basic  $H_2$ /LQG setup in Chapter IV. Favorable regulation to the  $\alpha$  perturbation was found, but the higher order model was unstable in all cases. Also, the complex margins tended to be low, and no useful input command tracking was observed. Mainly the LQG designs unstable higher order model is what led to including the dynamic weight for the  $H_2$ /Sensitivity design. In this second design of Chapter IV, the higher order model was indeed stabilized by one case, which turned out to be a poor regulator. The complex margins were improved over the basic LQG design, but the tracking of an input command was only acceptable in a few cases (even though the steady state error was now reduced). The final design of Chapter IV was a 2 DOF tracking setup that produced two stabilizing

compensators (for the higher order model), of which one was a good regulator and tracker.

The focus then shifted to the  $H_\infty$  methodology for Chapter V. The tracking setup yielded stable higher order models in all cases. A baseline  $H_\infty$  design was also shown as a good tracker and regulator, and a slightly better regulator than the  $H_2$  tracking design. Also, the  $H_\infty$  case had improved complex phase and upper gain margins, and a lower sensitivity magnitude at low frequencies. Since noise rejection was not addressed by the optimal  $H_\infty$  designs, an investigation into a suboptimal  $H_\infty$  design was given. This suboptimal investigation showed that it would be the choice for a practical application since now the compensator loses its feedthrough "D" term. All  $H_\infty$  designs were also stabilizing for the higher order model.

Chapter VI demonstrated a recent optimization advancement from Ridgely. The general mixed  $H_2/H_\infty$  setup for  $T_{zw}$  and  $T_{ed}$  was identical to the  $H_2$  and  $H_\infty$  tracking designs. While the  $H_2$ /Tracking baseline case was used in  $T_{zw}$ , a different  $H_\infty$  weight selection was used in  $T_{ed}$  (not  $H_\infty$  baseline of Chapter V). The choice of weights for the  $H_\infty$  part of the design drove the sensitivity magnitude transfer function to very low magnitude at low frequency, and also gave excellent complex phase and upper gain margins for this design plant. Driving sensitivity to lower magnitudes and improving margins with the  $H_\infty$  constraint was necessary because the  $H_2$  designs did not attack this problem very well, due to the frequency integral in the 2-norm calculation. The mixed

case proved to be advantageous over any separate  $H_2$  or  $H_\infty$  design investigated, with the visible performance and robustness tradeoff being the key. Although it did give slightly higher peaks to the  $T(s)$  and  $K_b(s)S(s)$  magnitudes, the overall combination of tracking, disturbance rejection at low frequencies, complex margins, and regulation of the initial  $\alpha$  perturbation was not approached by the other optimal designs.

Overall, this work has shown numerous design studies and weight choices. The designer is asked to refer to specific schemes in this work since conclusions from every case cannot be discussed. A key strategy was in analyzing the closed-loop design plant,  $T_{zw}$  or  $T_{cd}$ , to aid in choosing weight shapes, and in choosing the weight locations to get the necessary transfer functions in these closed-loop design plants. The main point is that successful controllers for this model were shown in almost every design type; the only difficulty was in the  $H_2$ /LQG method not stabilizing the higher order model. All  $H_\infty$  (including suboptimal designs) and mixed  $H_2/H_\infty$  cases stabilized the higher order model, and this was seen as a crucial advantage to these methods. Also, 2 DOF controllers were used in most designs, and proved to be the only choice when trying to achieve good tracking with this specific F-16 model. In the  $H_\infty$  designs, the suboptimal  $H_\infty$  compensator was shown to be another necessary choice if any form of sensor noise rejection is needed. The final conclusion is that Ridgely's general mixed  $H_2/H_\infty$  optimization method (of which the example in Chapter VI is the first realistic application), is the

preferred method because of its clear tradeoff between completely independent designs on  $T_{zw}$  and  $T_{ed}$ .

## **7.2 Recommendations for Future Work**

First, this same type of weight study could be conducted on a MIMO example. Because of the increased difficulty in the MIMO case, and the number of design iterations that it takes to go through all three optimization investigations, the mixed  $H_2/H_\infty$  methodology should be concentrated on. Also a viable topic in the mixed case would be to develop the theory for a reduced order compensator. Ridgely proves the full order case in [Rid91], and Wells likewise on the higher order example in [Wel91]. The reduced order (order of  $H_\infty$  design plant) mixed method will have the important advantages of having a start guess central  $H_\infty$  ( $Q(s) = 0$ ) compensator for DFP with the necessary order, and the algorithm will indeed run much faster with the reduced order compensator. One other potential topic in the mixed investigation should be to concentrate on a 1 DOF setup for the  $H_\infty$  part of the problem, since robustness is only controlled in the feedback loop. In summary, the vast amount of potential work on the mixed case is very interesting and obviously could yield great rewards to the control community, this is where the focus should be.

## Appendix A: F-16 Model Data

These plant properties are for Mach 0.6 and sea level.

The state space below represents the short period approximation

$$\begin{aligned} \mathbf{A}_{sp} = & \\ & \begin{bmatrix} -1.4910e+00 & 9.9600e-01 \\ 9.7530e+00 & -9.6000e-01 \end{bmatrix} \end{aligned}$$

$$\begin{aligned} \mathbf{B}_{sp} = & \\ & \begin{bmatrix} -1.8800e-01 \\ -1.9040e+01 \end{bmatrix} \end{aligned}$$

$$\mathbf{C}_{sp} = \begin{bmatrix} 3.5264e+01 & -3.3400e-01 \end{bmatrix}$$

$$\mathbf{D}_{sp} = -4.3660e+00$$

$$\mathbf{Zero}_{sp} = -1.2565e+00 \pm 1.1935e+01i$$

$$\begin{aligned} \mathbf{Pole}_{sp} = & \\ & \begin{bmatrix} -4.3535e+00 \\ 1.9025e+00 \end{bmatrix} \end{aligned}$$

The state space below represents the first order servo

$$\mathbf{A}_{1ser} = -20 \quad \mathbf{B}_{1ser} = 20 \quad \mathbf{C}_{1ser} = 1 \quad \mathbf{D}_{1ser} = 0$$

The state space below represents the first order Padé approximation

$$\mathbf{A}_{1pade} = -40 \quad \mathbf{B}_{1pade} = 1 \quad \mathbf{C}_{1pade} = 80 \quad \mathbf{D}_{1pade} = -1$$

The state space below represents the lower order model (includes second order short period approximation, first order servo, and first order Padé approximation)

**A<sub>low</sub> =**

-2.0000e+01	0	0	0
-1.8800e-01	-1.4910e+00	9.9600e-01	0
-1.9040e+01	9.7530e+00	-9.6000e-01	0
-4.3670e+00	3.5264e+01	-3.3400e-01	-4.0000e+01

**B<sub>low</sub> = [20, 0, 0, 0]<sup>T</sup>**

**C<sub>low</sub> = 4.3670e+00 -3.5264e+01 3.3400e-01 8.0000e+01**

**D<sub>low</sub> = 0**

**Zerolow =**

-1.2564e+00 ± 1.1934e+01i  
4.0000e+01

**Polelow =**

-4.0000e+01  
-4.3535e+00  
1.9025e+00  
-2.0000e+01

The state space below represents the short period and phugoid modes

**A<sub>spphu</sub> =**

-1.4850e-02	3.7382e+01	-3.2200e+01	-1.7940e+01
-8.0000e-05	-1.4910e+00	-1.3000e-03	9.9600e-01
0	0	0	1.0000e+00
-3.6000e-04	9.7530e+00	2.9000e-04	-9.6000e-01

**B<sub>spphu</sub> = [2.1400e-03, -1.8800e-01, 0, -1.9040e+01]<sup>T</sup>**

**C<sub>spphu</sub> = 1.5000e-03 3.5264e+01 2.7200e-02 -3.3400e-01**

**D<sub>spphu</sub> = -4.3660e+00**

**Zerospphu =**  
 $-1.2563e+00 \pm 1.1935e+01i$   
 $-1.4238e-02$   
 $-8.8016e-04$

**Polespphu =**  
 $1.9055e+00$   
 $-8.5673e-03 \pm 7.0838e-02i$   
 $-4.3542e+00$

The state space below represents the fourth order Padé approximation

**A4pade =**  
 $\begin{bmatrix} -4.0000e+02 & -7.2000e+04 & -6.7200e+06 & -2.6880e+08 \\ 1.0000e+00 & 0 & 0 & 0 \\ 0 & 1.0000e+00 & 0 & 0 \\ 0 & 0 & 1.0000e+00 & 0 \end{bmatrix}$

**B4pade =**  $[1, 0, 0, 0]^T$

**C4pade =**  $-8.0000e+02 \quad 3.3469e-08 \quad -1.3440e+07 \quad 1.8126e-04$

**D4pade =**  $1.0000e+00$

**Zero4pade =**  
 $8.4152e+01 \pm 1.0630e+02i$   
 $1.1585e+02 \pm 3.4689e+01i$

**Pole4pade =**  
 $-8.4152e+01 \pm 1.0630e+02i$   
 $-1.1585e+02 \pm 3.4689e+01i$

The state space below represents the fourth order servo

**A4ser =**  
 $\begin{bmatrix} -2.7010e+02 & -2.5366e+04 & -1.1489e+06 & -1.4917e+07 \\ 1.0000e+00 & 0 & 0 & 0 \\ 0 & 1.0000e+00 & 0 & 0 \\ 0 & 0 & 1.0000e+00 & 0 \end{bmatrix}$

$$B4_{ser} = [1, 0, 0, 0]^T$$

$$C4_{ser} = 0 \quad 0 \quad 0 \quad 14911000$$

$$D4_{ser} = 0$$

$$Zero4_{ser} = []$$

$$Pole4_{ser} =$$

$$-1.4480e+02$$

$$-5.2550e+01 \pm 4.8358e+01i$$

$$-2.0200e+01$$

The zeros/poles below represent the higher order system with Padé, Servo, and short period/phugoid plant

$$Zero_{high} =$$

$$8.4152e+01 \pm 1.0630e+02i$$

$$1.1585e+02 \pm 3.4689e+01i$$

$$-1.2563e+00 \pm 1.1935e+01i$$

$$-1.4238e-02$$

$$-8.8016e-04$$

$$Pole_{high} =$$

$$-8.4152e+01 \pm 1.0630e+02i$$

$$-1.4480e+02$$

$$-1.1585e+02 \pm 3.4689e+01i$$

$$-5.2550e+01 \pm 4.8358e+01i$$

$$-2.0200e+01$$

$$-4.3542e+00$$

$$1.9055e+00$$

$$-8.5673e-03 \pm 7.0838e-02i$$



## Bibliography

- [ACD77] Athans, M., D. Castanon, K. Dunn and others. "The Stochastic Control of the F-8C Aircraft Using a Multiple Model Adaptive Control (MMAC) Method - Part I : Equilibrium Flight," *IEEE Trans. Auto. Control*, Vol. 22, No. 5: 768-780 (October 1977).
- [Bic89] Bice, G.W. *Development of an Automatic Ground Collision Avoidance System Using a Digital Terrain Database*. MS thesis, AFIT/GAE/ENY/89D-03. School of Engineering, Air Force Institute of Technology (AU), Wright-Patterson AFB OH, December 1989 (AD-A216247).
- [ChS88] Chiang, R.Y. and M.G. Safonov. *Robust-Control Toolbox User's Guide*, Natick MA: The Mathworks, 1988.
- [Dai90] Dailey, R.L. "Lecture Notes for the Workshop on  $H_\infty$  and  $\mu$  Methods for Robust Control," in conjunction with *American Control Conference*. San Diego CA, May 1990.
- [DFT92] Doyle, J.C., B.A. Francis and A.R. Tannenbaum. *Feedback Control Theory*. New York: Macmillan, 1992.
- [DGKF89] Doyle, J.C., K. Glover, P.P. Khargonekar and B.A. Francis. "State-Space Solutions to Standard  $H_2$  and  $H_\infty$  Control Problems," *IEEE Trans. Auto. Control*, Vol. 34, No. 8: 831-847 (August 1989).
- [Fox71] Fox, R.L. *Optimization Methods for Engineering Design*. Reading MA: Addison-Wesley, 1971.
- [FrL88] Freudenberg, J.S. and D.P. Looze. *Frequency Domain Properties of Scalar and Multivariable Feedback Systems*, in *Lecture Notes in Control and Information Sciences*. Berlin: Springer-Verlag, 1988.

- [Gah92] Gahinet, P.M. "Troubleshooting for State-Space  $H_\infty$  Design," *Proc. of American Control Conference*. 634-638. Chicago IL, June 1992.
- [GLDKS91] Glover, K., D.J.N. Limebeer, J.C. Doyle, E.M. Kassenally and M.G. Safonov. "A Characterization of All Solutions to the Four Block General Distance Problem," *SIAM J. Control and Optimization*, Vol. 29, No. 2: 283-324 (March 1991).
- [Har90] Hartley, G.A. *F-18 Robust Control Design Using  $H_2$  and  $H_\infty$  Methods*. MS thesis. Naval Postgraduate School, Monterey CA, September 1990 (AD-A242562).
- [Ino90] Inoue, A. *Structural Properties of Optimality Based Controller Parameterizations*. MS thesis. Massachusetts Institute of Technology, Cambridge MA, 1990.
- [KwS72] Kwakernaak, H. and R. Sivan. *Linear Optimal Control Systems*. New York: Wiley-Interscience, 1972.
- [Li92] Li, X.P. *Robust Controller Design by  $H_\infty$  Optimization and Structured Singular Value Techniques*. PhD dissertation. Drexel University, Philadelphia PA, 1992.
- [Mid91] Middleton, R.H. "Trade-offs in Linear Control Design," *Automatica*, Vol. 27, No. 2: 281-292 (March 1991).
- [MrR92] Mracek, C.P. and D.B. Ridgely. "Normal Acceleration Command Following of the F-16 Using Optimal Control Methodologies: A Comparison," *1st IEEE Conference on Control Applications*. 602-607. Dayton OH, September 1992.
- [PM90] *Pro-Matlab User's Guide*, Natick MA: The Mathworks, 1990.
- [Rid91] Ridgely, D.B. *A Nonconservative Solution to the General Mixed  $H_2/H_\infty$  Optimization Problem*. PhD dissertation. Massachusetts Institute of Technology, Cambridge MA, 1991.
- [RMV92] Ridgely, D.B., C.P. Mracek and L. Valavani. "Numerical Solution of the General Mixed  $H_2/H_\infty$  Optimization Problem," *Proc. of American Control Conference*. 1353-1357. Chicago IL, June 1992.

- [Sim92] *Simulink - A Program for Simulating Dynamic Systems*, Natick MA: The Mathworks, 1992.
- [SLC89] Safonov, M.G., D.J.N. Limebeer and R.Y. Chiang.  
"Simplifying the  $H_2$  theory via loop-shifting, matrix-pencil and descriptor concepts," *Int. J. Control*, Vol. 50, No. 6: 2467-2488 (April 1989).
- [Wel91] Wells, S.R. *Investigation of the Effects of Increased Order Compensators in Mixed  $H_2/H_\infty$  Optimization*. MS thesis, AFIT/GAE/ENY/92D-14. School of Engineering, Air Force Institute of Technology (AU), Wright-Patterson AFB OH, December 1991 (AD-A243874).
- [Wil71] Willems, J.C. "Least Squares Stationary Optimal Control and the Algebraic Riccati Equation," *IEEE Trans. Auto. Control*, Vol. 16, No. 6: 621-634 (December 1971).
- [Zam66] Zames, G. "On the Input-Output Stability of Time-Varying Nonlinear Feedback Systems Part I: Conditions Derived Using Concepts of Loop Gain, Conicity, and Positivity," *IEEE Trans. Auto. Control*, Vol. 11, No. 2: 228-238 (April 1966).

## **Vita**

Captain James C. Baird was born in Florence, South Carolina on 2 January 1966. He grew up in Florence and graduated from West Florence High School in 1984. With an Air Force ROTC scholarship, he then attended the University of South Carolina in Columbia. He graduated in May of 1988 with a Bachelor of Science degree in Mechanical Engineering, and was commissioned into the USAF. His first assignment was to Aeronautical Systems Division at Wright-Patterson AFB, Ohio. He served as the lead F-15 performance engineer where he was responsible for energy maneuverability and mission analyses for use in specification compliance and by the tactical community. He entered the Air Force Institute of Technology in May 1991 to pursue a Master's Degree in Aeronautical Engineering. His follow on assignment is to the C-17 Combined Test Force at Edwards AFB, CA.

Permanent Address:

754 St. Andrews Lane  
Florence, SC 29501

REPORT DOCUMENTATION PAGE			Form Approved OMB No. 0704-0188	
<small>Public reporting burden for this report is estimated to be 1 hour per report, including the time for reviewing instructions, searching existing data sources, gathering and maintaining the data needed, and completing and reviewing the report. Send comments regarding this burden estimate or any aspect of this collection of information, including suggestions for reducing this burden, to Washington Headquarters Services, Directorate for Information Operations and Reports, Davis Hallway, Suite 1204, Arlington, VA 22202-4302, and to the Office of Management and Administration, Paperwork Reduction Project (0704-0188), Washington, DC 20503.</small>				
1. AGENCY USE ONLY (Leave blank)	2. REPORT DATE December 1992	3. REPORT TYPE AND DATES COVERED Master's Thesis		
4. TITLE AND SUBTITLE STRATEGIES FOR OPTIMAL CONTROL DESIGN OF NORMAL ACCELERATION COMMAND FOLLOWING ON THE F-16			5. FUNDING NUMBERS	
6. AUTHOR(S)  James C. Baird, Captain, USAF				
7. PERFORMING ORGANIZATION NAME(S) AND ADDRESS(ES)  Air Force Institute of Technology, WPAFB OH 45433			8. PERFORMING ORGANIZATION REPORT NUMBER  AFIT/GAE/ENY/92D-08	
9. SPONSORING/MONITORING AGENCY NAME(S) AND ADDRESS(ES)  Dr. Siva Banda WL/FIGCA Wright-Patterson AFB OH 45433			10. SPONSORING/MONITORING AGENCY REPORT NUMBER	
11. SUPPLEMENTARY NOTES				
12a. DISTRIBUTION/AVAILABILITY STATEMENT  Approved for public release; distribution unlimited			12b. DISTRIBUTION CODE	
13. ABSTRACT (Maximum 200 words)  Weight shapes and locations are investigated for $H_2$ , $H_\infty$ , and the general mixed $H_2/H_\infty$ optimization methodologies. The design model is normal acceleration command following for the F-16 (SISO) at Mach 0.6 and Sea Level, which yields a nonminimum phase and unstable plant. $H_2$ design types include LQG, LQG/Sensitivity, and LQG/Tracking. Robustness and tracking are the objectives of the central $H_\infty$ process. Both $H_\infty$ optimal and suboptimal controllers are examined, with the suboptimal controller shown as the practical choice for this plant. The mixed $H_2/H_\infty$ setup allows the tradeoff between $H_2$ tracking and noise rejection, and $H_\infty$ robustness. Results of weight choices on all designs are discussed, with the mixed $H_2/H_\infty$ design being favored.				
14. SUBJECT TERMS Optimization, Optimal Control, $H_2$ , $H_\infty$ , Mixed $H_2/H_\infty$ Compensator Design, Tracking, F-16, SISO			15. NUMBER OF PAGES 195	
			16. PRICE CODE	
17. SECURITY CLASSIFICATION OF REPORT Unclassified	18. SECURITY CLASSIFICATION OF THIS PAGE Unclassified	19. SECURITY CLASSIFICATION OF ABSTRACT Unclassified	20. LIMITATION OF ABSTRACT  UL	